

***Ab-Initio* Simulations of Materials Using VASP: Density-Functional Theory and Beyond**

JÜRGEN HAFNER

*Faculty of Physics and Center for Computational Materials Science, Universität Wien,
Sensengasse 8, A-1090 Wien, Austria*

Received 22 February 2008; Accepted 9 May 2008

DOI 10.1002/jcc.21057

Published online 11 July 2008 in Wiley InterScience (www.interscience.wiley.com).

Abstract: During the past decade, computer simulations based on a quantum-mechanical description of the interactions between electrons and between electrons and atomic nuclei have developed an increasingly important impact on solid-state physics and chemistry and on materials science—promoting not only a deeper understanding, but also the possibility to contribute significantly to materials design for future technologies. This development is based on two important columns: (i) The improved description of electronic many-body effects within density-functional theory (DFT) and the upcoming post-DFT methods. (ii) The implementation of the new functionals and many-body techniques within highly efficient, stable, and versatile computer codes, which allow to exploit the potential of modern computer architectures. In this review, I discuss the implementation of various DFT functionals [local-density approximation (LDA), generalized gradient approximation (GGA), meta-GGA, hybrid functional mixing DFT, and exact (Hartree-Fock) exchange] and post-DFT approaches [DFT + U for strong electronic correlations in narrow bands, many-body perturbation theory (GW) for quasiparticle spectra, dynamical correlation effects via the adiabatic-connection fluctuation-dissipation theorem (AC-FDT)] in the Vienna *ab initio* simulation package VASP. VASP is a plane-wave all-electron code using the projector-augmented wave method to describe the electron-core interaction. The code uses fast iterative techniques for the diagonalization of the DFT Hamiltonian and allows to perform total-energy calculations and structural optimizations for systems with thousands of atoms and *ab initio* molecular dynamics simulations for ensembles with a few hundred atoms extending over several tens of ps. Applications in many different areas (structure and phase stability, mechanical and dynamical properties, liquids, glasses and quasicrystals, magnetism and magnetic nanostructures, semiconductors and insulators, surfaces, interfaces and thin films, chemical reactions, and catalysis) are reviewed.

© 2008 Wiley Periodicals, Inc. J Comput Chem 29: 2044–2078, 2008

Key words: density-functional theory; plane-wave basis; pseudopotentials; projector-augmented-waves; hybrid functionals; many-body perturbation theory; solid state physics; solid state chemistry; materials science; surface science; catalysis

Introduction

The last two decades have witnessed tremendous progress in the development of methods for *ab initio* calculations of materials properties and for simulations of processes in materials. The cornerstone of this development was laid by density-functional theory (DFT), which casts the intractable complexity of the electron–electron interactions in many-electron systems into an effective one-electron potential, which is a functional of the electron density only.^{1–4} Although the form of this functional which would make the reformulation of the many-electron Schrödinger equation (the Kohn–Sham equations) exact is not known, starting with the pioneering work of Perdew, Becke, and coworkers a hierarchy of approximate functionals has been developed, which allow to predict many properties of solids with increasing accuracy.^{5–8} However, it cannot be overlooked that in the quest for better density-functionals, different

cultures have developed in quantum chemistry and in condensed-matter physics. Quantum chemists have realized very early the need to correctly reproduce the atomic one- and two-electron densities in atoms and molecules, but in addition, to maximize accuracy a number of empirical parameters are often introduced in a functional^{6,9–14} The resulting semiempirical approximations may be very accurate within their “training sets” (i.e., for systems similar to those in the data sets used for the optimization of the adjustable parameters) but often fail when applied to different situations because the optimized parameters are not transferable from one system (e.g., small molecules) to another (e.g., solids or solid surfaces). A striking example is provided by the B3LYP functional,^{15,16} which

Correspondence to: J. Hafner; e-mail: juergen.hafner@univie.ac.at

is the most popular functional in quantum chemistry. This functional contains a total of eight empirical parameters, which allow to achieve a very high accuracy for almost all properties of small molecules. However, the B3LYP functional fails to reproduce the correct exchange-correlation energy of the homogeneous electron gas. Consequently, the accuracy of B3LYP predictions deteriorates rapidly with increasing molecular size,^{17,18} and the functional fails quite badly for metallic solids.¹⁹ The solid-state physics community, under the leadership of John Perdew, has followed another strategy: Exchange-correlation functionals may also be designed to satisfy as many exact constraints (known, e.g., from many-body theory) as possible. Parameters introduced into the functional are nonempirical in the sense that they are determined by these constraints instead of being adjusted to reproduce experimental data. Nonempirical functionals that satisfy a sufficient number of constraints^{20–23} are more likely to be transferable and to perform equally well in different tasks. A particular challenge in the construction of nonempirical functionals is to respect the two paradigms prevalent in quantum chemistry and in solid state physics: the one- and two-electron densities in molecular quantum chemistry and the slowly varying electron densities in condensed matter physics. The relevance of the electron-gas limit to atoms, molecules, and solids and the difficulties to construct an exchange-correlation functional whose gradient-dependence allows to achieve good accuracy for atomization energies on one, and lattice parameters or surface energies on the other hand have very recently been discussed by Perdew and coworkers.^{24,25}

A substantial part of this review will be devoted to discuss the implementation of these functionals in a code using a plane-wave basis-set and their performance in describing various materials properties. However, even with the radical simplification introduced by DFT, *ab initio* calculations for solids were restricted, for a long time, to simple systems with small unit cells.

The rapid development of electronic-structure theory of solids during the last decades was triggered by a seminal paper published in 1985 by Car and Parrinello,²⁶ in which they proposed to solve the equations of motions of the coupled many-atom, many-electron system via a dynamical simulated annealing strategy. The Car-Parrinello (CP) method was designed to replace the traditional approach consisting of the iterative self-consistent solution of the Kohn-Sham equations for the electrons, the calculation of the forces acting on the atoms via the Hellmann-Feynman theorem, and the integration of the Newtonian equations of motions of the ions—the procedure having to be repeated after each ionic integration step until the ground state of the many-atom, many-electron system had been reached. In addition, the CP paper introduced several other important innovations. One which is very important for the methodology to be described below is the use of Fast Fourier Transforms to switch between real-space and momentum-space representations of the wave function because different parts of the calculation can be done most efficiently in one space or another: The kinetic energy has a diagonal representation in momentum space while the potential energy is diagonal in real space. The second step forward was based on the observation that it is inefficient to do one part of the calculation (the solution of the Kohn-Sham equations) with very high accuracy while the other part (the determination of the equilibrium ionic configuration) is still far from convergence. This led immediately to the bold idea—already referred to above—that

the total energy of a system could be minimized simultaneously with respect to both the electronic and ionic degrees of freedom. It was only after the publication of the CP paper that the full potential of DFT has been exploited: what had been so far a technique used by a small community of solid-state theorists was transformed into a powerful tool for materials research, with applications in many different areas such as structural materials, catalysis and surface science, nanomaterials, biomaterials, and geophysics (for a recent review of the impact of DFT on materials research see ref. 27).

Although much of the recent development was undoubtedly triggered by the Car-Parrinello paper, it is a bit ironical that the development of modern DFT calculations is characterized by a rather quick return to the more traditional approach. The reason is twofold: First, the CP approach of a dynamical updating of the electronic degrees of freedom requires electrons and ions to be effectively decoupled such that, once the electronic ground-state has been reached, the system remains close to the adiabatic Born-Oppenheimer surface. This condition is met with good accuracy for insulators and wide-gap semiconductors but violated for metals and narrow-gap materials. The second reason is that the minimization of the total energy does not allow an efficient control of charge-density fluctuations during the iterative process—for metallic systems such fluctuations (often referred to as “charge-sloshing”) may even prevent a convergence of this process.

Modern DFT calculations for solids are determined by several technical choices: (i) The choice of a basis set to expand the Kohn-Sham eigenfunctions. Essentially, the choice is between plane waves and localized basis functions. (ii) The interactions between the ionic core and the valence electrons can be described either by a full-potential approach or by a pseudopotential eliminating the need to account for the complex nodal character of the valence orbitals. (iii) The method adopted for the determination of the eigenstates of the Kohn-Sham Hamiltonian. (iv) The description of the electron-electron interactions by choosing an exchange-correlation functional within the hierarchy of functionals proposed within DFT.³ In those cases where DFT alone does not provide an adequate solution (strong electronic correlations, excited eigenstates, . . .) post-DFT corrections such as many-body perturbation theory^{28,29} or dynamical mean field theory^{30,31} may be used to improve the DFT predictions.

In the present review, I shall concentrate on the theoretical background of the Vienna *ab initio* simulation package VASP developed by Georg Kresse and his coworkers^{32–35} and on applications of this code in key areas of modern solid-state physics and chemistry. VASP is a plane-wave code for *ab-initio* density-functional calculations. It attempts to match the accuracy of the most advanced all-electron codes by using a projector-augmented-wave approach (PAW)³⁶ for describing the electron-ion interaction. A stable and accurate solution of the Kohn-Sham equations, as well as a favorable scaling of the computational effort with system size, are achieved by adopting iterative diagonalization techniques and optimized charge-mixing routines. Different levels of exchange-correlation functionals and different post-DFT approaches have been implemented. A variety of routines added to the basic DFT solver allow to calculate a wide variety of materials properties. I begin by reviewing the basic methodology.

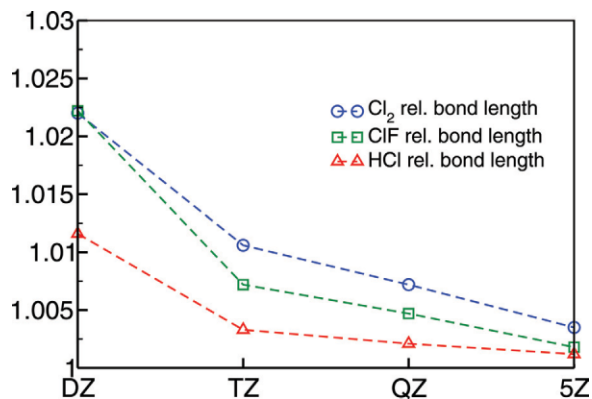


Figure 1. Convergence of the relative bond-lengths of Cl₂, ClF, and HCl molecules calculated using various local basis sets [aug-cc-pVXZ with $X = 2$ (double), 3 (triple), 4 (quadruple), 5 (quintuple)] relative to the plane-wave results. Cf. text. After Kresse et al.³⁷ [Color figure can be viewed in the online issue, which is available at www.interscience.wiley.com.]

The Vienna *Ab Initio* Simulation Package VASP — Basic Methodology

Why Plane Waves?

Modern electronic structure methods fall into two broad classes, depending on the choice of the basis set for the expansion of the valence orbitals, charge densities and potentials: plane-wave methods or methods using some kind of localized basis functions, e.g., Gaussian-type orbitals. The use of a plane-wave basis has several immediate advantages: (i) It is easy to change from a real-space representation (where the potential energy V has a diagonal representation) via a Fast Fourier Transform to momentum-space where the kinetic energy T is diagonal. (ii) The control of basis-set convergence is almost trivial; it is sufficient to monitor the eigenvalues and total energies as a function of the cut-off energy, i.e., the highest kinetic energy of a plane-wave within the chosen basis set. (iii) The Hellmann-Feynman forces acting on the atoms and the stresses on the unit cell may be calculated straightforwardly in terms of the expectation value of the Hamiltonian with respect to the ionic coordinates. (iv) Basis-set superposition errors that have to be carefully controlled in calculations based on local basis sets are avoided. On the other hand, a set of local Gaussian basis functions allows an analytic integration of the $1/r$ singularity of the Coulomb potential—this is instrumental to a fast calculation of exact (Hartree-Fock) exchange. The treatment of exact exchange is more difficult with a plane-wave basis. We shall return to this point below.

A very important point is that a reasonable convergence of a plane-wave expansion can be achieved only if the nodal character of the valence orbitals is eliminated, i.e., if the ion–electron interaction is described by some kind of pseudopotential. This raises the question of the accuracy and transferability of pseudopotentials, and the necessity linearize the valence-core exchange-correlation interactions. I shall discuss below how these problems can be solved within the projector-augmented wave method.^{35,36}

The pseudopotential and related methods are sometimes regarded as unnecessary approximations by quantum-chemists, while the plane-wave community considers local basis set results with some suspicion because of basis-set completeness and basis-set superposition errors. Therefore, a demonstration that both approaches lead to perfectly converged results is very important. Kresse et al.³⁷ have reported benchmark results on optimized geometries and atomization energies of molecules calculated with VASP (using a plane-wave basis set and the projector-augmented wave method) and GAUSSIAN03 (G03)³⁸ using large local basis sets. An illustration of the results is given in Figure 1 for the difficult (for plane waves) case of diatomic molecules containing Cl. It is evident that a very large local basis set [an augmented correlation-consistent polarized valence quintuple-zeta (aug-cc-pV5Z) basis set] is required to match the converged plane-wave results. Generally bond lengths of small molecules agree within 0.1%. The necessity to use a large basis set also has a consequence on the computational cost. While for the small molecules the plane-wave VASP and local basis-set quadruple-zeta calculations perform roughly equally, the cost increases dramatically for the quintuple-zeta basis necessary to achieve full convergence. In fairness, it must be pointed out that the G03 calculations are all-electron calculations, while the VASP-PAW calculations are full-potential valence-only calculations. As a consequence, G03 calculations will be very expensive for larger systems for which plane-wave calculations are suited very well. The influence of the frozen-core approximation used in the PAW method will be discussed below.

Very recently, a comparative investigation of the performance of plane-wave (VASP) and local-basis set methods (using the GAUSSIAN and SIESTA packages⁴⁰) in structural studies of small gold clusters has been presented by Gruber et al.³⁹ For a wide class of relatively compact cluster structures the authors found excellent agreement between the binding energies calculated using both methods, while planar structures were found to have a somewhat reduced stability in the local-basis set calculations. This difference was attributed to the fact that the quality of the plane-wave basis set is independent of the topology of the system while the quality of a basis composed of atom-centred local orbitals depends on the relative atomic positions (a situation which is evidently reminiscent of the basis-set superposition error). It was concluded that the relatively lower binding energy of planar clusters provided by SIESTA and GAUSSIAN03 could be a consequence of a lower “effective quality” of the basis set for systems that are more extended in one or two dimensions compared with more compact structures

Potentials, pseudopotentials

Pseudopotentials have been introduced to avoid the need for an explicit treatment of the strongly bound and chemically inert core electrons. They are a necessary ingredient of all plane-wave methods, but they can also be used in local-basis set methods to reduce the computational effort. The theory of pseudopotentials is mature, but the practice of constructing accurate, transferable, and efficient pseudopotentials is far from straightforward. Methods for generating pseudopotentials include the ‘norm-conserving’ *pseudopotentials*^{41,42} (the “norm-conservation” criterion applied to the node-less pseudo wave functions ensures that not only the logarithmic derivative of the exact and pseudo-wavefunctions, but also

their derivatives with respect to the energy agree at the chosen reference energy and cut-off radius) and the “ultrasoft” pseudopotentials (where the norm-conservation criterion is dropped, but the logarithmic derivatives are matched at two or more reference energies spanning the entire range of eigenvalues of the valence electrons).^{41,43} The ultrasoft pseudopotentials have the merit to make calculations for first-row elements and for systems with d – or f –electrons feasible at tractable effort. The criterion for the quality of a pseudopotential is not how well it matches experiment, but how well it reproduces the results of accurate all-electron calculations. A certain drawback of pseudopotential calculations is that because of the nonlinearity of the exchange interaction between valence and core electrons, elaborate non-linear core corrections⁴⁴ are required for all systems where the overlap between valence- and core-electron densities is not completely negligible. This deficiency may be removed by using the projector-augmented wave method.

Projector-augmented waves

The *projector-augmented wave* (PAW) method originally introduced by Blöchl³⁶ represents an attempt to achieve simultaneously the computational efficiency of the pseudopotential method as well as the accuracy of the full-potential linearized augmented-plane-wave (FLAPW) method,⁴⁵ which is commonly regarded as the benchmark for DFT calculations on solids. Unlike the pseudopotential approach, the PAW method accounts for the nodal features of the valence orbitals and ensures orthogonality between valence and core wave functions. In the PAW approach, the all-electron (AE) valence wave functions ψ_n^{AE} are reconstructed from the pseudo (PS) wave functions via a linear transformation^{35,36}

$$|\psi_n^{\text{AE}}\rangle = |\psi_n^{\text{PS}}\rangle + \sum_l (|\phi_l^{\text{AE}}\rangle - |\phi_l^{\text{PS}}\rangle) |p_l^{\text{PS}}\langle \psi_n^{\text{PS}}|. \quad (1)$$

The pseudo-wave functions ψ_n^{PS} (n is the band index) are the variational quantities and are expanded in plane waves. In the regions between the PAW spheres surrounding the atoms, the ψ_n^{PS} are identical to the AE wave functions ψ_n^{AE} , but inside the spheres the ψ_n^{PS} are only a bad approximation to the exact wave functions, they are used only as a computational tool. The AE partial waves ϕ_i^{AE} are solutions of the spherical scalar-relativistic Schrödinger equation for a nonspinpolarized atom at a reference energy ε_i in the valence regime and for an angular momentum l_i (we use atomic units),

$$\left(-\frac{1}{2}\Delta + v_{\text{eff}}^{\text{AE}}\right) |\phi_i^{\text{AE}}\rangle = \varepsilon_i |\phi_i^{\text{AE}}\rangle, \quad (2)$$

where $v_{\text{eff}}^{\text{AE}}$ is the spherical component of the AE potential. The index i is short-hand for the reference energy ε_i , the angular momentum quantum numbers (l_i, m_i) , and the atomic coordinates \vec{R}_i . The PS partial waves ϕ_i^{PS} are node-less and identical to the AE partial wave outside a core radius r_c (approximately equal to half the nearest-neighbor distance) and match continuously to ϕ_i^{PS} inside these spheres.

The projector functions p_i^{PS} are constrained to be dual to the partial waves, they are constructed by a two-step procedure: First, intermediate functions χ_i are computed via

$$|\chi_i\rangle = \left(\varepsilon_i + \frac{1}{2}\Delta - v_{\text{eff}}^{\text{PS}}\right) |\phi_i^{\text{PS}}\rangle, \quad (3)$$

where $v_{\text{eff}}^{\text{PS}}$ is the spherical component of the effective pseudopotential, which can be chosen arbitrarily inside the radius r_c but must match $v_{\text{eff}}^{\text{AE}}$ for $r \geq r_c$. The projector functions are linear combinations of the χ_i with^{35,43}

$$|p_i^{\text{PS}}\rangle = \sum_j (B_{ji}^{-1}) |\chi_j\rangle, \quad B_{ij} = \langle \phi_i^{\text{PS}} | \chi_j \rangle, \quad (4)$$

such that the ϕ_i^{PS} and p_i^{PS} are dual, $\langle p_i^{\text{PS}} | \phi_j^{\text{PS}} \rangle = \delta_{ij}$, and $\langle r | p_i^{\text{PS}} \rangle = 0$ for $r > r_c$.

It may be shown that the PS partial waves are exact solutions of a generalized Kohn-Sham eigenvalue equation

$$\begin{aligned} & \left(-\frac{1}{2}\Delta + v_{\text{eff}}^{\text{PS}} + \sum_{ij} |p_i^{\text{PS}}\rangle D_{ij} \langle p_j^{\text{PS}}| \right) |\phi_k^{\text{PS}}\rangle \\ & = \varepsilon_k \left(1 + \sum_{ij} |p_i^{\text{PS}}\rangle Q_{ij} \langle p_j^{\text{PS}}| \right) |\phi_k^{\text{PS}}\rangle, \end{aligned} \quad (5)$$

with the integrated compensation charges Q_{ij} and the one-center strength parameters D_{ij} defined by

$$Q_{ij} = \langle \phi_i^{\text{AE}} | \phi_j^{\text{AE}} \rangle - \langle \phi_i^{\text{PS}} | \phi_j^{\text{PS}} \rangle, \quad (6)$$

$$D_{ij} = \left\langle \phi_i^{\text{AE}} \left| -\frac{1}{2}\Delta + v_{\text{eff}}^{\text{AE}} \right| \phi_j^{\text{AE}} \right\rangle - \left\langle \phi_i^{\text{PS}} \left| -\frac{1}{2}\Delta + v_{\text{eff}}^{\text{PS}} \right| \phi_j^{\text{PS}} \right\rangle. \quad (7)$$

Within the PAW method the charge density corresponding to an all-electron eigenstate Ψ_n^{AE} , $n(\vec{r}) = \langle \Psi_n^{\text{AE}} | \vec{r} \rangle \langle r | \Psi_n^{\text{AE}} \rangle$ is composed of three contributions,

$$n(\vec{r}) = n^{\text{PS}}(\vec{r}) - n^{\text{PS},1}(\vec{r}) + n^{\text{AE},1}(\vec{r}), \quad (8)$$

where

$$n^{\text{PS}}(\vec{r}) = \langle \Psi_n^{\text{PS}} | \vec{r} \rangle \langle r | \Psi_n^{\text{PS}} \rangle \quad (9)$$

is a pseudo charge density expanded in a plane wave basis whereas

$$n^{\text{PS},1}(\vec{r}) = \sum_{ij} \langle \phi_i^{\text{PS}} | r \rangle \langle r | \phi_j^{\text{PS}} \rangle \langle \Psi_n^{\text{PS}} | p_i^{\text{PS}} \rangle \langle p_j^{\text{PS}} | \Psi_n^{\text{PS}} \rangle \quad (10)$$

and

$$n^{\text{AE},1}(\vec{r}) = \sum_{ij} \langle \phi_i^{\text{AE}} | r \rangle \langle r | \phi_j^{\text{AE}} \rangle \langle \Psi_n^{\text{PS}} | p_i^{\text{PS}} \rangle \langle p_j^{\text{PS}} | \Psi_n^{\text{PS}} \rangle \quad (11)$$

are pseudo and all-electron on-site charge densities that are expanded on atom-centered radial grids. The decomposition of the

wave functions and of the charge density illustrates the principle of the PAW method: A node-less pseudo wave function and the corresponding pseudo charge density are determined by solving a generalized Kohn-Sham equation in a plane wave basis. The exact all-electron wave function and charge density displaying the full nodal character are reconstructed by subtraction of the pseudo on-site terms and addition of the exact on-site terms, both are expanded on a radial support grid. An analogous decomposition with no cross-terms between on-site and plane-wave terms holds for all expectation values of quantum-mechanical operators, and in particular for the total energy of the electrons, i.e.,

$$E = E^{\text{PS}} - E^{\text{PS},1} + E^{\text{AE},1}, \quad (12)$$

where each of the three terms consists of a kinetic, Hartree, and exchange-correlation contribution.

Forces on the atoms and stresses on the unit cell are calculated within VASP as derivatives of the free energy with respect to the ionic positions and the shape of the unit cell. The derivatives of the free-energy contain both Hellmann-Feynman⁴⁶ as well as Pulay⁴⁷ contributions—note that for a pure plane-wave basis set no Pulay contributions exist, but they contribute in calculations with the US-PP and PAW methods because of the dependence of the on-site terms on the ionic coordinates.

A detailed comparison of the performance of the PAW approach implemented in VASP with all-electron calculations based on the full-potential linearized augmented plane wave (FP-LAPW) plus local orbital (lo) method as implemented in the WIEN2k code⁴⁸ and using a Gaussian-type orbitals approach⁴⁹ has recently been presented by Paier et al.⁵⁰ All calculations have been based on the same gradient-corrected exchange-correlation functional due to Perdew, Burke, and Ernzerhof (PBE).²⁰ The comparison demonstrates that for lattice constants and bulk moduli perfect agreement between VASP-PAW and FP-LAPW + lo calculations is achieved for *all* types of materials, although both are based on entirely different approaches. Between VASP-PAW and GTO calculations, reasonably good agreement is found for most insulators, semiconductors, and simple metals, whereas substantial differences exist for open-shell transition metals. The comparison is illustrated in Figure 2 for the lattice constants of a few representative systems. The good agreement between VASP-PAW and FP-LAPW + lo calculations has also been confirmed for complex reactions at surfaces.⁵¹

Compared with experiment, calculations using the PBE functionals tend to overestimate the lattice constants, although the largest error is only about 2% and the mean absolute error is around 0.04 Å. Improvement depends on the availability of a better functional, this will be discussed below.

The PAW method has been described as an all-electron (AE) method—this is correct in the sense that it correctly describes the nodal features of the valence orbitals which are also correctly orthogonalized to the core wave functions. However, as it is based on a frozen core (FC) approximation, it is not an AE method in the sense that all electronic eigenstates are treated selfconsistently. This is in contrast to the FP-LAPW method in which the core wave functions and charge densities are computed self-consistently within a spherical approximation to the one-center effective potential. However, it should be evident from the comparison discussed above

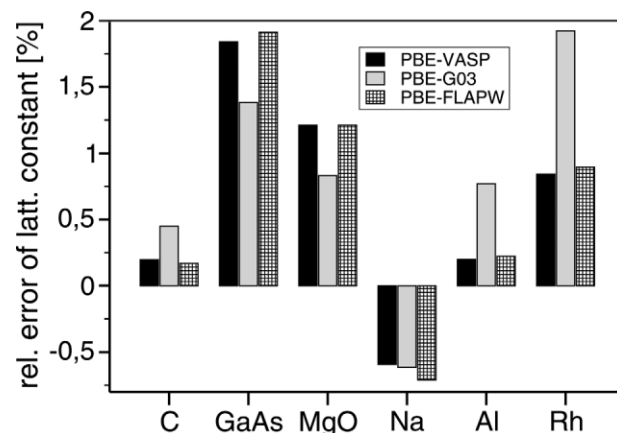


Figure 2. Comparison of the error in the equilibrium lattice constants of selected solids as determined using VASP-PAW, FP-LAPW + lo, and GTO calculations. Cf. text. After Kresse et al.⁵⁰

that the FC approximation is by no means a crude approximation—for the calculation of most properties of molecules or solids it is perfectly legitimate. Only in two cases, the FC approximation is questionable: (i) It leads to a substantial underestimation of the *s*–*d* promotion energies in 3*d* transition metals. (ii) Core-relaxation effects may affect the results of calculations of final-state core-level shifts. The final step toward a *relaxed-core projector-augmented-wave (RC-PAW) method*, including a selfconsistent optimization of the core-charge density, preserving the orthogonality between core and valence orbitals, has recently been made by Marsman and Kresse.⁵²

The RC-PAW method is based on the following selfconsistent cycle: (i) Solve selfconsistently the spherical one-center Schrödinger equation for the core states ϕ_c and the AE core charge density n_c . (ii) Solve the spherical Schrödinger equation for the new AE partial waves ϕ_i^{AE} . (iii) Pseudize the partial waves, $\phi_i^{\text{AE}} \rightarrow \phi_i^{\text{PS}}$ and calculate the new compensation charges Q_{ij} and one-center strength parameters D_{ij} . (iv) Solve the generalized Kohn-Sham equations, $(H - \varepsilon S)|\Psi_n^{\text{PS}}\rangle$ for the PS wave functions. (v) Calculate the pseudo valence charge density and the one-center PS and AE charge densities. (vi) Mix the new charge densities with those from the previous iteration step and return to (i), iterating until self-consistency of core and valence states has been achieved. If the core charge is confined to the PAW spheres (which also implies that the pseudized ionic charge remains constant), the only contributions to the total energy that are affected by the changes in the core charge density are the Hartree and the kinetic energy - details are described by Marsman and Kresse.⁵² It is important to note that the inclusion of core relaxation hardly changes the computational effort because the additional calculations are performed only within the PAW spheres and are much less demanding than the plane wave part of the computations.

The influence of the relaxation of the ionic core is largest in calculations of the $4s^2 3d^n \rightarrow 4s^1 3d^{n+1}$ inter-configurational energies ΔE_{ic} of the 3*d* transition metals: compared to AE calculations, the FC approximations introduces an error of about –100 meV in the ΔE_{ic} varying between 1.4 eV for Ti and –2.03 eV for C, which is reduced to less than 10 meV in RC-PAW calculations. In

these calculations, only 4s and 3d electrons have been treated as valence—if the 3p states are treated as valence states, the FC error in the inter-configurational energies is reduced to about −15 meV, and to less than 2 meV in a RC-PAW calculation.⁵² For surface core level shifts, the RC corrections are about 10%. For the ground-state properties of molecules and solids, the RC-PAW calculations confirm that the FC approximation is indeed very sound: atomization energies of molecules are affected (with the only exception of LiF) by at most 0.05 kcal/mol (generally by less than 0.02 kcal/mol), lattice constants of Fe by at most 0.05 Å. A certain advantage of the RC-PAW method is that it completely eliminates a certain weak dependence of the results on the atomic reference configuration chosen for the construction of the PAW data set, but the influence of the data set changes lattice constants by less than 0.01 Å and even large structural energy differences (e.g. bcc vs. hcp Fe) by only a few meV/atom. Altogether the RC-PAW calculations confirm that the good agreement between FC-PAW and genuine AE calculations is real and not due to a cancellation of errors.

It has been emphasized above that the construction of accurate, transferable, and efficient pseudopotentials or PAW data sets is by no means a trivial task. Also, to allow to compare the results of different calculations, it is important that they have been executed with the same set of potentials. It is therefore important that the VASP package offers a complete set of thoroughly tested pseudopotentials and PAW data sets for all elements of the Periodic Table, from H to Pu. For many elements, a choice between soft and hard potential (requiring low or high cut-off energies, respectively) is offered, the selection may be made on the basis of the desired accuracy of the total energies and of the acceptable computational effort.⁵³

Relativistic effects

In the standard mode, VASP performs a fully relativistic calculation for the core-electrons and treats valence electrons in a scalar relativistic approximation. Spin-orbit coupling of the valence electrons may be included using the second-variation method⁵⁴ using the scalar-relativistic eigenfunctions of the valence states. The inclusion of spin-orbit coupling⁵⁵ allows a calculation of orbital moments, the determination of the easy axis of magnetization, and the calculation of magnetic anisotropy energies.

Iterative schemes for calculating the Kohn–Sham ground state

An argument that is often brought forward against the use of a plane-wave basis set is that the number of plane waves N_{PW} which must be used to achieve basis-set convergence is usually much larger than the number of basis functions used in minimal local basis sets. However, this argument fails because (i) the action of the Hamiltonian onto the trial wave functions can be evaluated very efficiently and (ii) modern iterative algorithms for the calculation of the Kohn–Sham ground state avoid the explicit calculation, storage and diagonalization of the $N_{PW} \times N_{PW}$ Hamiltonian. These methods fall into two distinctly different categories: (i) Direct methods based on the minimization of the Kohn–Sham total energy functional (either using the Car–Parrinello approach²⁶ based on a pseudo Newtonian equation of motion for the electronic degrees of freedom or by a conjugate-gradient minimization of the total energy^{56,57}). (ii) Iterative methods for a sequential updating the occupied and some empty eigenstates,

in conjunction with an iterative improvement of the charge-density or the potential (mixing) in a selfconsistency cycle (SC). Conceptually the direct methods are definitely more elegant than the SC methods that have been used for a very long time for molecular and solid-state calculations. However, the recent development has demonstrated that the SC methods are at least competitive with the direct minimization methods for semiconductors and insulators and that for metallic systems they definitely outperform any other scheme.^{33,34}

For the iterative calculation of the lowest Kohn–Sham eigenstates many different approaches may be used. Kresse and Furthmüller^{33,34} have analyzed in detail (i) the blocked Davidson scheme,⁵⁸ (ii) the sequential conjugate-gradient (CG) algorithm proposed by Teter et al.⁵⁶ for the minimization of the total energy and adapted by Bylander et al.⁵⁹ for the iterative diagonalization of the Hamiltonian, and (iii) a variant of the minimization of the norm of the residual vector to each eigenstate combined with a direct inversion in the iterative subspace (RMM-DIIS).^{60,61} An important criterion for the efficiency of any iterative approach is that the number of operations scaling with a higher power of N_{PW} (e.g. the orthogonalization of the eigenstates scaling as N_{PW}^3) is kept at a minimum. In the sequential CG algorithm attempting to minimize the Rayleigh quotient

$$\varepsilon_{m,\text{app}} = \frac{\langle \phi_m | \mathbf{H} | \phi_m \rangle}{\langle \phi_m | \mathbf{S} | \phi_m \rangle} \quad (13)$$

the orthogonalization has to be performed after each update of the eigenstate ϕ_m . In contrast, the residuum minimization method (RMM) proceeds by minimization of the norm of the residuum vector defined as

$$|R(\phi_m)\rangle = (\mathbf{H} - \varepsilon_{m,\text{app}}\mathbf{S})|\phi_m\rangle \quad (14)$$

if $\langle \phi_m | \mathbf{S} | \phi_m \rangle = 1$. The minimization of $\|R(\phi_m)\|$ is free of orthogonality constraints, it is sufficient to re-orthonormalize the eigenstates after updating all bands by performing a sub-space diagonalization. Minimization of the residuum is performed following Pulay⁶⁰ in the “iterative subspace” spanned by the search directions in a few successive iterations steps, pre-conditioning is used to improve convergence.^{33,34} A certain drawback of the RMM method is that it always converges to the minimum closest to the initial state; therefore, initialization is a critical step. Problems can be avoided by performing a sub-space rotation, i.e. a unitary transformation such that the Hamiltonian is diagonal in the subspace of all eigenstates included in the iterative scheme.

A very important step is an efficient pre-conditioned mixing of the input and output charge densities (the pre-conditioning serving to damp the mixing factor for the low-q Fourier components of the charge density where small changes in the charge lead to strong fluctuations in the Hartree potential). Different mixing strategies have been discussed by Kresse and Furthmüller.^{33,34} A very efficient routine is again based on a RMM-DIIS strategy based on the charge-density residual vector $R[\rho_{\text{in}}] = \rho_{\text{out}}[\rho_{\text{in}}] - \rho_{\text{in}}$ and a pre-conditioning based on a reasonable approximation to the charge dielectric matrix of the systems—for all details, I refer to the original

publications. There is also no room to discuss other important technicalities such as the method adopted for Brillouin-zone integrations, for which the manual provides a detailed description.⁵³

Because in the approach (which could only be crudely sketched above), all $O(N)^3$ operations (where N stands for the system size—the number of valence electrons being a more meaningful measure than the number of atoms) are reduced to their absolute minimum, the overall scaling of the computational effort remains close to $O(N)^2$ even for the largest systems tractable in *ab initio* DFT calculations. Because of the progress in computer performance, the limiting system size has been expanded considerably during the last years. At the moment, the practical limit for static calculations on medium-sized clusters is probably around 10^4 valence electrons. Calculations with VASP coming close to this limit are the calculations of Ramos et al.⁶² on carbon impurities in group-III nitrides using supercells with up to 2744 atoms (or even more than 10,000 valence electrons) per cell or the calculations of Kresse et al.⁶³ on ZnO(0001) surfaces, using very large supercells (up to $\sqrt{48} \times \sqrt{48}$ surface cells on slabs consisting of eight double layers of ZnO) containing more than 750 atoms (or nearly 7000 valence electrons). *Ab initio* molecular dynamics simulations can be performed for cells containing a few hundred atoms, extending over time-spans of up to 100 ps. An example are the investigations of Alfé on the coexistence of solid and liquid Al, based on *ab initio* MD for 1000 atoms.⁶⁴

Hierarchy of DFT functionals

The attempts to render DFT calculations ever more accurate have led to the development of an entire hierarchy of exchange-correlation functionals, which is sometimes referred to as the “Jacob’s ladder” of density functional theory.³ Concerning the construction of exchange-correlation functionals, there is a marked cultural difference between quantum chemists and solid-state theorists. In quantum chemistry, parameterized semi-empirical functionals, with the parameters adjusted to a given set of experimental data, enjoy a rather wide-spread popularity. An example for these functionals is the three-parameter B3LYP functional,¹⁵ which has been widely used in molecular quantum chemistry. Solid-state theorists on the other hand tend to despise empirical parameterizations and have concentrated on the development of ‘parameter-free’ functionals fitted only to correlation energies from Quantum Monte-Carlo (QMC) simulations for the homogeneous electron gas and to known sum-rules, scaling relations, and asymptotic relations for the many-electron system. The four rungs on Jacob’s ladder accessible so far are (i) the local density approximation (LDA), (ii) the generalized gradient approximation (GGA), (iii) the *meta*-GGA introducing in addition a dependence on the Laplacian of the electron density (i.e. on the density of the kinetic energy), and (iv) *hybrid* functionals mixing DFT and exact (Hartree-Fock) exchange. All functionals exist in a paramagnetic and in a spin-polarized version, all four levels of approximation are accessible within VASP.

Local (spin)-density approximation (L(S)DA) and generalized gradient approximation—GGA

At the level of the LDA, VASP uses a parameterization of the exchange-correlation functional by Perdew and Zunger,⁵ based on Quantum Monte-Carlo simulations for the homogeneous electron

gas by Ceperley and Alder.⁶⁵ The extension of the LDA to the spin-polarized case is based on the spin-interpolation proposed by Barth and Hedin⁶⁶ and by Vosko, Wills, and Nusair.⁶⁷ It is well known that the LDA tends to overestimate the bond strength in solids: the calculated lattice constants are too small, cohesive energies are overestimated, and energy gaps in semiconductors and insulators are seriously underestimated.

The GGA introduces a dependence of the exchange-correlation functional on the local gradient $\nabla n(\vec{r})$ of the electron density. For the exchange energy, the GGA has the form

$$E_x^{\text{GGA}}[n] = \int d^3r \varepsilon_x^{\text{unif}}(n(\vec{r})) F_x(s(\vec{r})), \quad (15)$$

where $\varepsilon_x^{\text{unif}}(n)$ is the exchange energy density of a uniform electron gas (proportional to $n^{4/3}$) and $s = |\nabla n| / (2k_F n)$ is the dimensionless density gradient ($k_F = (3\pi^2 n)^{1/3}$ is the Fermi wavevector). $F_x(s)$ is the so-called exchange enhancement factor characterizing the precise form of the GGA. A similar formulation may also be found for the correlation energy. GGA functionals implemented in VASP are the functional proposed by Perdew et al. in 1991 (PW91),⁶⁸ the Perdew-Burke-Ernzerhof (PBE)²⁰ functional and its revised form proposed by Hansen et al. (RPBE),⁶⁹ and the functional proposed by Armiento and Mattson (AM05).⁷⁰ The PW91 functional has been constructed using QMC data for the uniform electron gas and exact properties of the exchange-correlation hole. PBE presented a more elegant derivation of the functional using exact properties of the exchange-correlation energy. A slightly revised version of the PBE functional (modifying the exchange enhancement factor at intermediate values of s where it is not constrained by exact conditions) referred usually as RPBE⁶⁹ has been constructed with the aim to yield more realistic binding and adsorption energies. A GGA functional designed to include surface effects was developed by Armiento and Mattson (AM05).⁷⁰ A revised PBE density-functional that improves predictions of equilibrium properties of solids (PBEsol) was very recently proposed by Perdew et al.²⁵ The PW91, PBE, RPBE, PBEsol, and AM05 functionals are available with VASP. Extensive tests of various forms of the GGA on standard test sets of molecules and solids are available in the literature.^{37,50,70–74} The GGA corrects the overbinding tendency inherent in the LDA, albeit with a certain tendency to overcorrect: lattice constants are on average underestimated in the LSDA by about 1%, PBE overestimates them by nearly the same amount. Other equilibrium properties that are sensitive to the lattice constant such as bulk moduli, phonon frequencies, and magnetic moments are also sometimes over-corrected by the GGA.⁷¹ However, it must also be pointed out that the GGA produces the correct ground state for magnetic transition metals where the LSDA fails quite badly: in the LSDA, Fe is predicted to be hexagonal close-packed and nonmagnetic instead of body-centered cubic and ferromagnetic,⁷⁶ and body-centered cubic Cr is predicted to be nonmagnetic instead of antiferromagnetic.⁷⁷ For surface energies, the LSDA predictions are too low, but even lower values are produced in the GGA.⁷² For the adsorption energies of small molecules on solid surfaces, however, the lower values predicted by GGA are definitely superior to the LSDA results. For the adsorption on transition metals, the RPBE results come closer to

Table 1. Lattice constants a (in Å) and Bulk moduli B (in GPa) for Solids Calculated Using VASP and Various GGA Functionals.^{74,82}

Solid	a_{PBE}	B_{PBE}	a_{PBEsol}	B_{PBEsol}	a_{AM05}	B_{AM05}	$a_{\text{expt.}}$	$B_{\text{expt.}}$
Li	3.438	13.7	3.437	13.5	3.455	13.0	3.477	13
Na	4.200	7.80	4.174	7.88	4.212	7.36	4.225	8
Al	4.040	76.6	4.106	81.1	4.004	83.9	4.032	79
C	3.574	431	3.557	448	3.551	442	3.567	443
Si	5.469	87.8	5.436	93.2	5.431	90.2	5.430	99
LiF	4.068	67.3	4.013	73.1	4.039	65.8	4.010	70
MgO	4.258	150	4.222	156	4.232	152	4.207	165
Cu	3.635	136	3.569	164	3.565	157	3.603	142
Rh	3.830	254	3.780	294	3.773	285	3.798	269
Pd	3.943	166	3.877	203	3.872	194	3.881	195

experiment than PBE, but for adsorption on noble metals RPBE produces unrealistic results (endothermic adsorption energies).⁷⁵ The LDA produces wrong results for the potential-energy profiles for the dissociation of diatomic molecules on metallic surfaces (barriers in the entrance instead of the exit channel) which are corrected in the GGA.^{78,79}

In a few cases, LDA calculations yield better agreement with experiments than calculations using the GGA. Examples are layered crystals such as graphite and hexagonal boron nitride or molecular crystals where the binding between atomic layers or between molecules is based on van der Waals interactions only. In such cases, interlayer or intermolecular distances are in better agreement with experiment if the LDA has been used;^{73,80} however, it has to be pointed out that this is a mere artefact due to the overbinding inherent in the LDA and not a proper description of the physical binding mechanism (which is based on correlation effects which cannot be described within DFT, see also below).

Attempts to construct a GGA functional that improves total or cohesive energies and bond lengths or lattice constants to the same extent meet a dilemma highlighted recently by Perdew and coworkers.^{25,81} An enhanced gradient dependence improves total energies,⁶⁹ while a reduced gradient dependence improves lattice constants but worsens energetics.^{71,73} Perdew et al.²⁵ have pointed out that the dilemma arises from the limiting behavior of the exchange enhancement factor for small s , any GGA recovering the uniform electron gas limit has

$$F_x(s) = 1 + \mu s^2 + \dots \quad (s \rightarrow 0). \quad (16)$$

For slowly varying densities, the gradient expansion is accurate for $\mu = \mu_{\text{GE}} = 10/81 \sim 0.1234$. On the other hand, the asymptotic behavior of the exchange energy for heavy atoms is well described by $E_x = -0.2208Z^{5/3} - 0.196Z + \dots$. To recover the second term which arises from the s^2 term in the expansion of the enhancement factor requires $\mu \sim 2\mu_{\text{GE}}$. This condition is almost met by the PBE functional, although the value of $\mu = 0.2195$ was determined by another argument. A similar analysis may be performed for the correlation contribution. Perdew et al.²⁵ proposed a new GGA functional for solids, called PBEsol, where the exchange-enhancement factor is density-dependent, i.e. $F_{xc} = F_{xc}(r_s, s)$, where r_s is the usual electron radius and where the gradient-dependence is reduced

at low densities. PBEsol has recently been implemented in VASP,⁸² a few representative results for the lattice constants for solids are compiled in Table 1.

A larger compilation may be found in the papers by Mattson et al.⁷⁴ and Paier et al.⁸² For the lattice constants, the mean relative error (MRE) for this larger set of solids is reduced from 0.83% with the PBE functional to -0.27% (PBEsol) and -0.04% (AM05), for the bulk modulus MRE = -8.6% (PBE), 0.1% (PBEsol), and -3.1% (AM05). The price for the significant improvement for lattice constants and bulk moduli is, however, a reduced accuracy of the calculated atomization energies. The AM05 functional performs similar to PBEsol, but it should be pointed out that the PBEsol correctly respects the Lieb-Oxford bound (lower limit to the exchange-correlation energy), while the AM05 functional does not.

Meta-GGA

The meta-GGA is a straightforward extension of the concept underlying the GGA—in addition to the dependence on the local density $n(\vec{r})$ and its gradient $\nabla n(\vec{r})$, the meta-GGA functional depends also either on the Laplacian of the electron density $\Delta n(\vec{r})$ or on the local kinetic energy density $\tau(\vec{r})$ defined as

$$\tau(\vec{r}) = \frac{1}{2} \sum_{k=1}^N |\nabla \psi_k(\vec{r})|^2, \quad (17)$$

where the summation extends over all occupied Kohn-Sham eigenstates. Meta-GGA functionals using the kinetic energy density $\tau(\vec{r})$ depend explicitly on the orbitals. Again, the many meta-GGA functionals proposed in the literature may be divided into semi-empirical parameterized functionals (such as that proposed by Voorhis and Scuseria⁹) and functionals following the philosophy of the PBE-GGA and attempting to eliminate adjustable parameters as far as possible. An example is the PKZB functional proposed by Perdew et al.,¹⁸ which may be cast into the form of an exchange enhancement factor which reduces in the limit of a slowly varying density to a fourth-order gradient expansion⁸³ depending on the square of the reduced density gradient and the reduced Laplacian of the density. An improved form of the meta-GGA has been proposed by Tao et al. (TPSS).^{17,21,23} Molecular tests²² proved a substantial improvement

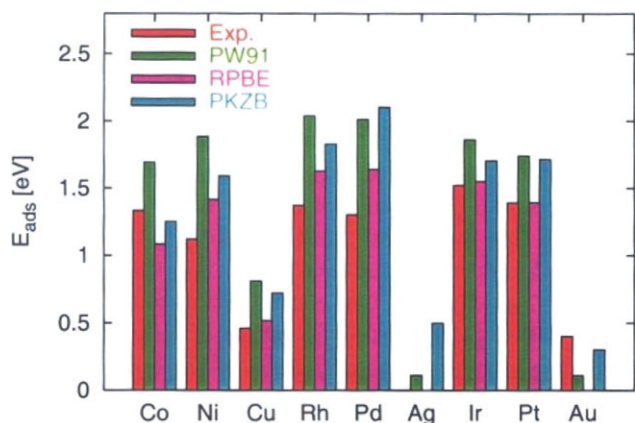


Figure 3. Comparison adsorption energies of CO on the (111) surfaces of transition metals, calculated using the GGA (PW91, RPBE), and meta-GGA (PKZB). Cf. text. After Hirschl.⁸⁴ [Color figure can be viewed in the online issue, which is available at www.interscience.wiley.com.]

of atomization energies, while for lattice constants and bulk moduli of solids the performance of the PKZB and TPSS meta-GGA's is essentially on par with the PBE results.^{21,23}

The PKZB meta-GGA has also been implemented in VASP, and extended tests for molecules and solids have been performed by Hirschl.⁸⁴ The implementation is non-selfconsistent (as in the work of PKZB), i.e., the meta-GGA corrections are calculated a posteriori with PBE orbitals. However, Tao et al.^{17,21} have emphasized that self-consistency does not significantly alter the conclusions. For small molecules, the meta-GGA leads to significant improvements of the atomization energies, but for solids the results are more ambiguous, in agreement with the conclusions of TPSS.

Hirschl also made an attempt to apply the meta-GGA to surface-science problems. For the adsorption of small molecules on the surfaces of transition- and noble metals the results are ambiguous. Energies for CO adsorption on transition metals are reduced compared to the GGA (PW91 or PBE) results (but not as much as for the RPBE functional which leads to better agreement with experiment— see Fig. 3). On noble metal surfaces the difference between the PW91 and the PKZB results is more modest, both are in reasonable agreement with experiment, whereas for Ag and Au the RPBE predicts endothermic adsorption energies. For the dissociative adsorption of hydrogen molecules on Pd surfaces, serious differences appear between PBE results on one side and the meta-GGA results on the other side. Potential-energy profiles from LDA and GGA calculations^{85,86} predict that dissociation is a nonactivated process, with a dynamic precursor in the entrance channel, in agreement with experiment. The RPBE functional and the PKBZ meta-GGA strongly reduce the binding between adsorbate and substrate—not only for the dissociated product, but already for the approaching molecule. As a result, the barrier separating the precursor and the final state is increased and dissociation is predicted to be an activated process (see Fig. 4).

Mittendorfer et al.⁸⁷ have applied both GGA and meta-GGA calculations to study the stepwise hydrogenation of benzene to

cyclohexene, both in the gas-phase and catalyzed on a Ni(111) surface. In the gas-phase the energy differences between the different cyclic hydrocarbon species (benzene, cyclohexadiene, cyclohexene) are correctly described only in the meta-GGA, while for the adsorbed species only minimal differences exist between the GGA and meta-GGA predictions. This suggests that the main merit of the meta-GGA is to predict more accurate energy differences between single and double bonds, while for the adsorbed species where the hybridization with the substrate reduces the difference between single and double bonds and between aromatic and non-aromatic behavior the meta-GGA corrections are less significant.

I have included these last results to emphasize the point that the calculation of a number of simple ground-state properties of an even rather extensive set of atoms, molecules, and solids should not be considered as a final assessment of the quality of a functional. If applications are extended to more complex situation, some surprising results might appear.

Hybrid functionals

Hybrid functionals are characterized by mixing nonlocal Fock exchange and local or semilocal DFT exchange in a certain proportion. The construction of hybrid functionals is motivated by the fact that the deficiencies of DFT and HF are in some sense complementary: band gaps predicted by DFT are too narrow, gaps calculated using HF are far too wide. Hence there is some hope that a mixed functionals may not only predict more accurate gaps, but also lead to more accurate total energies and geometries. The mixing of HF and DFT exchange energies may also be justified to some extent by the adiabatic connection formula (ACF) for the exchange energy.^{88,89} The most popular hybrid is the three-parameter B3LYP functional^{15,16} mixing 80% of LDA with 20% of HF exchange (adding a certain amount of Becke's correction, ΔE_x^{B88}), and mixing in the correlation part 19% of the Vosko-Wilk-Nusair (VWN) functional⁶⁷ with 81% of Lee-Yang-Parr⁹⁰ correlation (note that these exchange and correlation functionals in turn contain some empirical parameters),

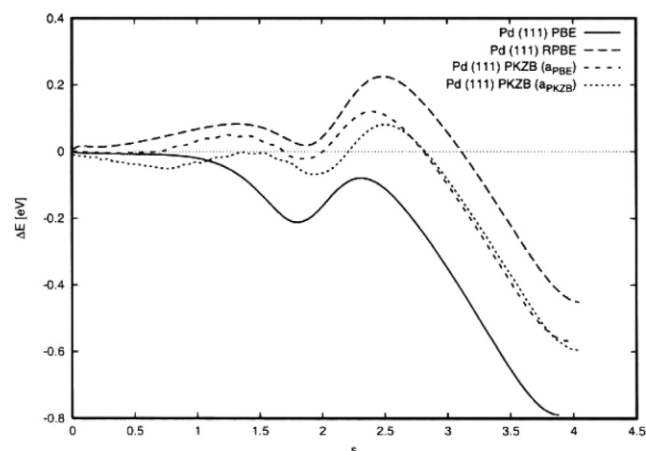


Figure 4. Potential energy profile for the dissociative adsorption of a hydrogen molecule on a Pd(111) surface, calculated using the GGA (PW91, RPBE) and meta-GGA (PKZB). Cf. text. After Hirschl.⁸⁴

$$E_{xc}^{B3LYP} = 0.8E_x^{LDA} + 0.2E_x^{HF} + 0.72\Delta E_x^{B88} + 0.19E_c^{VWN} + 0.81E_c^{LYP}. \quad (18)$$

The mixing coefficients have been determined by a fit to a test set of molecules, and the B3LYP functional enjoys an enormous popularity in molecular quantum chemistry. However, it has to be pointed out that the correlation part of the functional is incorrect in the limit of the homogeneous electron gas.

An attempt to reduce the degree of empiricism has been made with the PBE0 and HSE03 functionals. The PBE0 functional²⁰ mixes $\frac{1}{4}$ of exact (HF) exchange with $\frac{3}{4}$ of PBE exchange, and describes correlation in the GGA (PBE),

$$E_{xc}^{PBE0} = 0.25E_x^{HF} + 0.75E_x^{PBE} + E_c^{PBE}. \quad (19)$$

For molecular systems, the improvement achieved with the PBE0 functional is well documented,^{21,91} and it can be attributed to the fact that an admixture of a certain part of exact exchange reduces the self-interaction error of DFT.⁹² Under periodic boundary conditions the calculation of the HF exchange energy is very expensive because of the slow decay of the exchange interaction with distance. To avoid this difficulty Heyd et al.⁴⁹ proposed to separate the Coulomb kernel into a short- and long-range part,

$$\frac{1}{r} = S_\mu(r) + L_\mu(r) = \text{erfc}(\mu r)/r + \text{erf}(\mu r)r, \quad (20)$$

where μ is the range-separation parameter determining the distance (equal to $\sim 2/\mu$) beyond which the short-range interaction becomes negligible. In the HSE03 functional, the mixing of HF and DFT exchange is applied only to the short-range interaction, i.e.,

$$E_{xc}^{HSE03} = 0.25E_x^{sr, HF} + 0.75E_x^{sr, PBE} + E_x^{lr, PBE} + E_c^{PBE}. \quad (21)$$

It has been established empirically that $\mu \sim 0.2 \rightarrow 0.3 \text{ \AA}^{-1}$ is a good universal choice of the range-separation parameter. The mixing ratio adopted in the PBE0 and HSE03 functional is not the result of a fitting—it has been argued⁹³ that this ratio is suggested by the result of a coupling constant integration between the HF and DFT limit.

All three hybrid functionals discussed above (B3LYP, PBE0, HSE03) have been implemented in VASP.^{19,37,50} The implementation of Hartree-Fock exchange in a plane-wave code using the PAW method is by no means trivial. The first task is the representation of the exchange energy in the PAW formalism. To treat the long-range electrostatic interactions it is necessary to introduce an additional quantity, the compensation density $n^C(\vec{r})$ which is chosen in such a way that the sum of the pseudo on-site charge and of the compensation charge density, $n^{PS,1}(\vec{r}) + n^C(\vec{r})$, has exactly the same moments as the all-electron charge density $n^{AE,1}(\vec{r})$ within each PAW sphere - this implies that the electrostatic potential associated with $n^{AE,1}(\vec{r})$ is identical to that of $n^{PS,1}(\vec{r}) + n^C(\vec{r})$ outside the spheres. A separable representation of the exchange energy, with three noninteracting terms based on the pseudo orbitals represented by plane waves, and on AE and PS orbitals represented on radial support grids may be

based on the decomposition of the charge density related to two AE orbitals Ψ_a^{AE} and Ψ_b^{AE} , $n_{ab}(\vec{r}) = \langle \Psi_a^{AE} | \vec{r} \rangle \langle \vec{r} | \Psi_b^{AE} \rangle$ according to³⁷

$$n_{ab}(\vec{r}) = [n_{ab}^{PS}(\vec{r}) + n_{ab}^C(\vec{r})] + n_{ab}^{AE,1}(\vec{r}) - [n_{ab}^{PS,1}(\vec{r}) + n_{ab}^C(\vec{r})], \quad (22)$$

i.e., by adding and subtracting the compensation charge from the expression for the total charge density. A further problem arises from the singularity of the Fourier-transformed Coulomb potential at $\vec{G} = 0$. Setting $V(\vec{G}) = 0$ is equivalent to the assumption of a compensating uniform background charge and leads to slow convergence with respect to the size of the computational cell. In VASP, this problem is solved, following Massida and Posternak⁹⁴ and Makov and Payne,⁹⁵ by calculating the electrostatic energy between periodically repeated point charges and a compensating background and subtracting the self-energy of an isolated point charge, i.e., $V(\vec{G})$ is given by the energy difference between an isolated and a periodically repeated charge, divided by the cell volume.³⁷

Still, calculations using hybrid functionals mixing DFT, and Hartree-Fock in a plane-wave basis require a very fine k -point mesh in the Brillouin zone to achieve convergence of the Fock exchange energy.⁵⁰ In this respect, the screening of the long-range interactions in the HSE03 functional offers a significant computational advantage, as it allows a “downsampling” of the short-range Fock interactions on a considerably coarser grid.

The computational cost scales with the square of the number of occupied bands N_{bands} times the number of k -points, N_k , multiplied by the cost for a single fast Fourier transform $N_{\text{FFT}} \ln N_{\text{FFT}}$ where N_{FFT} is the number of grid points for the FFT. Hence the entire calculation scales as

$$(N_{\text{bands}} N_k)^2 N_{\text{FFT}} \ln N_{\text{FFT}}. \quad (23)$$

However, as for solids $N_{\text{bands}} \propto N_{\text{atoms}}$, $N_k \propto 1/N_{\text{atom}}$ and $N_{\text{FFT}} \propto N_{\text{atoms}}$, the computational efforts scales linearly with the number of atoms, as long as with an increasing cell size the number of k -points can be reduced in proportion.

Details on the CPU-timings of GGA and hybrid functional calculations with VASP and GAUSSIAN03 have been given by Paier et al.³⁷ The timing ratio between PBE and PBE0 calculations for small molecules is about 2 for plane-wave calculations. For this case, plane-wave calculations with a very large basis set (cut-off energy 1000 eV) and the local aug-cc-pVQZ basis set perform roughly equal, while with the aug-cc-pV5Z basis required to match the fully converged plane-wave results the computational effort is already much higher at the PBE level and the PBE0/PBE timing ratio also increases to about five. To be honest, it has to be pointed out that the GAUSSIAN03 calculations are all-electron calculations, while the VASP calculation are full potential valence only calculations. This makes the calculations with local basis sets particularly expensive for heavy molecules - with the advantage if increased precision (but see the section on relaxed-core PAW). For solids, the screening of the Fock-exchange in the HSE03 functional allows to restrict Brillouin-zone sampling: Typically a $(6 \times 6 \times 6)$ mesh of k -point is sufficient to achieve converged results for total energies, even in metals, whereas at least a $(12 \times 12 \times 12)$ mesh is required if the bare exchange operator is used.⁵⁰

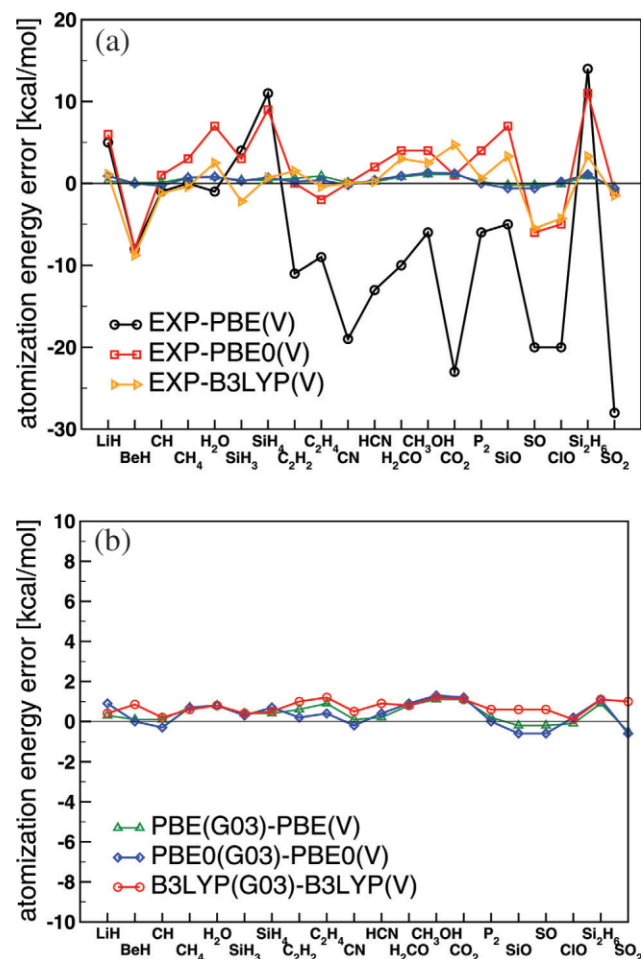


Figure 5. (a) Comparison of the error in the calculated atomization energies of small molecules calculated using VASP and the PBE, PBE0, and B3LYP functionals. Part (b) confronts the results of calculations using VASP and GAUSSIAN, using the same set of functionals. After Paier et al.^{19,37} [Color figure can be viewed in the online issue, which is available at www.interscience.wiley.com.]

The implementation of Hartree-Fock exchange and of hybrid functionals in VASP has been thoroughly tested for molecular and solid-state systems against calculations with local basis sets (using GAUSSIAN03 and Gaussian-type orbitals). As an example

Figure 5 compares the atomization energies of small molecules, calculated using VASP and the PBE, PBE0 and B3LYP functionals, part (b) of the figures compares the results for the same three functionals achieved using VASP and GAUSSIAN03. The differences between the plane-wave and the local-basis-set results never exceeds 1 kcal/mol. Both hybrid functionals achieve a significantly improved accuracy of the predicted atomization energies.

For solids the performance of hybrid functionals is more ambiguous. The first observation is that the PBE0 and HSE03 hybrid functionals predict more accurate lattice constants and bulk moduli for most solids than standard GGA functionals, whereas on average the B3LYP results are at best on par with the GGA results (a few selected results are listed in Table 2, for a more complete listing I refer to the original publications). Results obtained using PBE0 and HSE03 are essentially on par—this demonstrates that the screening of the long-range exchange is legitimate and that the computational advantages of the HSE03 should be exploited. For the B3LYP functional one has to differentiate between different types of solids: whereas the predicted lattice constants are more accurate than the PBE results for ionic solids (MgO) and, to a lesser extent, for large-gap semiconductors (diamond), they are definitely less accurate for transition metals.

For the atomization energies, the overall accuracy achieved with hybrid functionals is lower than at the PBE level (see Fig. 6). For a representative set of 21 solids (metals, semiconductors, and insulators), the mean absolute relative error (MARE) is 3.4%, 6.3%, 7.4% and 17.6% for the PBE, PBE0, HSE03, and B3LYP functionals. If metals are excluded, the MARE are reduced to 3.4%, 3.6%, 3.6%, and 8.0%, respectively.¹⁹ These results show that for nonmetals, the performance is comparable for the PBE, PBE0, and HSE03, while B3LYP definitely under-performs compared to all functionals. For metals, the performance of all hybrid functionals is unsatisfactory. For the PBE0 and HSE03 functionals, the reason for the reduction of the atomization energy is likely associated with the overestimation of the stability of the spin-polarized atom, arising from an overestimation of the exchange-splitting.⁵⁰ For the B3LYP functional the performance is further reduced because the LYP correlation energy fails to correctly describe the homogeneous electron gas. Better results are achieved for the heats of formation of insulating solids, where the reference is not the isolated atom, but the elemental solid.

A main failure of DFT calculations is the pronounced underestimation of the band gaps in semiconductors and insulators—in this respect the GGA does not represent any advantage over the LDA. The admixture of screened HF exchange in the HSE03 functional

Table 2. Lattice Constants a (in Å) and Bulk Moduli B (in GPa) of Selected Solids, Calculated using VASP and the PBE, PBE0, HSE03, and B3LYP functionals (after Paier et al.^{19,50}).

Solid	a_{PBE}	B_{PBE}	a_{PBE0}	B_{PBE0}	a_{HSE03}	B_{HSE03}	a_{B3LYP}	B_{B3LYP}	$a_{\text{expt.}}$	$B_{\text{expt.}}$
C	3.574	432	3.550	466	3.549	467	3.569	443	3.567	443
Si	5.469	87.8	5.439	96.5	5.433	99.0	5.478	90.2	5.430	99.2
GaAs	5.752	59.9	5.696	69.5	5.672	72.9	5.772	62.4	5.648	75.6
MgO	4.258	149	4.212	168	4.211	169	4.212	162	4.207	165
Na	4.200	7.80	4.225	8.45	4.229	8.22	4.203	7.12	4.225	7.50
Al	4.040	76.6	4.025	81.1	4.102	86.0	4.058	66.8	4.032	79.4
Rh	3.830	254	3.786	285	3.785	291	3.851	239	3.798	269
MAE	0.045	12.4	0.024	8.6	0.022	7.9	0.040	9.7		

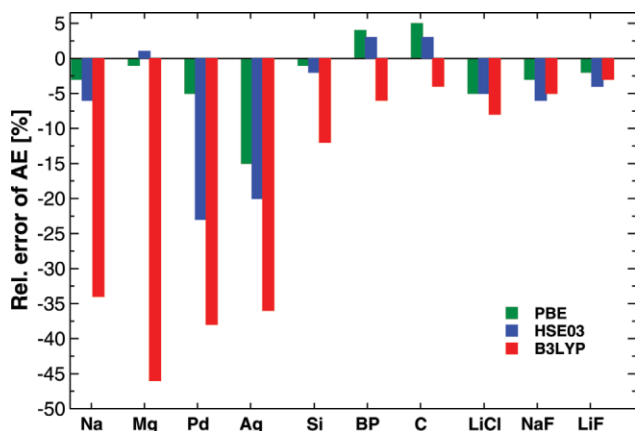


Figure 6. Comparison of the error in atomization energies of a few selected solids calculated using VASP and the PBE, HSE03, and B3LYP functionals. After Paier et al.^{19,37} [Color figure can be viewed in the online issue, which is available at www.interscience.wiley.com.]

dramatically improves band-gaps—most notably for narrow- and medium-gap semiconductors, while for large-gap insulators, the band gaps are still underestimated (see Fig. 7). Detailed HSE03 calculations for lead chalcogenides⁹⁶ have produced excellent results for structural properties, band-gaps and effective masses. The failure for large-gap systems is clearly due to the fact that in these systems the non-local exchange should approach the unscreened Fock exchange. PBE0 calculations overestimate the gap for small-gap systems (the shift is almost uniformly 0.8 eV), but still underestimate it for large-gap systems where many-body corrections are required (see below).

Severe problems arise if hybrid functional are applied to itinerant magnetic metals. For Fe, for example, the magnetic moments increases from a PBE value of $2.2 \mu_B$ (in perfect agreement with experiment) to $2.7 \mu_B$, accompanied by a strong overestimation of the exchange splitting and a broadening of the valence band.⁵⁰ The broadening of the d-band exists also in non-magnetic d-metals. As a consequence, hybrid functionals still fail to correct the failure of DFT to describe the adsorption of CO on some transition-metals (Cu, Rh, Pt—adsorption is predicted in a threefold hollow instead of in an on-top geometry). It had been shown that when the HOMO-LUMO gap of the adsorbate is increased to its correct value, while retaining a PBE description of the substrate, the correct result is achieved.⁹⁷ A hybrid functional corrects the HOMO-LUMO gap of the CO molecule, but unphysically broadens the d-band—as a result the correct adsorption site is still not found for Pt.⁹⁸ The conclusion—as has already been emphasized at the end of the paragraph on meta-GGAs is that an assessment of the usefulness of a functional requires more than a calculation of lattice constants and atomization energies.

Recent applications to solids where standard semi-local functionals do not provide a satisfactory description have dealt mostly with rare-earth and transition-metal oxides which are insulating and antiferromagnetic and where GGA calculations seriously underestimate both the band gap and the exchange splitting: CeO_x ,⁹⁹ MnO_x .^{100,101} The results demonstrate that hybrid functionals cure both defects.

Range-separated hybrid functionals

A shortcoming of DFT functionals that is only partially corrected by hybrid functionals is the incorrect long-range behavior of the exchange-correlation potential. In atoms and molecules, the xc potential of semilocal functionals decays exponentially, while the asymptotic form of the exact xc potential is $-1/r$.¹⁰² For hybrid functionals mixing exact and GGA exchange, the xc potential decays asymptotically as $-a/r$ where a is the fraction of Hartree-Fock exchange. To recover the exact $-1/r$ asymptote, it has been suggested to separate the Coulomb kernel into a short- and long-range part, as described above for the HSE03 functional, but now to replace the long-range part of the DFT exchange by the Hartree-Fock counterpart. Hence a *range-separated* or *long-range corrected* (LC) hybrid functional is defined as^{103–106}

$$E_{xc}^{\text{LC-DFT}} = E_x^{\text{sr,DFT}} + E_x^{\text{lr,HF}} + E_c^{\text{DFT}}, \quad (24)$$

where DFT stands for any possible flavor of DFT (LDA, GGA,...). Both the long- and short range parts of the exchange interaction depend of course on the value of the separation parameter Vydrov and Scuseria¹⁰⁶ have demonstrated that a long-range corrected PBE functional (LC-PBE) is remarkably accurate for a broad range of molecular properties, including activation energies of chemical reactions and processes involving long-range charge transfer such as the dissociation of ionic diatomics. However, it has also been pointed out¹⁰⁷ that, as the description of long-range correlation is not improved at the same time, the LC or range-separated hybrid functionals produce HOMO-LUMO gaps approaching the HF values (and hence grossly overestimated).

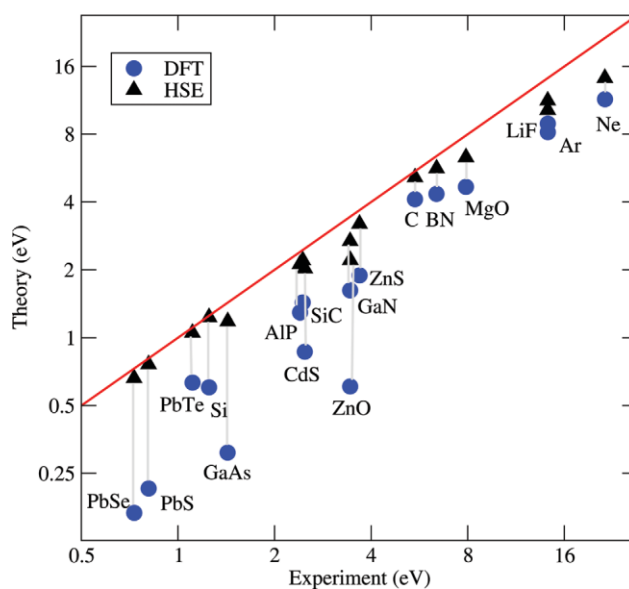


Figure 7. Comparison of band gaps in semiconductors and insulators, calculated using the PBE and HSE03 functionals. After Paier et al.^{19,37} [Color figure can be viewed in the online issue, which is available at www.interscience.wiley.com.]

The implementation of Hartree-Fock exchange in VASP³⁷ also allows to apply LC-hybrid functionals to solids. Gerber et al.¹⁰⁸ have demonstrated that even a LC-LDA yields improved structural parameters, but the study also demonstrates that band gaps in semiconductors are strongly overestimated. Only for large gap insulators (NaCl, Ar), the LC-hybrid functional predicts also reasonable gap-widths. For the moments the conclusion must be that to realize further progress with long-range corrected hybrid functionals, a better description of long-range correlation must be achieved.

Spin-polarized DFT—collinear and noncollinear magnetic ordering

All levels of DFT are available in VASP also in a spin-polarized version. For the exchange part of the functional, the spin-polarized version may be derived straightforwardly from the general spin-scaling relation

$$E_x^{\text{SDFT}}[n_\uparrow, n_\downarrow] = \frac{1}{2}(E^{\text{DFT}}[2n_\uparrow] + E^{\text{DFT}}[2n_\downarrow]). \quad (25)$$

The correlation energy of the spin-polarized homogeneous electron gas may be evaluated in the random-phase approximation,^{66,67} the result may be written as a function of the fractional spin polarization ζ ,

$$\zeta = \frac{n_\uparrow - n_\downarrow}{n_\uparrow + n_\downarrow} \quad (26)$$

as

$$E_c^{\text{SDFT}} = \int d^3r \varepsilon_c(n(\vec{r}), \zeta(\vec{r})), \quad (27)$$

where $\varepsilon_c(n, \zeta)$ is the correlation energy of the spin-polarized electron gas. For an explicit expression, see ref. 67. Spin-polarization has been implemented in VASP at all levels of the DFT hierarchy.

We have already emphasized that for itinerant magnets, only the GGA leads reliable and accurate results^{76,77} while the LDA predicts often the wrong ground state. Hybrid functionals tend to overestimate magnetic moments and exchange splitting, because in metallic systems the screening of the HF exchange is underestimated. For systems with local magnetic moments such as the insulating antiferromagnetic transition-metal oxides, the GGA underestimates the exchange-splitting quite severely, while hybrid functionals or the DFT + U approach (vide infra) lead to improved results.^{99–101}

In most magnetically ordered (ferro-, ferri-, or antiferromagnetic) systems the spin-moments on all sites are aligned (“collinear”). Noncollinear magnetic ordering may arise from a topological frustration of exchange interactions (e.g., the frustration of antiferromagnetic interactions on triangular or Kagomé lattices¹⁰⁹), the competition between spin- and orbital magnetism,¹¹⁰ from competing ferromagnetic and antiferromagnetic interactions in disordered alloys.¹¹¹ Noncollinear magnetism was first implemented in DFT calculations by Kübler et al.¹¹² The original implementation was based on an atomic-sphere approximation, assuming fixed spin-quantization axes in each atomic sphere. A fully unconstrained approach to noncollinear magnetism, based on

a vector-field description of the magnetization and of the exchange field was first attempted by Oda et al.¹¹³ within a plane-wave pseudopotential scheme and implemented with the PAW approach used in VASP by Hobbs, Kresse and Hafner.¹¹⁴

For the description of noncollinear magnetism, DFT is expressed in terms of a 2×2 density matrix $n^{\alpha\beta}(\vec{r})$. The electron density is given by the trace of the density matrix,

$$\text{Tr}[n^{\alpha\beta}(\vec{r})] \equiv n_{\text{Tr}}(\vec{r}) = \sum_\alpha n^{\alpha\alpha}(\vec{r}) \quad (28)$$

while the magnetization density $\vec{m}(\vec{r})$ is given by

$$\vec{m}(\vec{r}) = \sum_{\alpha\beta} n^{\alpha\beta}(\vec{r}) \cdot \vec{\sigma}^{\alpha\beta}, \quad (29)$$

where $\vec{\sigma} = (\sigma_x, \sigma_y, \sigma_z)$ is the vector of the Pauli spin matrices. The exchange-correlation energy is a functional of the electron density and of the magnetization field,

$$E_{\text{xc}}[n^{\alpha\beta}] = \int n_{\text{Tr}}(\vec{r}) \varepsilon_{\text{xc}}[n^{\alpha\beta}(\vec{r})] d\vec{r} \quad (30)$$

$$= \int n_{\text{Tr}}(\vec{r}) \varepsilon_{\text{xc}}[n_{\text{Tr}}(\vec{r}), |\vec{m}(\vec{r})|] d\vec{r}. \quad (31)$$

The exchange-correlation potential consists of a scalar contribution

$$v_{\text{xc}}[n^{\alpha\beta}](\vec{r}) = \frac{\delta E_{\text{xc}}[n^{\alpha\beta}]}{\delta n_{\text{Tr}}(\vec{r})} \quad (32)$$

$$= \varepsilon_{\text{xc}}[n^{\alpha\beta}](\vec{r}) + n_{\text{Tr}}(\vec{r}) \frac{\partial \varepsilon_{\text{xc}}[n^{\alpha\beta}(\vec{r})]}{\partial n_{\text{Tr}}(\vec{r})} \quad (33)$$

and of the magnetic exchange-correlation field

$$\vec{b}[n^{\alpha\beta}](\vec{r}) = \frac{\delta E_{\text{xc}}[n^{\alpha\beta}]}{\delta \vec{m}(\vec{r})} \quad (34)$$

$$= \vec{e}(\vec{r}) n_{\text{Tr}}(\vec{r}) \frac{\partial \varepsilon_{\text{xc}}[n^{\alpha\beta}(\vec{r})]}{\partial |\vec{m}(\vec{r})|}, \quad (35)$$

where $\vec{e}(\vec{r}) = \frac{\partial |\vec{m}(\vec{r})|}{\partial \vec{m}(\vec{r})}$ is the local direction of the magnetization at the point \vec{r} . Details of the generalization of the PAW equation to the density-matrix formulation have been given by Hobbs et al.¹¹⁴ A special type of noncollinear magnetic structures are spin spirals or helical spin waves. For spin-spirals Herring has demonstrated that by applying generalized Bloch conditions the calculations may be performed for the unit cell of the underlying crystal lattice.^{115,116}

VASP has been used to investigate noncollinear magnetism in small magnetic clusters,¹¹⁴ in ultrathin triangular antiferromagnetic films,¹¹⁷ at frustrated ferro/antiferromagnetic interfaces,¹¹⁸ and in antiferromagnetic α -Mn.¹¹⁹ As an example Figure 8 shows the noncollinear antiferromagnetic structure in the 58-atom unit cell of

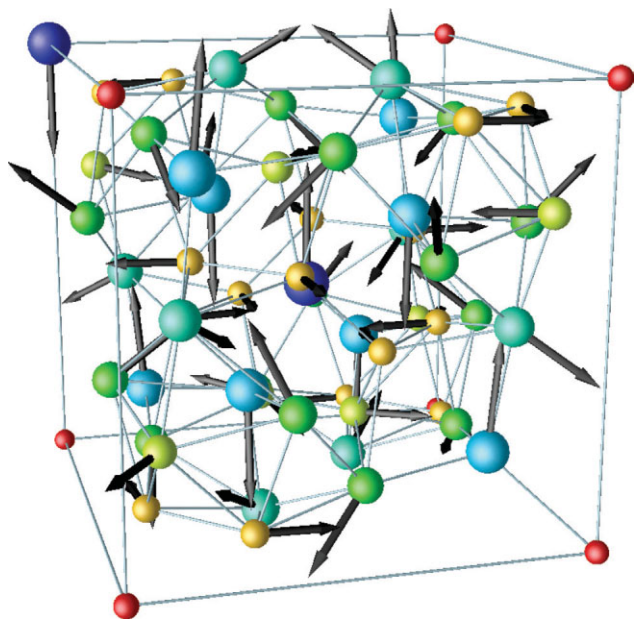


Figure 8. Noncollinear magnetic structure of α -Mn. Different colors distinguish crystallographically inequivalent sites, the length of the arrows is proportional to the magnitude of the local magnetic moments. The noncollinearity of the magnetic structure is triggered by the frustration of the antiferromagnetic interactions in triangles of the Mn-IV atoms shown in yellow. After Hobbs et al.¹¹⁹, Cf. text.

α -Mn which is in good agreement with the results of magnetic neutron scattering.¹²⁰ The noncollinearity of the spin-moments results from the frustrated antiferromagnetic coupling in Mn-triangles with short interatomic distances. Note that in this case antiferromagnetic ordering is accompanied by a small tetragonal distortion of the body-centered cubic structure which is also correctly described by the calculations.

Spin-spiral structures have been investigated in body-centered cubic δ -Mn^{M8} and in face-centered cubic γ -Fe^{M6}. In this case the broken crystalline and magnetic symmetries are strongly correlated and it has been demonstrated that the experimentally observed spin-spiral structure with a propagation vector $\vec{q} = 2\pi/a \times (0.1, 0, 1)$ can be found only if an unconstrained vector-field description of magnetization is used.¹¹⁶

Beyond density-functional theory

Even after climbing to the highest rung of John Perdew's "Jacob's ladder," DFT does not solve all problems. Examples are strongly correlated materials (d- and f-electron systems with narrow bands), excited states in semiconductors and insulators, and dispersion forces in rare-gas solids or molecular crystals. In all cases, it is necessary to go beyond DFT—in the following, I describe very briefly the post-DFT capabilities implemented in VASP.

Correcting on-site Coulomb repulsions—DFT+U

In DFT, the orbital-dependence of the exchange correlation energy is rather weak. In many cases, this is appropriate, but in systems with narrow 3d- or 5f-bands and localized orbitals, DFT fails to account

for the strong Coulomb repulsion between electrons occupying these narrow bands, which leads to an enhanced exchange splitting between occupied and empty eigenstates. The DFT+U method attempts to cure this defect by adding a Hubbard-type Coulomb repulsion to the DFT Hamiltonian. Many versions of the DFT+U have been presented in the literature, the implementation in VASP is based on the work of Dudarev¹²¹ and Liechtenstein,¹²² using the spin-dependent on-site density matrix ρ_{ij}^σ to define the DFT+U energy functional as

$$E_{\text{DFT+U}} = E_{\text{DFT}} + \frac{U-J}{2} \sum_{\sigma} \text{Tr}[\rho^{\sigma} - \rho^{\sigma} \rho^{\sigma}], \quad (36)$$

where the Hubbard parameter U , $U = E(d^{n+1}) + E(d^{n-1}) - E(d^n)$, measures the increase in energy caused by placing an additional electron into a particular site, and J is a screened Stoner-like exchange parameter. Note that in this formulation the Hubbard-like part of the Hamiltonian is rotationally invariant. If the density matrices are idempotent, $(\rho^{\sigma})^2 = \rho^{\sigma}$, i.e. for a completely empty or a full band, the energy is given by the DFT alone. The one-electron potential is given by the variational derivative of the total energy with respect to the density,

$$V_{ij}^{\sigma} = \frac{\delta E_{\text{DFT+U}}}{\delta \rho_{ij}^{\sigma}} = \frac{\delta E_{\text{DFT}}}{\delta \rho_{ij}^{\sigma}} + (U-J) \left[\frac{1}{2} \delta_{ij} - \rho_{ij}^{\sigma} \right], \quad (37)$$

i.e., relative to the DFT eigenvalues the energies of occupied states are lowered by $-(U-J)/2$ and increased by $(U-J)/2$ for unoccupied states. The implementation of the DFT+U approach in the PAW formalism of VASP follows Bengone et al.,¹²³ for details see Rohrbach et al.¹²⁴ The DFT+U capability of VASP has been applied to transition-metal sulphides,¹²⁴ transition-metal oxides^{125–127} and to f-electron systems.¹²⁸ The DFT+U is a semi-empirical approach, because the Hubbard parameter U is an adjustable parameter. However, it has been shown that if the Hubbard correction is applied to spin-polarized GGA calculations, good agreement for lattice parameters, magnetic moments, band gap and exchange splitting can be achieved with a single value of U . If, as often reported in the literature, the DFT+U is applied on the basis on non-spinpolarized LDA or GGA results, a much larger value of U is required to reproduce the experimentally observed exchange splitting, spoiling the agreement for the lattice parameters and other volume-dependent quantities. To some extent, the DFT+U approach has been superseded by hybrid-functional calculations - however, it has still the advantage of a much lower computational effort.

Many-body perturbation theory—The GW approach

The accurate calculation of excitation spectra (i.e. of quasiparticle energies) is a long-standing problem of solid-state theory. That DFT fails to correctly predict excited state energies is not surprising, since there is no formal justification to interpret DFT eigenvalues for unoccupied states as quasiparticle energies. A widely used approach to quasiparticle energies and spectral functions is the GW approach.^{28,29,129,130} Within The GW method, the quasiparticle

energies E_{nk}^{QP} are the solutions of the following set of nonlinear equations

$$(T + V_{ne} + V_H - E_{nk}^{QP})\Psi_{nk}(\vec{r}) + \int d^3r' \Sigma(\vec{r}, \vec{r}', E_{nk}^{QP})\Psi_{nk}(\vec{r}') = 0 \quad (38)$$

where T is the kinetic energy operator, V_{ne} the potential of the nuclei, V_H the Hartree potential and Σ is the self-energy operator given by

$$\Sigma(\vec{r}, \vec{r}', \omega) = \frac{i}{4\pi} \int_{-\infty}^{\infty} e^{i\omega'\delta} G(\vec{r}, \vec{r}', \omega + \omega') W(\vec{r}, \vec{r}', \omega') d\omega' \quad (39)$$

where G is the Green's function, and W is the screened Coulomb interaction of the electrons. The GW method includes many-body effects in the electron–electron interaction and goes beyond the mean-field approximation for independent particles. This is achieved via the dynamical screening of the exchange operator with the frequency-dependent dielectric matrix of the system. The GW method is conceptually rather simple, but computationally very demanding. Therefore, realizations of the GW approach often rely on a simplified description of dynamical effects via a plasmon-pole model and/or replacing the quasi-particle eigenfunctions Ψ_{nk}^{QP} by their LDA counterparts. Some time ago a simplified version of the GW using the plasmon pole approximation has been implemented in VASP by Furthmüller et al.¹³¹

Very recently, Shishkin and Kresse have implemented different versions of the GW method in VASP. At the lowest (and hence computationally less demanding) level of sophistication, DFT (GGA) eigenvalues and orbitals are used to calculate the Green's function G and the screened Coulomb interaction W (using the random-phase approximation to the dielectric matrix)—this is commonly called the G_0W_0 approximation.¹³² Updating the eigenvalues in the Green's function G while the screening properties are still treated in the RPA using GGA eigenvalues and orbitals leads the GW_0 approximation, updating the eigenvalues in both the Green's function G and in the screening matrix determining W defines the self-consistent GW method. Shishkin and Kresse¹³² have demonstrated that the G_0W_0 approximation based on LDA or GGA eigenstates underestimates the gaps for practically all materials. This conclusion agrees with the results of G_0W_0 calculations based on the all-electron full-potential linearized muffin-tin-orbital method¹³⁴ and on the FLAPW method,¹³⁵ but contradicts a widespread belief based on pseudopotential calculations - the good agreement achieved in these calculations is due to a cancellation of errors. GW_0 calculations¹³³ yield excellent predictions for the band gaps, except for systems with shallow d-states (e.g. ZnO) where the gaps are still underestimated by up to 10%. It has been demonstrated that this is due to an overestimation of the static dielectric constant in the RPA. Unfortunately the completely self-consistent GW approach yields consistently too large band-gaps (the overestimation is most pronounced for narrow-gap semiconductors) - except for the systems with shallow d-states.

The performance of GW calculations depends not only on the level of self-consistency that is achieved, as the GW method is

a perturbative approach the results depend also on the choice of the exchange-correlation functional chosen as a starting point. A detailed comparison of the results achieved with different methods (LDA, PBE0 and HSE03 hybrid functionals, HF, screened exchange) for the calculation of the one-electron eigenvalues and wavefunctions has been presented by Fuchs et al.¹³⁶ It was found that G_0W_0 corrections applied to Kohn-Sham schemes based on screened exchange (Screened HF, HSE03) yield good overall agreement with experimental band gaps, while the quasiparticle corrections are too small when applied to LDA or GGA eigenstates and too large if added to PBE0 results. For calculations based on the HSE03 functional, self-consistency in G and W impairs the agreement with experiment.

It has been suggested that the problems encountered in the self-consistent GW calculations might be related to the neglect of the attractive Coulomb interaction between electrons and holes, which is also responsible for the excitonic effects observed in the optical spectra,¹³⁴ which can be included in GW calculations via vertex corrections. A self-consistent GW including the effects of the electron hole interaction has very recently implemented in VASP by Shishkin and Kresse.¹³⁹ Following Reining et al.^{137,138} the effects is cast into the form of a nonlocal exchange-correlation kernel $f_{xc}(\vec{r}, \vec{r}')$, with the full polarizability given by a Dyson equation,

$$\chi = [1 - \chi_0(v + f_{xc})]^{-1} \chi_0, \quad (40)$$

where χ_0 is the non-interacting polarizability and v the Coulomb interaction. Within DFT, the exchange-correlation kernel is given by the second variational derivative of the exchange-correlation functional with respect to the density:

$$f_{xc}(\vec{r}, \vec{r}') = \delta(\vec{r} - \vec{r}') \frac{\delta^2 E_{xc}[n(\vec{r})]}{\delta^2 n(\vec{r}) \delta(\vec{r})}. \quad (41)$$

The inclusion of electron-hole interactions successfully corrects the overestimation of the band-gap in the self-consistent GW (see Fig. 9) and also yields very accurate ion-clamped (high-frequency) dielectric constants. An exception are again the systems with shallow d-states such as ZnO, where the screening is still underestimated. Self-consistent GW calculations including vertex corrections are very demanding. Therefore, it is an important result that GW_0 results are consistently in good agreement with the vertex-corrected GW gaps. This offers a convenient access to less demanding but still accurate calculations.

Van-der-Waals bonding

A correct description of van-der-Waals interactions requires a treatment of dynamic long-range correlation effects. In principle, an exact expression for the correlation functional may be derived on the basis of the adiabatic-connection fluctuation-dissipation theorem (AC-FDT).^{140,141} This theorem relates the correlation energy to the electronic response of a system when the electron-electron interaction is continuously changed from the Hartree-Fock limit to the full many-body interaction. The AC-FDT expression for the

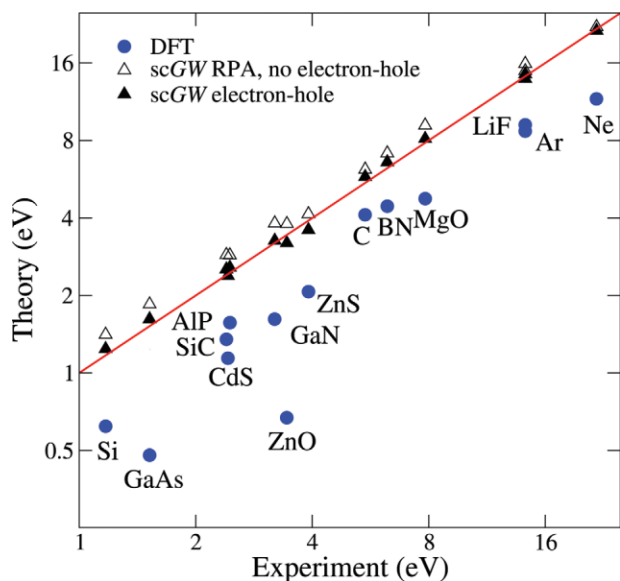


Figure 9. DFT and selfconsistent GW band gaps with and without attractive electron-hole interactions (vertex corrections in W), compared with experiment. After Shishkin and Kresse.¹³⁹ [Color figure can be viewed in the online issue, which is available at www.interscience.wiley.com.]

correlation energy is

$$E_{\text{corr}} = - \int_0^1 d\lambda \int_0^\infty \frac{d\omega}{2\pi} \text{Tr}\{v[\chi^\lambda(i\omega) - \chi^0(i\omega)]\}, \quad (42)$$

where v stands for the Coulomb kernel in Fourier space, $v_{\vec{G},\vec{G}'}(\vec{q})$ and the operator Tr includes taking the trace over the product of the Coulomb kernel with the difference in the response tensors of the interacting and non-interacting systems. The response function of the λ -interacting system is given by the Dyson equation,

$$\chi^\lambda(\vec{q}) = \chi^0(\vec{q}) + \chi^0(\vec{q})[\lambda v(\vec{q}) + f_{\text{xc}}^\lambda(\vec{q}, i\omega)]\chi^\lambda(\vec{q}). \quad (43)$$

The Dyson equation is solved in the random-phase approximation (RPA), i.e. by neglecting the local-field corrections f_{xc} . The total energy of a system is given by the sum of the expectation value of the Hartree-Fock Hamiltonian evaluated with one-electron wave functions from a DFT calculation plus the correlation energy. For a more detailed discussion of the underlying theory see Furche¹⁴¹ or Dahlen et al.¹⁴² Furche has shown that the AC-FDT combined with the RPA leads to accurate atomization energies of diatomic molecules.

The RPA-AC-FDT has very recently been implemented in VASP by Harl and Kresse.¹⁴³ Results of their plane-wave based calculations agree with the atomic-orbital results of Furche within 1 kcal/mol. Calculations of the lattice constants and cohesive energies of rare-gas solids (see Table 3) demonstrate that the approach leads to a dramatic improvement of the calculated cohesive energies.

The LDA leads to a strong overbinding—too small lattice constants and too large cohesive energies—while the PBE results show

a significant underbinding. AC-FDT results have been calculated with both LDA and PBE wave functions, with more accurate results for AC-DFT calculations starting from the PBE level. While differences in the correlation energies are rather modest, the HF energies calculated with PBE wavefunctions are smaller, improving agreement with experiment. This suggests that the PBE wavefunctions are closer to the ground-state HF orbitals. Although plane-wave calculations of correlation energies are rather demanding, these results demonstrate that a treatment of van-der-Waals bonding in extended systems is feasible.

Tools

So far, I have discussed the fundamental quantum-mechanical principles and the numerical strategies implemented in VASP. Beyond the accuracy, efficiency and stability of the basic code, the usefulness of a program package depends on the availability of routines for calculating a wide range of physico-chemical properties and for simulating atomic-scale processes, and also of software packages allowing a visualization of the results—this is what I like to call “tools.” In the following, I give a brief overview of some of the “tools” available with VASP or developed by VASP users.

VASP contains a *symmetry package* returning the Bravais lattice and point group symmetry corresponding to the input coordinates. For spin-polarized calculations in addition the magnetic symmetry group corresponding to the initial magnetic moments is returned. This information is used to construct the \vec{k} -space grid used for Brillouin-zone integrations and to symmetrize total charge- and spin-densities, forces, and stress-tensors of each iteration, unless symmetrization is explicitly suppressed.

Static structure optimization of periodic systems (unit cell parameters and internal coordinates) is performed routinely in VASP via quasi-Newton, conjugate-gradient schemes or using a damped second-order equation-of-motion for the ions, using the analytically calculated Hellmann-Feynman forces acting on the atoms and the stresses on the unit cell. Structure optimization may also be performed at a fixed external pressure. The calculations are performed in terms of Cartesian coordinates. Isolated molecules or clusters may be treated by placing them into computational cells large enough to suppress any interaction with the periodically repeated images. Alternatively (and this might be preferable for complex molecules, molecular crystals, layered crystals, or complex microporous solids)

Table 3. Equilibrium lattice constants a_0 (in Å) and cohesive energies E_c (in meV/atom) for the fcc rare-gas solids, compared with experiment (after Harl and Kresse¹⁴³).

		DFT-LDA	ACFDT-LDA	DFT-PBE	ACFDT-PBE	Expt.
Ne	a_0	3.9	4.7	4.6	4.5	4.35
	E_c	83	11	20	17	27.3
Ar	a_0	4.9	5.4	6.0	5.3	5.23
	E_c	140	59	22	83	88.9
Kr	a_0	5.3	5.8	6.4	5.7	5.61
	E_c	165	88	25	112	122.5

static optimization may be performed in internal (chemical) coordinates using a routine developed by Bucko et al.¹⁴⁴

The calculation of the structural energy differences allows to determine the energetically most favorable structure among a finite number of possible candidate structures, and also to investigate possible pressure-induced *phase-transitions* among these structures (and also temperature-induced phase-transitions if the vibrational contributions to the free energy are derived from phonon-calculations). However, it does not allow to determine unknown crystal structures. This has become possible by the development of *genetic algorithms* such as that developed by Oganov and Glass.^{145,146} Their USPEX package¹⁴⁶ allows to predict the equilibrium structure of a system, using as input the chemical composition and the forces and stresses calculated using a package such as VASP.

Molecular dynamics simulations may be performed in a micro-canonical ensemble, or in a canonical ensemble using Nosé dynamics. Either a Verlet algorithm or a predictor-corrector scheme is used to integrate the Newtonian equations of motion of the ions. Note that during MD runs, the volume and shape of the cell are kept fixed.

Transition-states on potential-energy surfaces (for the diffusion of atoms, phase-transitions, chemical reactions etc.) may be determined using the nudged elastic band (NEB) method.^{147,148} In this approach, a “band” of intermediate states is constructed along an assumed reaction path connecting the initial and final states. These intermediate states are then relaxed in the subspace orthogonal to the reaction coordinate. That the saddle point identified along this path is a real transition state may be verified by calculating the vibrational eigenfrequencies (see below). Calculation of the vibrational eigenmodes for the initial and transition state also allows to calculate reaction rates within the framework of harmonic transition-state theory.^{149,150}

The calculation of the Hessian matrix (i.e. the matrix of the second derivatives of the total energy with respect to the atomic positions) allows to determine the *elastic constants* and the *vibrational eigenmodes* of a system. To calculate the Hessian matrix finite differences are used, i.e. ions are displaced by small amounts from their equilibrium positions in the direction of Cartesian coordinates and the derivative of the reaction forces relative to the displacement is calculated. This may be done either for all three Cartesian coordinates of all atoms, or only symmetry-inequivalent displacements are considered. The former mode of operation may be used to calculate the vibrational eigenmodes of a part of the system, e.g., the vibrational eigenmodes of a molecule adsorbed on a substrate. The calculation of the derivatives with respect to the symmetry-inequivalent displacements allows a very economic calculation of the vibrational eigenmodes of molecules¹⁵¹ and of phonon spectra of solids using the “direct” approach.¹⁵² It must be emphasized that, because the calculations are based on a periodically repeated supercell, the correct splitting of the longitudinal and transverse optical requires corrections for the electrostatic dipole moments of polar phonon modes, using the matrix of the Born effective charges. The direct approach has also been implemented by Parlinski in a program package allowing to calculate phonon spectra for bulk materials with arbitrary symmetry, using the forces calculated by VASP as input.¹⁵³ The PHONON package also offers a graphical user interface. A similar package for phonon calculations is also available from Alfé.¹⁵⁴ The elastic tensor for systems with arbitrary symmetry is calculated from the stress-strain relationship and allowing a relaxation of all

internal coordinates, following the method proposed by LePage and Saxe.¹⁵⁵

The evaluation of the Berry phase expression for the *polarization* of crystalline solids,^{156,157} appropriately generalized to the PAW formalism, has been implemented in VASP by Marsman (unpublished observations). The *frequency-dependent dielectric matrix* may be calculated. The imaginary part is calculated by summation over empty states, the real part by a Kramers-Kronig integration. Density functional perturbation theory^{156,157} has been implemented in VASP by Gajdos et al.¹⁵⁸ This allows to calculate the *static dielectric tensor*, the *piezoelectric tensor*, the *vibrational frequencies*, and the matrix of the *Born effective charges*. The approach avoids a summation over empty bands, instead the derivatives of the periodic part of the eigenstates with respect to the wave vector are calculated using perturbation theory. The calculation may be performed without or including local field effects (as described in the section on GW calculations). For the dielectric and piezoelectric tensors both the ion-clamped and the relaxed-ion version may be calculated.

Note that not all capabilities are included in the version VASP4.6 distributed until March 2008, but require version VASP5.1. Detailed descriptions may be found in the VASP manual which is freely accessible on the web-site.⁵³

Applications

In the following, I want to highlight front-line applications of VASP in many different areas. During 2007 alone, more than 300 papers have appeared in the scientific literature in which VASP has been used for some kind of *ab initio* calculations. It is hence quite impossible to keep track of all interesting applications. The references given below are hence necessarily fragmentary and concentrated on the work of our own group.

Crystal structure and phase stability

Ab initio calculations of the stable crystal structure and of phase transformations under increasing pressure and temperature are of course a very active field. *Ab initio* results are now available for almost all elements of the Periodic Table of the Elements and for a large number on inorganic compounds, with a few applications also to molecular crystals. Out of the many papers on the structures of the elements, I only refer to the work on the polymorphs of Mn^{119,159} and their transformations under applied pressure - Mn is probably the most complex of all metallic elements.

An important contribution of *ab initio* calculations based on VASP was the elucidation of the complex quantum-mechanical effects leading to the formation of novel, very complex structures of many elements under extreme pressures. Under pressure, the polyvalent metals and semimetals and the heavy alkali and alkaline-earth metals transform from simple dense-packed to complex, more open structures describable as (sometimes incommensurate) host-guest structures.¹⁶⁰ For the heavier pnictide elements As, Sb, and Bi, Häussermann et al.¹⁶¹ have presented detailed *ab initio* calculations of the phase transformations and discussed the dominant influence of pressure induced changes in the electronic structure. Even more surprising were the theoretical predictions that under very high compression the atomic and electronic structures of Li¹⁶² and Na¹⁶³ depart significantly from the expected simple-metal behavior,

showing low structural symmetry and semimetallic electronic properties. For Li, the structural sequence under pressure is predicted to culminate in a nearly insulating ground state with paired atoms and under extreme compression Na is also predicted to adopt a paired structure and to become a zero-gap semiconductor. It has been shown that the changes in the atomic and electronic structures result from the combined effects of Pauli exclusion and core-valence orthogonality: the valence electron density is minimal near and between the ions and maximal in the interstitial regions, lowering kinetic and exchange energies. Evidently the all-electron character of the PAW approach implemented in VASP and the ability to relax the 1s (Li) and 2s2p (Na) states is very important for such calculations. Very recent work has extended these exploratory studies to dense intermetallic compounds of Li and Be.¹⁶⁴ These metals are immiscible under ambient conditions but form stable intermetallic compounds under increased pressure, with complex crystal structures and a striking deviation from free-electron like behavior. Exploratory studies of the high-pressure structures of the elements based on VASP combined with genetic algorithms have been performed by Oganov and Glass for carbon, sulphur, oxygen, nitrogen and hydrogen. Vočadlo et al.¹⁶⁵ have used VASP to explore the nature of the stable phase of iron in the Earth's inner core, which is still highly controversial.

VASP has been used extensively to explore the crystal structure of intermetallic compounds. Studies include aluminides,^{166–168} silicides,^{169–171} Laves phases (including an investigation of temperature-induced phase transitions between different stacking variants),^{172–174} Zintl phases,^{175–177} Heusler alloys,^{178,179} Nowotny “chimney-ladder” phases,¹⁸⁰ shape-memory alloys,^{181,182} and crystalline approximants to quasicrystalline alloys.¹⁸³ The *ab initio* calculations provide a detailed picture of the chemical bonding in these complex phases and a clear understanding of the correlation between the electronic and magnetic properties and the crystal structures. As an example Figure 10 shows the complex crystal structure of the compound Al_{10}V . The structure consists of a Kagomé lattice composed of intersecting, covalently bonded $\cdots - \text{Al} - \text{V} - \text{Al} - \text{V} - \cdots$ chains in whose cavities large Friauf polyhedra of Al atoms are embedded. This structure is prototypic for the crystalline constituents of high-strength nanocrystalline Al-based alloys.¹⁸⁴ Calculations for approximants to icosahedral and decagonal quasicrystals have been extended to unit cells with more than five hundred atoms.¹⁸³

Work on disordered alloys can be based either on a supercell approach¹⁸⁵ or combine *ab initio* DFT calculations with multi-scale simulations techniques such as the cluster-expansion (CE) approach.^{186,187} Here DFT calculations are used to describe the range, type (pairs, triplets, . . .) and chemical character of the interaction energies. On the basis of this information, CE opens the possibility to quantitatively investigate temperature-dependent alloy properties such as short-range order effects, mixing enthalpies or the formation of microstructures.

An important application of the ability of VASP to provide accurate structural and energetic information on multicomponent systems (even if their crystal structures are incompletely specified or unknown) is the use of these data in computational thermodynamics approaches^{188,189} predicting complex, multicomponent phase equilibria such as they are important in many industrial alloys. Reliable information from *ab initio* calculations has contributed to boost

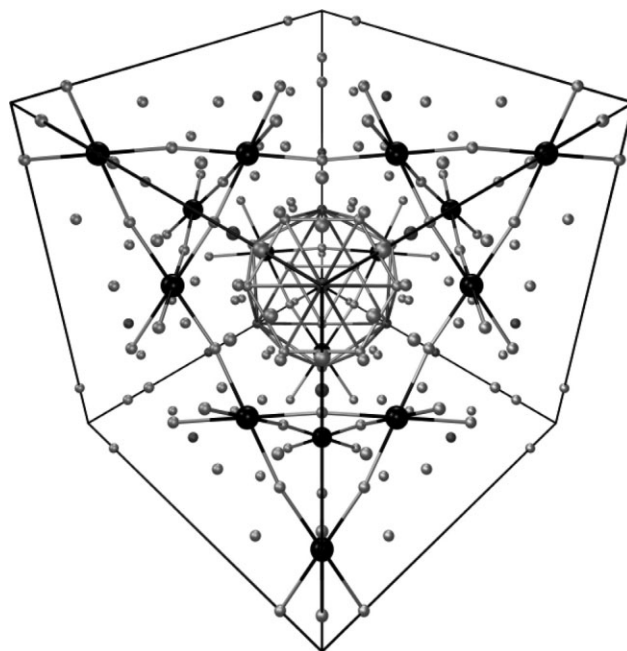


Figure 10. Optimized crystal structure of the intermetallic compound Al_{10}V . The structure consists of a Kagomé lattice of vanadium atoms with Al atoms in the center of each V-V bond. In the large interstices of the Kagomé lattice, large Friauf polyhedra of Al atoms are located. A unit cell contains 176 atoms. After Jahnatek et al.¹⁶⁸

the predictive capabilities of these approaches - for an example see, e.g., the work of Wolverton et al.¹⁹⁰ on metastable phases in age-hardening aluminum alloys.

Applications of VASP to the structures of inorganic compounds include oxides,^{79,99–101,125,126,191–193} sulphides,^{124,194,195} hydrides,^{196–199} carbides and related ternary compounds,^{200,201} ceramics,^{202,203} and clathrates.^{204,205} The importance to include corrections for strong electronic correlation effects has been evidenced not only for many transition-metal oxides,^{99–101,125,126,206} pronounced magneto-structural effects, and an important role of electronic correlations has also been demonstrated for certain transition-metal sulphides.^{114,124} The studies on the mixed Li_xCoO_2 oxides¹⁹² are motivated by the use of these materials as cathode materials in Li batteries. The work on hydrides is of particularly timely interest in connection with the search for novel hydrogen storage materials.

Ab initio calculations using VASP have also been applied to many minerals. One of the first studies in this field was the very comprehensive investigation of polymorphism in silica.²⁰⁷ The changes in the crystal structures near the continuous $\alpha \rightarrow \beta$ transitions in quartz and cristobalite and at the discontinuous pressure-induced phase transitions from quartz to coesite and from coesite to stishovite have been explored in detail. The work also illustrates the limitations of local and semilocal DFT functionals: while for a correct prediction of the transition pressures, the GGA is largely superior to the LDA, the GGA predictions for the energy differences between quartz and some low-density polymorphs (tridymite, keatite) are questionable. A re-investigation using hybrid functionals has been started. The work has also been

extended to high-pressure post-stishovite phases.²⁰⁸ The work on the polymorphs of silica is closely related to studies of aluminosilicates, including zeolites,^{209–211} silicoaluminophosphates (SAPO's),^{212,213} and clays,^{214–216} demonstrating the ability of VASP to accurately describe the structures and physico-chemical properties of these complex systems. The work on clays already highlights the impact of VASP in the geosciences where the code has contributed to the solution of long-standing problems (we have already referred above to the work on the crystalline phases of Fe under extremal pressures and temperatures). Of particular interest was the work of Oganov and Ono²¹⁷ on the structure and the physical properties of the “post-perovskite” phase assumed by MgSiO₃ under the conditions prevalent in the Earth's lower mantle which lead to a re-interpretation of puzzling aspects in the seismic data. A review of applications of DFT in the geosciences (many of them based on VASP) was recently given by Brodholt and Vočadlo.²¹⁸

Applications of VASP to molecular crystals are still rather scarce. The potential of the code in this field is, however, very nicely illustrated by the work of Plazanet et al.^{219,220} on crystalline DNA bases (thymine, guanine, . . .) demonstrating that the structures optimized at the GGA level provide an excellent basis for a highly accurate calculation of the vibrational spectra of these hydrogen-bonded systems. In fact it seems that the proton-positions derived from the calculations are more accurate than the available experimental data.

VASP has also been applied successfully to the structural optimization of complex molecular systems. Examples are dye molecules adsorbed on solid surfaces²²¹ or the structure of the molecular complexes formed by rhodopsin chromophore and various counterions.²²²

Mechanical properties: Elasticity, theoretical strength, fracture

Ab initio DFT calculations based on VASP have a great potential for the calculation of mechanical properties of solids (elastic constants, theoretical strength under tensile and shear loading, plastic deformation, fracture). Calculations of the full elastic tensor of materials are now quite standard, for illustrative results for metals and intermetallic compounds see, e.g., ref. 167, 223, for calculations of the variation of the elastic constants of minerals over a wide range of pressures, see refs. 145, 224, 225. A more recent application of first-principles calculations is the investigation of the response of metals and intermetallic compounds to tensile and shear loading, including the determination of the theoretical strength and the elucidation of the mechanism of structural transformations under applied non-hydrostatic strains. As exemplary applications of VASP I would like to mention the work of Ogata and Yip²²⁶ of the shear strength of face-centered cubic Al and Cu,²²⁶ the work of Morris et al. on the ideal strength of iron, molybdenum and tungsten under tension and shear.^{227,228} The investigations have been extended to B2-type transition-metal aluminum compounds (FeAl, CoAl, NiAl)²²⁹ and to L1₂ and D0₂₂-type trialuminides of Sc, Ti and V,²³⁰ Ogata et al. have presented calculations of the ideal shear strength for a series of simple metals and ceramics.²³¹

The potential of the *ab initio* calculations is illustrated in Figure 11, which shows the response of D0₂₂-type Al₃Ti to uniaxial tensile loading along the [110] direction. The scenario is quite remarkable: (i) The deformation under uniaxial tension does not occur along the tetragonal Bain path, but along an orthorhombic deformation path.

(ii) Immediately after passing the saddle point along the orthorhombic deformation path, a bifurcation to a tetragonal deformation path occurs. This bifurcation occurs at the “special invariant state” (labeled D) with $C_{22} = C_{33}$ which admits a bifurcation under dead load. (iii) The tetragonal deformation leads to a “flipped” D0₂₂ phase with the same decoration of the tetragonal unit as in the initial state A. This scenario is very similar to that proposed for the fcc metals by Milstein et al.²³² where under very large strains the fcc structure is restored by a “flip-strain” mechanism. It is interesting to note that for the trialuminides the same mechanism operates for the tetragonal D0₂₂-phases, but not for the cubic L1₂-phase—the differences in the response to tensile deformation have been analyzed in terms of the metallo-covalent bonding properties of these phases.²³⁰

The correlation between elasticity and cleavage has been studied by Lazar and Podloucky,²³³ the formation of grain boundaries and their influence on the tensile strength has been studied for Al²³⁴ and Fe.²³⁵ VASP has also been used to investigate segregation at grain boundaries,²³⁶ as well as segregation-induced embrittlement^{236,237} and deformation twinning.²³⁸

Dynamical properties: Collective and single-particle dynamics

The calculation of the phonon spectrum and of the vibrational contributions to the free energy is one of the most popular applications of VASP. The first applications within our group dealt with diamond and graphite,¹⁵² hexagonal and cubic BN²³⁹ and fcc Rh.²⁴¹ These calculations demonstrated that DFT-derived phonon frequencies achieve in general agreement with experiment within a few percent. However, the investigations of the transition metal Rh also signaled a caveat: because of the long-range nature of the interatomic forces in metals, convergence with respect to supercell size cannot be achieved with a single large and isotropic supercell. A converged solution could be achieved by deriving independent sets of interplanar force constant from calculations with long $1 \times 1 \times n$ supercells (with n up to 13) stretching along the main crystallographic directions. This information may be used to fit a matrix of long-range Born-van Karman force constants. The reward for this extra effort is that even details of the dispersion relations such as Kohn anomalies associated with nesting vectors of the Fermi surface are described with good accuracy.²⁴¹ Not all subsequent applications to metals took this lesson into account.

The calculations for the BN polymorphs were extended to a calculation of the phonon Grüneisen parameters which opens the way to a calculation of the vibrational free energies in a quasi-harmonic approximation and of the temperature-induced phase transition from layered hexagonal to cubic BN.²³⁹ The investigations on carbon-based systems have been extended to graphene layers and nanotubes.²⁴⁰

Very recently much effort has been spent on *ab initio* calculations of the thermodynamic properties of the metallic elements, based on phonon spectra calculated via the “direct” method.¹⁵² Grabowski et al.²⁴² have presented an extended study for nonmagnetic fcc metals (Al, Pb, Cu, Ag, Au, Rh, Ir, Pd, Pt), including an investigation of the influence of the exchange-correlation functional, the supercell size and the k-space grid used for the calculation of the electronic total energy and of the phonon density of states. It was demonstrated that, if cubic supercells are used, full convergence is reached for Pb (the worst case) only for $5 \times 5 \times 5$ cells containing 500 atoms and that

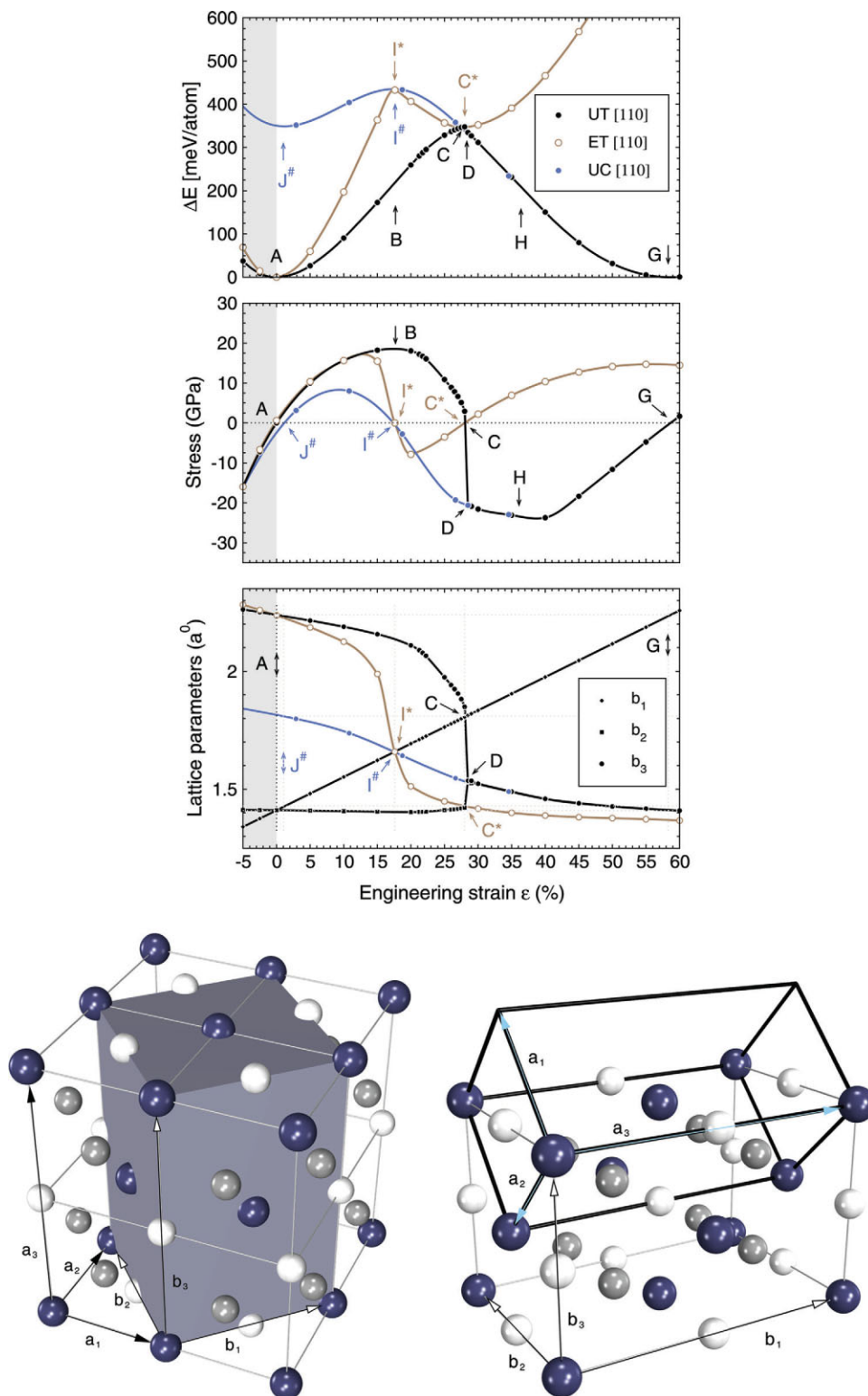


Figure 11. Top: Response of $D0_{22}$ -type Al_3Ti to [110] uniaxial loading: Energy-strain (top), stress-strain (middle panel), and the strain dependence of the lattice parameters (bottom) are shown for unconstrained relaxation under tension (UT) and compression (UC) and along the epitaxial Bain path (ET). Bottom: Starting configuration (left) and flipped $D0_{22}$ structure (right). Al atoms are shown in white and light gray, Ti atoms in black. Cf. text. After Jahnatek et al.²³⁰ [Color figure can be viewed in the online issue, which is available at www.interscience.wiley.com.]

for transition metals $4 \times 4 \times 4$ supercells with 256 atoms are required to exclude safely all imaginary modes and to correctly reproduce the experimentally observed Kohn anomalies, confirming the earlier conclusions made at the example of the Rh calculations.²⁴¹ An interesting observation is that the choice of the exchange–correlation functional (LDA or GGA) influences the result mainly through the determination of the equilibrium volume. If the calculations are based on the theoretical $T=0\text{K}$ lattice constants, LDA yields too hard bulk moduli and phonon frequencies, while the GGA produces too soft bulk moduli and vibrational eigenmodes. Thermal expansion coefficients and heat capacities are larger in the GGA (for the heavy elements the agreement with experiment is better in the LDA). If the $T=0\text{K}$ calculations are performed at the experimental lattice constant, the situation is reversed, GGA frequencies are now softer, the influence of the functional on the thermodynamic properties is strongly reduced. This suggests that calculations using functionals such as PBEsol or AM05 giving better lattice constants and bulk moduli than the conventional GGA (see Table 1) should also lead to an improved prediction of phonon frequencies and thermodynamic properties.

Similar studies including also bcc (Nb, Mo) and hcp (Ti, Y, Zr, Ru, Tc, Ru) transition-metals have been performed by Souvatzis et al.^{243,244} These calculations are based on much smaller supercells (27 atoms for the hcp, 64 atoms for the bcc metals). Although for the fcc metals the results are in semiquantitative agreement with those of Grabowski et al.,²⁴² the difference between the LDA and GGA predictions is even larger, with a still more pronounced preference for the LDA (as the authors point out, this is at least partially due to a cancellation of errors). A remarkable result for the hcp metals is that the strong anisotropy of the thermal expansion and in particular the negative values for the thermal expansion along the hexagonal lattice observed for Ti at low temperatures is correctly reproduced and assigned to a van-Hove singularity in the electronic density of states.²⁴³

Calculations of phonon dispersion relations and thermodynamic properties have also been extended to intermetallic compounds. As an example Figure 12 shows the dispersion relations calculated for DO_3 -type Fe_3Si , compared with the inelastic neutron scattering results.¹⁷¹ The experimental investigations for this compound have been motivated by the unusually fast diffusion of Fe atoms, which had been tentatively attributed to soft lattice modes. The figure demonstrates good agreement between theory and experiment for all 12 dispersion branches and that the fast diffusion must be attributed to another mechanism (see also below).

Extensive calculations of phonon spectra, thermodynamic properties and temperature-induced phase transitions have been performed for Laves phases, including also an investigation of the influence of magnetic ordering on the vibrational properties.^{173,245} For ZrMn_2 , better agreement with the phonon densities of state measured at low temperature has been observed for the ferromagnetic state.²⁴⁵

Only a few investigations of lattice vibrations in non-metallic compounds can be mentioned here. *Ab initio* phonon calculations for insulators are less demanding in the sense that due to the short-range interactions, a smaller supercell is often sufficient. On the other hand in heteropolar insulators cations and anions carry effective charges (the Born effective charges) and due to the periodic boundary conditions polar phonons create an electrostatic

field suppressing the LO-TO splitting. To correct the effect of this artificial field created by the boundary conditions requires the knowledge of the matrix of the Born effective charges. Calculations of pressure-induced phase transitions and of the phonon dispersion relations have been performed for various polymorphs of GeO_2 , with the aim of characterizing the order of the structural phase transitions.²⁴⁶ Studies of phonons in Fe-borate²⁴⁷ have elucidated the influence of magnetic ordering on the lattice vibrations. Calculations for a MgAl_2O_4 spinel display the ability to accurately predict the acoustic and optic modes of an insulator with a complex crystal structure with 56 atoms in the cubic unit cell.²⁴⁸ The acoustic modes are in good agreement with the inelastic neutron scattering data, the optic modes at the Γ -point compare very well with the five Raman and four infrared active modes. Calculations of phonon dispersion relations and of vibrational free energies for different polymorphs of ceramic materials have recently been presented by Tanaka and Oba.²⁰³ In combination with cluster expansion techniques and Monte Carlo simulations, the first principles calculations have been extended to evaluate the temperature-dependence of cationic disorder in AB_2O_4 spinels, where A and B are divalent and trivalent cations, respectively.

Computational studies of single-particle dynamics are difficult. Diffusive jumps of atoms or vacancies are rare events on the time-scale of *ab initio* molecular dynamics simulations, but activation energies for diffusion may be determined by via nudged-elastic band calculations. This approach has been used to study the fast vacancy-promoted diffusion of Fe-atoms in Fe-silicides¹⁷¹ and the diffusion of charged and neutral vacancies in Y-doped zirconia.²⁴⁹ A similar approach has also been used to determine activation energies for hopping- and exchange-diffusion on metallic surfaces.^{250–252}

Liquids and amorphous materials

The intention to perform *ab initio* molecular dynamics (MD) simulations for molten transition metals was one of the motivations for the development of the first versions of VASP based on ultra-soft pseudo-potentials - the structures of molten Cu and V belonged to the early applications of the code.²⁵³ This was followed rather soon by *ab initio* MD simulations of liquid Ge and of the formation of an amorphous phase by ultrafast quenching²⁵⁴—this simulation demonstrated that *ab initio* MD simulations could be extended over time-scales long enough to produce realistic amorphous structures by a simulated quench. The interest in the liquid-metal to amorphous-semiconductor transition has recently been renewed by reports²⁵⁵ that the transition is preceded by a liquid-liquid phase transition from a high-density liquid with imperfect to a low-density liquid with almost perfect tetrahedral coordination. *Ab initio* simulations based on VASP have been used by Jakse and Pasturel²⁵⁶ to confirm the existence of such a transition and to characterize the structural and electronic properties of the two undercooled liquid phases of silicon.

A number of investigations were devoted to molten metals under extremal conditions: The structure and electronic properties of mercury were studied along the liquid-vapor coexistence line, from the triple-point up to the liquid-gas critical point.²⁵⁷ The liquid structure was found in excellent agreement with experiment all the way up to the critical point and it was demonstrated that the metal/nonmetal

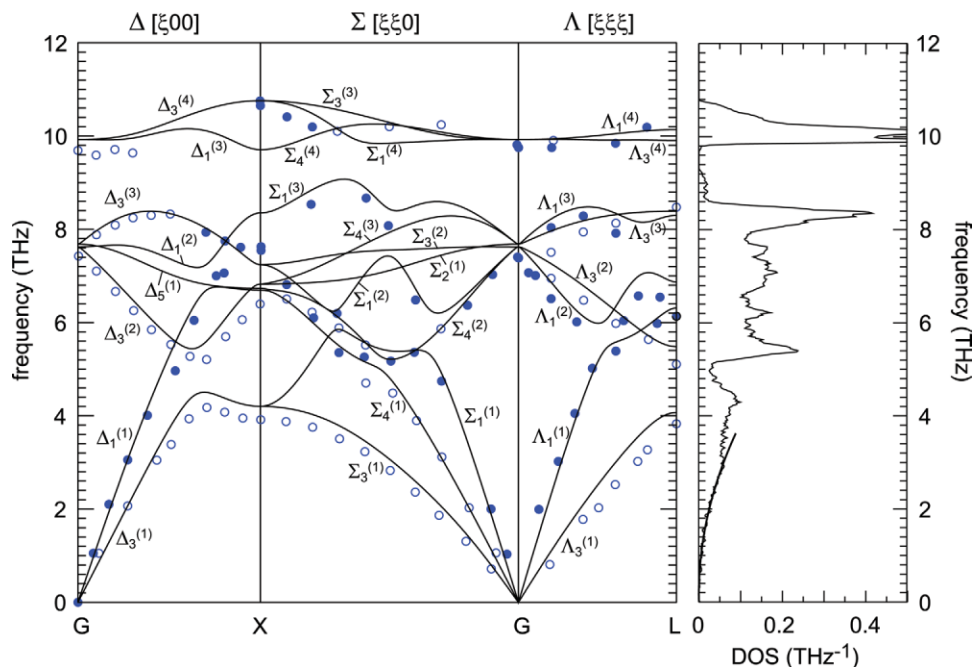


Figure 12. Phonon dispersion relations in DO_3 -type Fe_3Si . Full lines, *ab initio* calculations; dots, inelastic neutron scattering experiments. After Dennler and Hafner.¹⁷¹ [Color figure can be viewed in the online issue, which is available at www.interscience.wiley.com.]

transition taking place before reaching criticality is a simple band-crossing transition, a gap develops between the s- and p-bands (but no localization at the band edges is found). Molten Fe was studied at temperatures and pressures corresponding to the conditions in the Earth's molten core.^{258,259} The viscosity of liquid Fe under these conditions was derived via a Kubo-Greenwood relation from the calculated stress autocorrelation function, with robust values ranging between 15 to 8 mPa.s, going from the inner-core boundary to the core-mantle boundary. This information is important for simulations of the magneto-hydrodynamics of the core, but had been very controversial, with estimates spanning many orders of magnitude.²⁶⁰

Extended *ab initio* MD simulations have been performed for molten Zintl-alloys combining alkali metals with group-IV,^{261,262} group-V,²⁶⁴ and group-VI²⁶³ elements. According to the Zintl-principle the structures of the binaries are characterized by electron transfer from the alkali metal to the polyvalent element and the formation of polyanionic substructures characteristic for the elements in the next column to the right in the Periodic Table, e.g. tetrahedral Sn_4^{4-} clusters isostructural and isoelectronic to P_4 molecules, infinite spiral chains of Sb^- anions isostructural to the chains in trigonal Se, and Te_2^{2-} dimers isoelectronic to halide molecules. Extended diffraction experiments²⁶⁵ have demonstrated the existence of a pronounced chemical and topological short-range order in the molten alloys, which has been interpreted as a sign for the survival of the polyanionic units in the molten phase.²⁶⁵ *Ab initio* MD simulations of these short-range order phenomena are hampered by the fact that if the calculation is initiated by melting the crystalline phase the polyanionic units might survive for a long time, while if the simulations are started from a random configuration the equilibration of a

chemically ordered state is controlled by slow diffusive processes. In any case, simulations for sufficiently large ensembles and long time-intervals are required. The *ab initio* MD simulations on the molten Zintl alloys have been performed in the canonical ensemble, they were based on cells containing up to 125 atoms and covered intervals of up to 60 ps. In this context it is important to point out that as the system is relaxed to the electronic ground-state after each ionic move, the time-increment is controlled by the ionic dynamics alone and may be as large as 2 to 3 fs. This is in contrast to a Car-Parrinello MD using a pseudo-Newtonian dynamics for the electronic degrees of freedom which allows only much shorter time increments (depending on the fictive mass chosen for the electronic eigenstates).

Figure 13 shows a snap-shot of an instantaneous atomic configurations and valence-electron density distributions for molten KSn. The graphs demonstrate that polyanionic clusters survive in the melt and that they are stabilized by covalent multicenter bonds. However, not all these polyanionic clusters display the perfect tetrahedral geometry of the crystalline phase. But comparisons with the available neutron diffraction data demonstrate that the degree of local order is sufficient to reproduce the experimental structure factors.

Recent applications of *ab initio* MD based on VASP have concentrated on the investigation of short-range order in liquid transition metals (Ni,Zr)^{266,267} and molten alloys^{268,269} with the aim of elucidating the ability to form glassy or quasicrystalline alloys. Simulations of quench-condensation of metallic glasses were presented by Sheng et al.²⁷⁰ and Ganesh and Widom.²⁷¹ The work of Sheng et al. illustrates the state-of-the-art for this class of *ab initio* simulations: the work is performed in a canonical ensemble of 100-300 atoms, allowing about 10 ps for equilibration at high

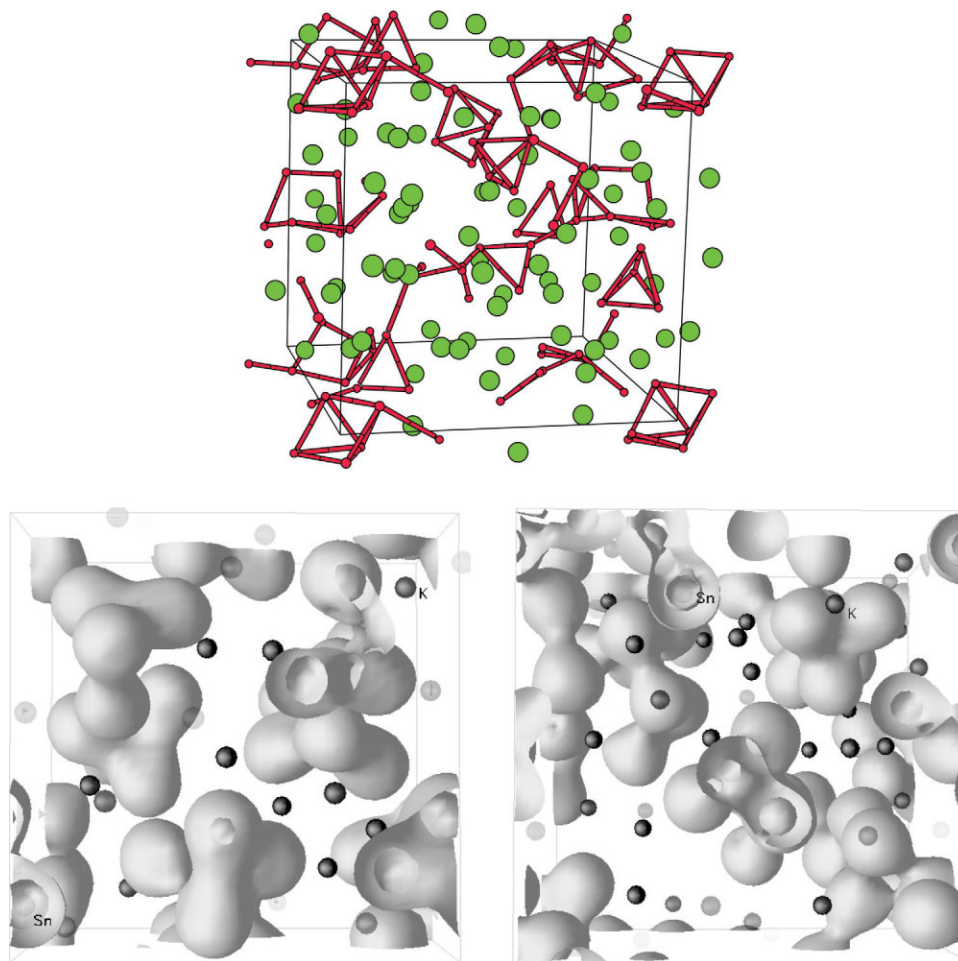


Figure 13. Top: Ball-and-spoke model of an instantaneous configuration in a molten KSn alloy. All Sn-Sn bonds shorter than 3 Å are shown by the red spokes, K atoms in green. Bottom: Constant electron-density contours for two different configurations of molten KSn containing 64 and 96 atoms, respectively. The electron-density contours demonstrate the existence of imperfect tetrahedral Sn clusters stabilized by covalent multicenter bonds. After Genser and Hafner.²⁶¹ [Color figure can be viewed in the online issue, which is available at www.interscience.wiley.com.]

temperatures and quench-rates of 20 to 200 K per 1000 time-steps (of 5 fs) to produce the glassy phase. This allows to achieve excellent agreement of the partial radial distribution functions for Ni-B and Ni-Nb glasses with experiment.²⁷⁰ Liquids and glasses have been probed for icosahedral short-range order using Voronoi tessellation^{270,271} and common-neighbor analysis^{266–269,271} and it was concluded that while the glass-forming ability of bimetallic systems is correlated to a high degree of icosahedral ordering in the melt, no such correlations exists for the amorphous Fe- and Ni-borides where the local arrangements are strongly influenced by the covalent Fe(Ni)-d-B-p bonds. These *ab initio* simulations also support earlier large-scale simulations of transition-metal-metalloid glasses based on tight-binding-bond potentials.²⁷²

An interesting point raised by both Ganesh and Widom²⁷¹ and by Jakse and Pasturel²⁷³ is the persistence of magnetic moments in the liquid phase. Ganesh and Widom point out that spin-polarized

calculations yield better agreement with the measured structure factor of liquid Fe than nonmagnetic calculations. This is attributed to a magneto-volume effect due to local paramagnetic moments. Jakse and Pasturel report large magnetic moments on most Mn atoms in dilute (20 at. pct or less Mn, i.e. at compositions favoring the formation of quasicrystalline alloys) molten Al-Mn alloys. The formation of local moments is interpreted in an impurity model. Increasing temperature and thermal expansion enforces the impurity character of the Mn atoms and favor increased magnetic moments, as observed experimentally. However, the spin-polarized simulations of melts have not yet exploited the possibility to simulate a non-collinear arrangement of the spin-moments.

As an example of *ab initio* MD simulations of ionic liquids I refer to the recent work on molten AlCl_3 ²⁷⁴ which presents a detailed investigation of the dynamical formation and destruction of $(\text{AlCl}_3)_n$ clusters.

Magnetism and magnetic nanostructures

The potential of VASP for *ab initio* simulations of magnetic materials resides on the ability to simultaneously relax the structural, electronic, and magnetic degrees of freedom as illustrated by the elucidation of the complex magneto-structural effects in Mn (where noncollinear magnetism is correlated to a tetragonal distortion of the complex cubic crystal structure¹¹⁹), in γ -Fe (where distortions of the fcc crystal structure and the spin-spiral magnetism are strongly correlated¹¹⁶), and in transition-metal oxides and sulphides where in addition a correct description of strong electronic correlation effects, either at the level of a GGA+U description¹²⁴ or using hybrid functionals^{100,101} is required.

In this section, I shall briefly review applications of VASP to the description of unexpected magnetic ordering in s-p bonded systems, to strongly correlated transition-metal oxides, to magnetic nanostructures and to novel complex magnetic materials such as magnetic semiconductors and multiferroics. Experimental observations that defects in the atomic network of all-carbon systems such as graphite or polymerized fullerenes lead to itinerant ferromagnetism without *d*-electrons have stirred much interest, because of the promise of light-weight nonmetallic magnets in many applications. Lehtinen et al.²⁷⁵ have used VASP to study the magnetic properties of defects formed in graphite by irradiation—vacancies and vacancy-hydrogen complexes. It was shown that both types of defects carry a magnetic moment, but due to the high mobility of carbon interstitials they will very likely annihilate with interstitials. Vacancy-hydrogen complexes are less reactive and carry a magnetic moment large enough to give a macroscopic signal in agreement with experiment.

While the structural and magnetic properties of many transition-metal oxides with strong electronic correlations such as NiO are well described with DFT+U,^{125,126} the approach is evidently unable to account for systems with a more complex correlation between structure and magnetism. An example are the Mn-oxides in which Mn assumes different oxidation states varying between +2 and +4. The recent work of Franchini et al.^{100,101} includes a critical confrontation of results achieved with a GGA+U approach and using hybrid (PBE0 and HSE03) functionals. Important differences are found for the equilibrium volumes (where PBE+U calculations suffer from a strong overestimation, while PBE0 and HSE03 results are in excellent agreement with experiment), for the band-gap and the magnetic ground state. For all realistic values of *U*, PBE+U gaps are lower than PBE0 or HSE03 gaps. For antiferromagnetic MnO the gap increases from a PBE value of 0.9 eV to only 2.1 eV with PBE+U and even a large value of *U* = 6 eV, while the PBE0 gap of 3.8 eV is in perfect agreement with experiment. Mn₃O₄ and α -Mn₂O₃ are predicted to be metallic in PBE, half-metallic ferrimagnetic and ferromagnetic in PBE+U, while PBE0 and HSE03 predict insulating behavior. β -MnO₂ is metallic in PBE and PBE+U and semiconducting in PBE0 and HSE03. Absolute values of magnetic moments also show best agreement with experiment if a hybrid functional is used in the calculations.

Ultrathin magnetic films have been a very active field of research. Fe-films grown on a Cu(100) substrate have perhaps received more attention than any other thin-film systems, because they illustrate the complexity of magneto-structural effects: Up to about 11 monolayers (MLs), the structure of the films continues the fcc lattice of the substrate, albeit with tetragonal distortions depending on the

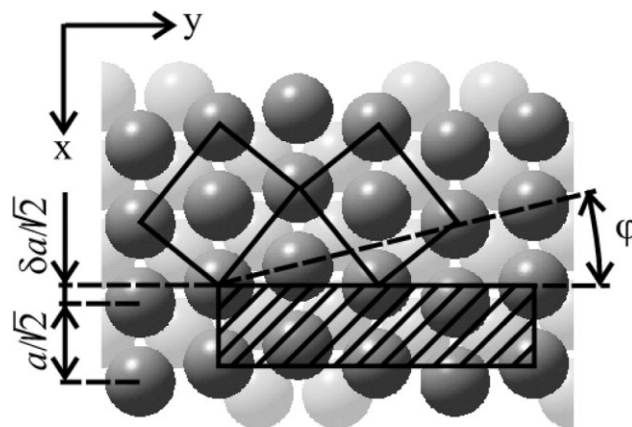


Figure 14. Atomic structure in the two topmost layers of the striped (1×4) reconstruction of a 3 ML Fe/Cu(100) film. The shearing angle is $\phi = 13^\circ$ (theory) against 14° from the STM experiment. After Spišák and Hafner.²⁷⁹

magnetic order in the film. Up to 3–4 ML the film is ferromagnetic, between 4 and 11 ML layered antiferromagnetism develops below a ferromagnetically coupled bilayer at the free surface.²⁷⁶ In addition, LEED experiments²⁷⁷ and STM studies²⁷⁸ have demonstrated that the surface of the films undergoes a ($1 \times n$) reconstruction ($n = 4 - 6$ in the ferromagnetic regime, $n = 2$ in the antiferromagnetic thickness region) leading to the formation of a stripe pattern. *Ab initio* calculations²⁷⁹ have shown that the reconstruction of the films is related to a fundamental instability of *all* magnetic phases of face-centered tetragonal Fe along the Bain-path against monoclinic distortions. In the γ -Fe films the distortion occurs at the free surface, but is limited in the deeper layers because of the epitaxial relationship at the Fe/Cu interface. Figure 14 shows the (1×4) striped phase for a 3ML film. The shearing angle of $\phi = 13^\circ$ is in perfect agreement with the STM results, the vertical corrugation agrees very well with the STM results.

A surprising prediction, based on *ab initio* calculations and later confirmed by experiment, was that in Fe monolayers grown on W(100) surfaces the hybridization of the 3d-states of the adlayer with the 5d-band of the substrate induces antiferromagnetic ordering in the Fe-layer²⁸⁰ while Mn mono- and bilayers grown on the same substrate order ferromagnetically.²⁸¹ In ultrathin Mn films grown on Fe(100) substrates, the competition between ferromagnetic coupling across the interface and antiferromagnetic coupling in the film induces the formation of a noncollinear magnetic spin-flop structure in the film where the antiferromagnetic moments in the film are approximately perpendicular to the spins in the ferromagnetic substrate (see Fig. 15) whose existence has been experimentally confirmed.²⁸²

Investigations of magnetic nanostructures have been extended to stripes²⁸³ and nanowires²⁸⁴ grown at the step-edges of vicinal surfaces, and to clusters in the gas-phase²⁸⁵ and supported on nonmagnetic substrates.²⁸⁶ *Ab initio* simulations reveal interesting aspects of the physics of these systems: for the nanowires a tendency to be buried below the step-edge of the substrates and a long-range interwire-coupling mediated by the substrate,²⁸⁴ for the gas phase clusters the coexistence of structural and magnetic isomers and a

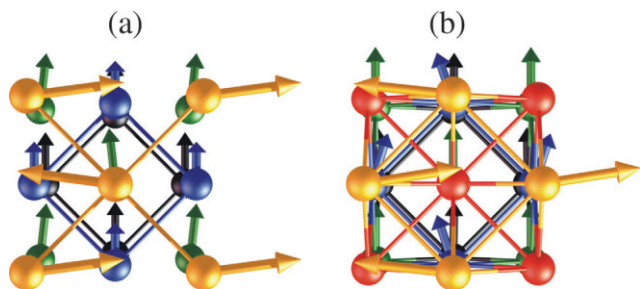


Figure 15. Noncollinear spin-flop structure in Mn mono- and bilayers grown on Fe(100) surfaces. Mn atoms are picture yellow and red, Fe atoms dark blue and green. After Spišák and Hafner.²⁸² [Color figure can be viewed in the online issue, which is available at www.interscience.wiley.com.]

tendency to disfavor icosahedral motifs relative to fragments of crystalline structures²⁸⁵ have been established. Adatoms and clusters supported on highly polarizable substrates such Pd, Rh or Pt induce a long-range magnetic polarization with a strong orbital component, such that the substrate makes a strong, eventually even dominant contribution to the magnetic anisotropy energies.²⁸⁶

The GGA+U approach implemented in VASP,¹²⁴ eventually coupled with a selfconsistent treatment of spin-orbit coupling⁵⁵ has found widespread application. Recent studies treat ferromagnetism in Mn-doped GaAs,²⁸⁷ magnetic doping of cuprous oxide or copper nitride,^{288, 289} orbital ordering and Jahn-Teller distortions in perovskite-type Sr-ruthenate,²⁹⁰ and multiferroics.^{291–293} The work on the magnetic doping of GaAs exploits the high computational efficiency of the approach which allows to achieve realistic dopant concentrations by using large supercells. The investigation of ferroelectricity in the spin-spiral magnets LiCu_2O_2 and LiCuVO_4 ²⁹¹ and in the orthorhombic perovskite HoMnO_3 ²⁹² use also the capability to treat noncollinear magnetic structures and the Berry-phase approach to polarization. For simpler systems, however, the GGA+U approach begins to be superceded by calculations using hybrid functionals,^{99–101} which are, however, computationally much more demanding.

Interesting applications of VASP to molecular magnetism are the recent studies of Fe-phthalocyanine in the molecular phase and adsorbed on Au(111) surfaces²⁹⁴ and of a single-molecule Mn_{12} magnet ($\text{Mn}_{12}\text{O}_{12}(\text{CH}_3\text{COO})_{16}(\text{H}_2\text{O})_4$) attached to a Au(111) surface through thiol groups.²⁹⁵ The simulations of adsorbed Fe-phthalocyanine allow to determine the stable adsorption configuration which greatly influences measured scanning tunneling spectra and the molecular Kondo effect. For the adsorbed Mn_{12} magnet the calculations predict a slight increase of the magnetic moment from $18\mu_B$ to $20\mu_B$ induced by charge transfer from the substrate and a significant increase of the transverse magnetic anisotropy compared to the isolated Mn_{12} molecular magnet.

Semiconductors and insulators

For semiconductors and insulators studies using the version of VASP based on GGA functionals have been performed on semiconductors alloys,²⁹⁶ the structure and mobility of point defects in Si,^{297, 298} in SiGe alloys,²⁹⁹ in SiC,³⁰⁰ in high-k dielectrics,^{301, 302} and in Si

nanocrystallites.³⁰³ Perhaps the studies of impurity diffusion and of nanocrystallites illustrate best the potential of VASP. For B in Si the *ab initio* calculations have been used to determine the optimal geometry and charge-state of the B interstitial and either nudged elastic band calculations have been used to determine migration barriers for different diffusion mechanisms²⁹⁷ or *ab initio* MD simulations at high temperatures have been performed to monitor diffusion events. Both simulations agree on a diffusion mechanism involving a boron-silicon interstitial pair and a migration barrier of about 0.7 eV, in excellent agreement with experiment.

The recent work on doping of Si nanocrystals³⁰³ with atoms from groups III to V is based on varying crystallites sizes (up to 300 Si atoms plus H atoms saturating dangling bonds at the surface) and shapes, spin-polarized calculations are used to monitor acceptor (group III) and donor (group IV) levels as a function on the size of the nanocrystallites. However, the predictions of impurity levels are certainly limited by the well-known energy-gap problem of DFT. Since, as discussed above, GW calculations now allow very accurate calculations of energy gaps and also confirm that the gaps predicted by hybrid functional are in consistently good agreement with the many-body results, I expect that this will boost the use of VASP in *ab initio* simulations of semiconductors.

First results have recently been presented for lead chalcogenides⁹⁶—since these materials are narrow-gap materials, this is a serious test for the theory. Calculations including spin-orbit (fully relativistic for the core electrons and by the second-variation method for the valence states) have been performed using the PBE and HSE03 functionals and in addition GW_0 calculations have been performed to validate the results obtained with the hybrid functional. The lead chalcogenides are a very difficult case for DFT calculations - if SOC is properly included standard GGA calculations predict *negative* band gaps at the *L* point and much too low carrier masses.

The results compiled in Table 4 demonstrate that the HSE03 calculations including SOC predict band gaps in reasonable agreement with experiment (with a maximum error of 0.1 eV), and also the correct order of the band gaps within the series. The GW_0 calculations achieve, as expected, even better agreement with experiment. The hybrid functionals have also been used to calculate longitudinal and transverse effective masses at the valence-band maximum (VBM) and the conduction band minimum (CBM), achieving excellent agreement with experiment, while PBE calculations predict masses which are too large by a factor of 2 to 3.

Table 4. Fundamental Band Gaps E_g (in eV) of the Lead Chalcogenides at the *L* Point, as Calculated Without or With Spin-Orbit Coupling (SOC) Using a Standard GGA Functional (PBE), a Hybrid Functional (HSE03), and Using the GW_0 Approach, after Hummer et al.⁹⁶

Method	PbS	PbSe	PbTe
PBE	0.37	0.30	0.73
PBE+SOC	−0.01	−0.12	−0.01
HSE03	0.67	0.58	0.98
HSE03+SOC	0.31	0.18	0.25
GW_0 +SOC	0.45	0.23	0.30
Experiment	0.41	0.28	0.31

The largest potential of hybrid-functional calculations for semiconductors is certainly in the determination of defect levels. Tanaka, Oba and Kresse³⁰⁴ have used the hybrid functionals implemented in VASP to investigate defects (charged and neutral oxygen vacancies and Zn self interstitial) in ZnO, using supercells with up to 192 atoms to achieve realistic defect concentrations. As the O vacancy level lies about 1 eV from the CBM and 2.5 eV from the VBM, only the HSE03 calculations predicting a band gap of 3.5 eV (in agreement with experiment) can provide a realistic description, while GGA calculations fail quite badly, since they predict a gap of only 0.7 eV.

However, hybrid functional calculation for large supercells are still computationally very demanding. As a cheap alternative, van de Walle^{305,306} has recently proposed to use the DFT+U ability implemented in VASP to achieve an improved description of band offsets, defect formation energies and related quantities in semiconductors. The approach is based on the idea that the underestimation of the band gaps is partially due to the underestimation of the binding energies of the semicore *d*-states. The Hubbard potential is applied to the completely filled *d*-band. In a series of studies it was demonstrated that, although the band-gap error is only partially corrected, this leads to a much better description of semiconductor-interfaces and point defects.

Calculations of the static and frequency-dependent dielectric constants of semiconductors and insulators within the PAW formalism and the LDA have been presented by Gajdos et al.¹⁵⁸ The approach is based on the longitudinal expression for the polarizability matrix and uses either a summation over conduction band states or linear response theory. Very recently Paier³⁰⁷ has used time-dependent DFT in combination with a hybrid-functional (HSE03) and local field corrections to calculate static and frequency-dependent dielectric functions for a number of semiconductors and insulators. Excellent agreement with experiment is achieved: the improved gap-width due to the admixture of exact exchange corrects the low-frequency on-set of the absorption spectra, local-field corrections lead to an improved description of excitonic effects.

Surfaces, interfaces, and thin films

The investigation of solid surfaces and thin films is one of the most active research fields in the VASP developer group. Therefore VASP has been applied to a wide range of surface related problems, only a few selected studies can be mentioned here. Within VASP, surfaces are modeled by periodically repeated slabs of sufficient thickness, separated by wide vacuum regions. Early applications were devoted to diamond surfaces (including an extensive *ab-initio* MD simulation of the graphitization of the surface at high temperatures³⁰⁸). Applications to metallic surfaces included *inter alia* the quasihexagonal (1 × 5) reconstruction of the (100) surface of fcc Ir,³⁰⁹ the “clock-rotated” reconstruction of a Pd-Cu surface alloy on Cu(100)³¹⁰ and surface-segregation and its adsorption induced reversal on a Pt-Fe alloy surface.³¹¹ Recently, the studies of metallic surfaces have been extended to the fivefold surfaces of icosahedral Al-Pd-Mn³¹² and to the tenfold surfaces of decagonal-Al-Ni-Co³¹³ quasicrystals. The calculations are based on large slab-models with more than 400 atoms in the computational supercell. Figure 16 shows the characteristic arrangement of atoms with local fivefold symmetry, together with the simulated and

measured STM contrast. Characteristic features with fivefold symmetry, often referred to as the “white flower” (WF) and the “dark star” (DC) have been identified in the STM. The structural model resulting from the *ab initio* modeling of the surface structure allows to resolve the atomistic structure creating the observed pattern in the STM images and to relate it to the quasicrystalline structure built by large inter-penetrating Mackay and Bergman clusters.³¹² In particular the DS feature could be identified with surface vacancies originating from the irregular structure surrounding the Mn-centered Mackay clusters.

Adatoms such as oxygen often induce complex surface reconstructions or the formation of ultrathin layers of surface oxides with stoichiometries and structures which are entirely different from the bulk oxides. Traditional experimental methods such as low energy electron diffraction (LEED), surface X-ray diffraction and scanning tunneling microscopy are often insufficient to resolve the surface structure. High-performance computing offers several interesting approaches: Dynamical simulated annealing may be used for searching possible structures in configuration space. This approach has been used, e.g., to determine the structures of the oxygen-induced $c(6 \times 2)$ reconstruction of a V(110) surface³¹⁵ or the structure of two-dimensional surface oxides.³¹⁶ Alternatively, genetic algorithms may be used to solve complex surface structures.³¹⁷ An important ingredient of these studies is the calculation, in the grand canonical ensemble, of the surface free energy as a function of the chemical potential of oxygen in the reactive atmosphere above the surface which allows to determine the limits of stability of different surface phases. Recent studies include surface-oxidation on different surfaces of Rh (including vicinal surfaces),^{318,319} Pd,³²⁰ and Ag.³²¹ On Rh(110) surfaces for example, combined studies by *ab initio* calculations and STM have revealed $(2 \times 2)p2mg$, $c(2 \times 6)$, and $c(2 \times 8)$ missing-row reconstructions with increasing exposure to oxygen.

Ab initio calculations combined with experiment have elucidated the physical mechanisms leading to the formation of quasi-one dimensional surface structures on Pt(110), induced by the adsorption of Br. The adsorption provokes a missing-row reconstruction of the substrate and the formation of close-packed rows of Br in the troughs of the surfaces.³²² It has been shown that the reconstructed Br/Pt(110) surface acts as a template for growing one-dimensional arrays of adsorbates.

Investigation of the surfaces of bulk oxides have included the polar ZnO(0001) surface³²³ and surfaces of strongly correlated oxides treated in the GGA+U approach such as NiO,³²⁴ Fe₂O₃ (hematite) and Cr₂O₃ (chromia)³²⁵ and MnO.^{326,327} For the three last surfaces it was demonstrated that the on-site Coulomb potential required to describe electronic correlation effects in the narrow *d*-bands induces a re-ordering of different surface terminations. On the polar MnO(111) surface the corrections for strong correlation favor an oxygen-terminated octopolar surface over a wide range of the chemical potential of oxygen, only under strongly oxidizing conditions a reconstructed stripe-phase becomes energetically favored. Similar effects had been noted for hematite and chromia.³²⁵

Extended studies of the (001) surface of anatase-TiO₂ and of the (110) and (100) surface of γ -Al₂O₃ under various reaction conditions (varying partial pressures of H₂O, H₂S, H₂ and varying temperature) have been performed by Digne et al.^{328,329} and Arrouvel et al.^{330,331} These studies allow to determine the precise degree

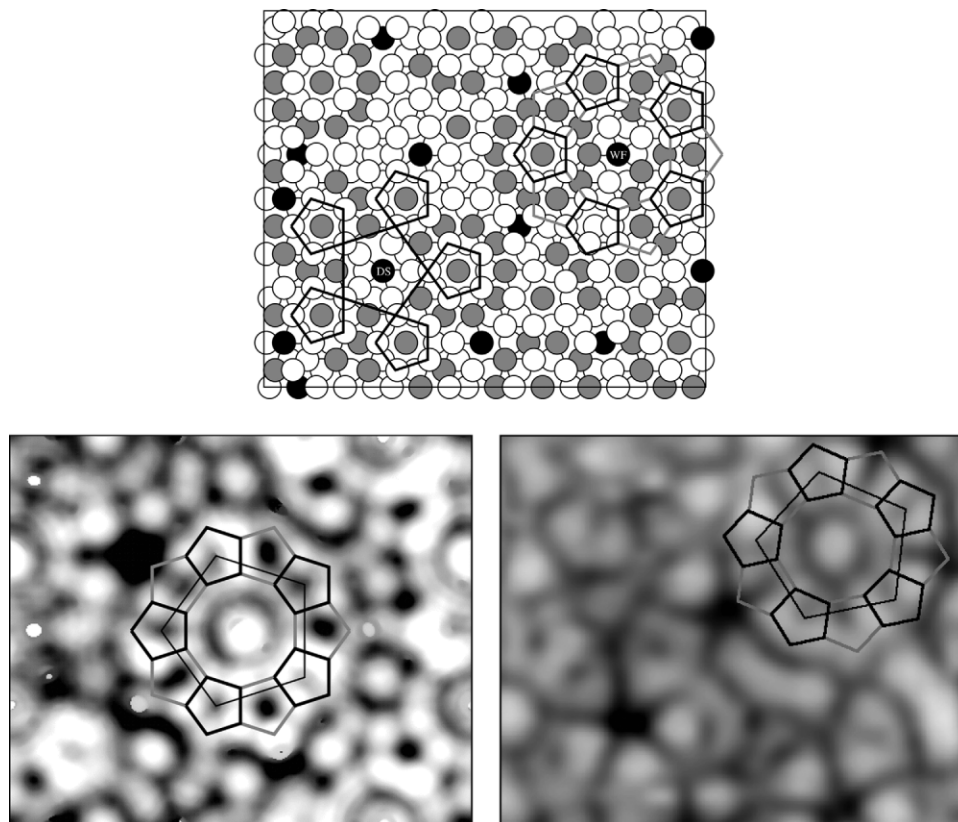


Figure 16. Top: Atomic structure of a section of a fivefold surface of an icosahedral AlPdMn quasicrystal. Aluminum atoms are shown in white, Pd in gray and Mn in black. Two characteristic motifs with fivefold symmetry, commonly nicknamed the “dark star” (DS) and the “white flower” (WF) are highlighted. Bottom: The left and right panels show the simulated and measured STM contrast around one of the ‘white flowers’, the pentagonal structure of the support is indicated. Note that both pictures also show the signatures of ‘dark stars’ associated with surface vacancies. After Krajčí et al.³¹⁴

of hydroxylation of the surfaces and the structure of the catalytically active sites under realistic working conditions.

Ultrathin oxide films formed on other metallic substrates offer a particularly rich phase diagram with many novel structures. That ultrathin alumina films can be formed on NiAl(110) alloy surfaces had been known for about thirty years, but their complex structure remained unresolved until the recent *ab initio* studies.³³² Using dynamical simulated annealing, genetic algorithms and the comparison of simulated STM images with experiment the structure could finally be resolved. The studies have also been extended to defects structures induced by a partial reduction of the films.³³³ Similar complex structures are also observed for oxide films produced by the oxidation of Ni₃Al(111) surfaces.³³⁴ The oxide films show $(\sqrt{67} \times \sqrt{67})R12.2^\circ$ periodicity with respect to the unit cell of an ordered Ni₃Al(111) surface, which makes an *ab initio* simulation a rather challenging task. Kresse has performed dynamical simulated annealing calculations for the complete surface cell which contains 721 atoms in the oxide layer, together with the substrate layers, the computational cell contained 1257 atoms. In perfect agreement with the atomically resolved STM images, the relaxed surface structure shows sixfold (at the corners of the surface cell), threefold and twofold rotation axes (see Fig. 17). The DFT simulations also

provide clear building rules for the structure of the oxide layer as imposed by the strong chemical ordering of the surface of the substrate. The hexagonal rings of atoms around the sixfold axes are empty - these holes in the oxide films should be able to capture metallic adatoms and for this reason the films could be attractive templates for growing ordered structures of metallic clusters. Well ordered Pd and Pd Au clusters have been grown, while attempts to grow ordered structures of other metals failed. DFT simulations demonstrated that Pd atoms diffusing on the oxide surfaces are easily incorporated in the six-fold holes, while a barrier of about 0.2 eV prevents a jump of a diffusing Fe atom into the hole.

Extensive investigation of ultrathin VO_x films grown on Pd(111) and Rh(111) surfaces have been performed by Kresse in cooperation with experimentalists. A large variety of different thin-film oxides has been observed experimentally, but details of their structure and chemical identity could only be resolved on the basis of *ab initio* simulations. A compilation of many results may be found in a recent review.³³⁵

Ab initio calculations have also been used to resolve the atomic structure of quasiperiodic mono- and bilayers grown on the surfaces of icosahedral quasicrystals,^{336,337} based on an extended potential-energy mapping of the quasicrystalline surface.

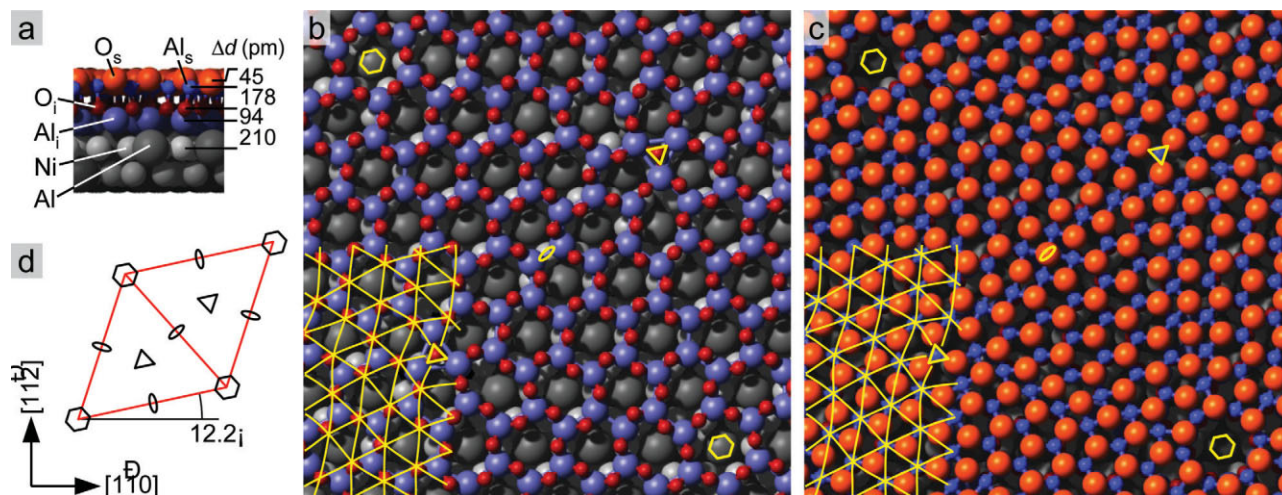


Figure 17. Atomic structure of an oxide film on $\text{Ni}_3\text{Al}(111)$ as determined by DFT optimization: (a) side view, (b) interface, (c) surface. The superposed grid lines indicate the distorted hexagonal lattice of the Al surface atoms, symbols mark the hexagonal, trigonal and twofold rotation axes of the unit cell sketched in (d). After Schmid et al.³³⁴

Adsorption, chemical reactions, and catalysis

DFT simulations have been used extensively for the simulation of chemical reactions catalyzed by solid surfaces - to some extent it even appears to be legitimate to say that the rapid development of the DFT methodology was driven by the strong interest in atomistic simulations of catalytic reactions - for a recent review of the field see, e.g., the article by Nørskov, Scheffler, and Toulhoat.³³⁸

VASP has been used to study molecular and dissociative adsorption of molecules on solid surfaces, ranging from simple diatomics^{339–341} to larger organic molecules,^{342,343} to model oxidation, redox^{344,345} and hydrogenation^{87,346} reactions catalyzed by metallic surfaces. Applications to industrially relevant reactions include hydro-desulfurization catalyzed by transition-metal sulphides,³⁴⁷ the hydrogen production by water gas shift catalysts,³⁴⁸ and hydrocarbon conversion reactions catalyzed by microporous solid acids.³⁴⁹

The studies of adsorption of CO ³³⁹ and NO ³⁴⁰ on the close-packed surfaces of late transition and noble metals have allowed to establish systematic trends in the adsorption behavior (including the vibrational properties of the adsorbate-substrate complex), for NO the determination of the activation energies for dissociation based on nudged-elastic band calculations has allowed to underpin the validity of a generalized Brønsted-Evans-Polanyi³⁵⁰ relation between the transition-state energy and the adsorption energy of the dissociation products. For light molecules such as hydrogen, the adsorption dynamics is strongly influenced by quantum effects, and DFT calculations may provide the information on the six-dimensional potential-energy surface required to perform quantum-dynamics simulations for the dissociation process.³⁴¹

Ab initio calculations of reaction rates may be performed within harmonic transition-state theory:¹⁴⁹ a search for the transition-state and a calculation of the reaction-barrier is performed using nudged-elastic band or similar techniques, the pre-exponential factor in the reaction rates is determined by the ratio of the partition functions in the transition-state and the initial-state. For tightly

bound transition-states the partition functions are derived from the vibrational eigenfrequencies. *Ab initio* calculations of reaction rates have been performed for CO oxidation on Pt surfaces,³⁴⁴ for the redox reaction between CO and NO,³⁴⁵ for the hydrogenation of benzene to cyclohexene catalyzed by a Ni(111),⁸⁷ and for the hydrogenation of formaldehyde and ethylene on Pt and PtFe alloy surfaces. In general, GGA calculations yield good agreement with experimental reaction rates: the DFT error in the adsorption energies in the initial and transition-states cancels out in the calculation of the reaction barrier, and the good agreement achieved for the vibrational eigenmodes also leads to accurate values for the prefactors. The calculated reaction rates agree with experiment over a wide range of temperatures.

Motivated by the environmental importance, a lot of effort has been spent on modeling hydro-desulfurization reactions of reactants such as thiophene catalyzed by transition-metal sulphides.^{347,351} The catalysts are layered transition-metal sulphides like MoS_2 or WS_2 whose catalytic activity is enhanced by doping with ‘promoters’ such as Ni or Co. The catalytically active sites are coordinatively unsaturated metal sites exposed at the edges of the MoS_2 sheets, whereas the basal planes are inert. The morphology of the MoS_2 crystallites and the sulfur content of the exposed edge-facets in equilibrium with the reactive atmosphere consisting mainly of H_2 and H_2S is one of the key factors for understanding the working of the catalyst. *Ab initio* DFT calculations of the surface energies of MoS_2 crystallites³⁵² allow to determine the equilibrium crystallite shape and the S-decoration of the edges under varying partial pressures and temperatures, providing excellent agreement with experiment.³⁵³ DFT simulations also allow to elucidate the role of promoters: Co or Ni atoms substitute Mo at the outer edges, contributing to a reduction of the sulfur content.³⁵⁴ The reaction is also strongly influenced by the interaction of the catalyst with the support (usually γ -alumina or anatase). Detailed simulations of small Mo-S clusters anchored on the hydroxylated surfaces of the supports^{355,356} have demonstrated that the shape and orientation of the crystallites depend on the chemical potential

of sulfur in the reactive atmosphere. Under strongly sulphideing conditions, the MoS₂ platelets lies parallel to the surface and the edges are fully S-saturated, while in a more reductive environment tilted or perpendicular orientations with exposed active sites at the edges are stabilized. Anatase supports tend to support a lower S-content - in agreement with the observed increased catalytic activity. Altogether, these studies nicely illustrate the capacity of *ab initio* DFT simulations to contribute to the design of improved catalysts.

The recent work of Opalka et al.³⁴⁸ describes the development of Pt/ceria-zirconia water gas shift catalysts by coordinated efforts in atomic modeling, catalyst synthesis, structural characterization and kinetic reaction analyses and performance tests. Atomic modeling was used to interpret possible ligand configurations and blocking of active sites on ceria-zirconia surfaces via associative reactions, as suggested by the results of in-situ spectroscopies. *Ab initio* modeling was also used for the screening of new ceria-zirconia catalysts doped with transition-metals (Nb, Mo, Ta, W) - the results predicted a more efficient re-oxidation in the regenerative steps of the water-gas shift reaction which significantly enhanced the turnover rates.

The atomistic modeling of chemical reactions in microporous solid-acid catalysts such a protonated or metal-exchanged zeolites of aluminosilicophosphates (SAPO's) was for a long time the domain of quantum-chemical simulations on finite clusters. It is known, however, that the reactivity of Brønsted and Lewis acid sites depends significantly on the location of the site in the framework and that the geometry of cavities and channels in the zeolites plays an important role in determining the selectivity of the catalyst. VASP has been used extensively for the characterization of Brønsted sites in protonated zeolites^{357,358} and of Lewis sites in metal-exchanged zeolites³⁵⁹⁻³⁶¹ and SAPO's.²¹³ These simulations have demonstrated that the efficiency of VASP is sufficient to model even zeolites with large unit cells such as mordenite or faujasite. Investigations of the chemisorption of hydrocarbon molecules^{362,363} and of ammonia³⁶⁴ have demonstrated the important role of the geometry and the flexibility of the zeolitic framework on the adsorption process. Combined with nudged elastic band calculations and harmonic transition-state theory VASP has been used to model a series of reactions catalyzed by acid zeolites: isomerization of pentene, toluene, xylene and of thiophenic derivatives,³⁶⁵⁻³⁶⁷ the alkylation of toluene with methanol,³⁶⁸ the cracking of thiophenic derivatives.³⁶⁹ A particularly ambitious study was the modeling of the Beckmann rearrangement of cyclohexanone to ϵ -caprolactam in the gas phase, catalyzed by acid mordenite.³⁷⁰ A comparative investigation of the barriers and rates for all steps of the reaction catalyzed by a Brønsted site in bulk mordenite, by silanol nests formed by lattice defects, and by terminal silanol groups at the outer surface was performed, demonstrating that only Brønsted sites are the active catalytic center. More information on *ab initio* modeling of zeolite catalysis may be found in a recent review.³⁴⁹

Within harmonic transition-state theory entropy effects on reaction rates are considered only insofar as they are described by the variation of the vibrational degrees of freedom along the reaction path. This is adequate only for reactions where reactant and transition-states are bound relatively tightly to the catalyst. For complex, rather loosely bound systems where soft degrees of freedom

such as hindered rotations or translations undergo changes during the reaction, a more comprehensive treatment of entropic effects, i.e. a calculation of the free-energy profile of the reaction is required. Many techniques for the determination of free-energy transition-states have been proposed in the literature - the drawback is that in combination with *ab initio* calculations of interatomic forces all are computationally very demanding. Very recently Bucko³⁷¹ has implemented two free-energy methods in VASP: thermodynamic integration based on constrained molecular dynamics along a possible reaction path³⁷² and metadynamics³⁷³ which allows to determine multidimensional free-energy surfaces for chemical reactions by including additional degrees of freedom which are used to drive the system towards the reactant state. A first application to an interesting reaction in a zeolite was devoted to proton-exchange between hydrocarbon molecules and Brønsted sites in chabazite.³⁷⁴ For these reactions, the origin of regioselectivity, i.e. the much faster exchange rate for methyl than for methine groups could not be explained on the basis of the calculated or measured barriers in the potential energy. Figure 18 shows in part (a) the transition-state for the proton exchange of between a methyl group of isobutane and an acid site in chabazite. Part (b) shows the variation of the free-energy and of the entropy along the reaction path for a proton exchange with a methyl or a methine group. The lower free-energy barrier leads to a much faster proton exchange by a methyl group. The analysis of the entropy profile shows that the difference stems mostly from the larger loss of entropy when a methine group forms an adsorption complex, while the work required to break the C-H bond is nearly the same in both cases.

Entropic effects have also been discussed for branching reactions of a linear carbocation (nonenium ion) catalyzed by an ionic liquid consisting of pyridinium cations and aluminum chloride anions.³⁷⁵ *Ab initio* MD simulations show that the branching reaction proceeds via a closed transition state involving a protonated cyclopropane structure (as also observation in isomerization reactions catalyzed by a zeolite³⁶⁵), but entropy effects are found to favor open against closed molecular structures. Preliminary results of simulations of monomolecular cracking of hydrocarbons show that again entropy plays a very important role.

Outlook

I have made an attempt to discuss the implementation of different DFT and post-DFT approaches in the Vienna *ab-initio* simulation package VASP and the progress realized by their application in many areas of solid-state physics and chemistry and in materials science. Of course this could only describe the actual state of development of the methodology and of its applications. The development of DFT and post-DFT methods leading even more accurate energies and geometries, and their implementation in efficient and easy-to-use codes is a dynamical process. The quest for more accurate energies, treatment of even larger systems, access to the calculations of new materials properties and the simulation of processes continues.

For example, although the GW approach has been developed to a point where systematically improved and very accurate predictions of quasiparticle spectra may be achieved, the calculation of similarly accurate total energies based on many-body perturbation theories

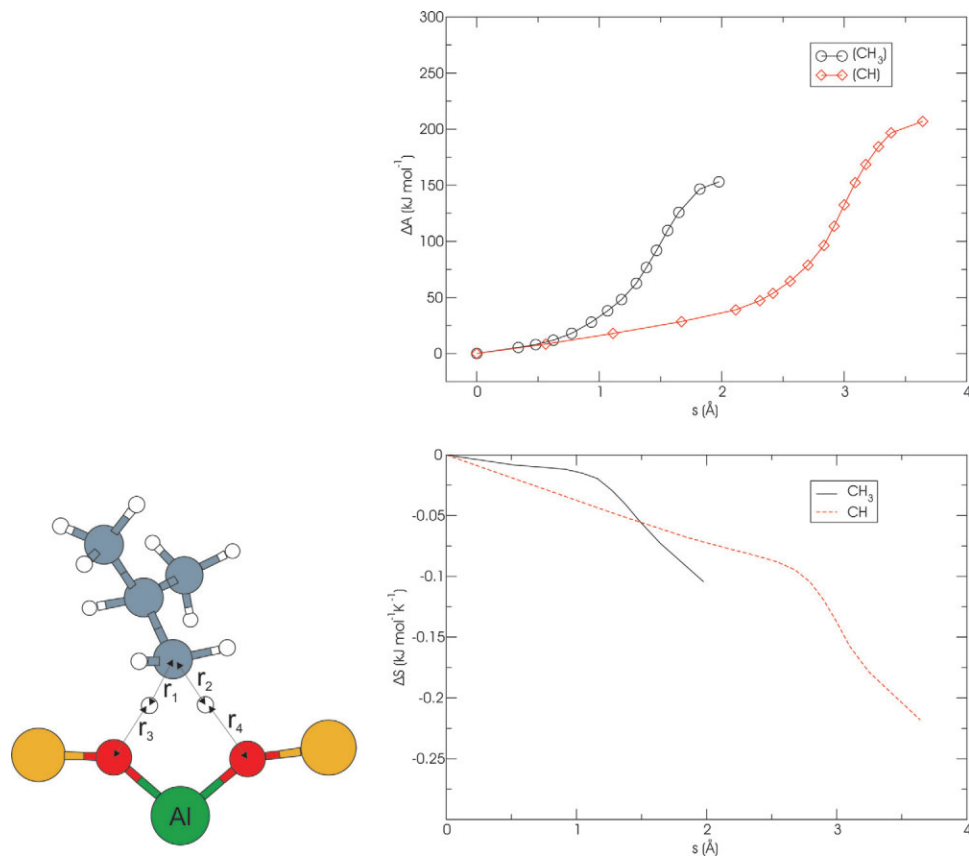


Figure 18. Left: Transition state for the proton exchange between a Brønsted site in a zeolite and a methyl group of isobutane. Right: Free-energy profile and entropy profile for the proton exchange with a methyl or a methine group of isobutane with an acid site in chabazite. After Bucko et al.³⁷⁴ [Color figure can be viewed in the online issue, which is available at www.interscience.wiley.com.]

is not yet possible. Future attempts to achieve more accurate total energies will also draw on the experience from quantum-chemical methods such as MP2 or coupled clusters.

Attempts to extend the applicability of *ab initio* DFT methods to even larger systems have been greatly assisted by the improved performance of commodity clusters. The challenge is now to improve the performance of calculations involving computationally more demanding approaches such as hybrid functionals or GW.

Finally, with applications of the methods spreading to ever new areas, new “tools” for the calculation of materials properties, spectra, processes will be required. This exceeds by far the potential of a single group of developers. Here we hope that the development of the different phonon packages added to VASP will set an example.

Acknowledgments

This review could not have been written without the contributions from the members of the Computational Materials Science Group at the Universität Wien. Special thanks are due to Georg Kresse who has always been the mastermind behind the development of VASP.

References

1. Kohn, W.; Sham, L. J. *Phys Rev A* 1964, 140, 1133.
2. Parr, R. G.; Yang, W. *Density Functional Theory of Atoms and Molecules*; Oxford University Press: Oxford, UK, 1989.
3. Perdew, J. P.; Schmidt, K. In *Density Functional Theory and its Applications to Materials*; Van Doren, V.; van Alsenoy, C.; Geerlings, P., Eds.; AIP: Melville, NY, 2001.
4. Perdew, J. P.; Kurth, S. In *A Primer in Density Functional Theory*; Fiolhais, C.; Nogueira, F.; Marques, M., Eds.; Lecture Notes in Physics, vol. 620; Springer: Berlin, 2003.
5. Perdew, J. P.; Zunger, A. *Phys Rev B* 1981, 23, 5048.
6. Becke, A. D. *Phys Rev A* 1988, 38, 3098.
7. Becke, A. D. *J Chem Phys* 1993, 98, 1372.
8. Perdew, J. P. *Phys Rev B* 1986, 33, 8822.
9. van Voorhis, T.; Scuseria, G. E. *J Chem Phys* 1998, 109, 400.
10. Boese, A. D.; Handy, N. C. *J Chem Phys* 2002, 116, 9559.
11. Becke, A. D. *J Chem Phys* 1998, 109, 2092.
12. Tao, J. *J Chem Phys* 2001, 115, 3519.
13. (a) Tao, J. *J Chem Phys* 2002, 116, 2335; (b) Tao, J. *J Chem Phys* 2002, 116, 10557 (E).
14. Kurth, S.; Perdew, J. P.; Blaha, P. *Inter J Quantum Chem* 1999, 75, 889.
15. Stevens, P. J.; Devlin, F. J.; Chablowski, C. F.; Frisch, M. J. *J Phys Chem* 1994, 80, 11 623.
16. Becke, A. D. *J Chem Phys* 1993, 98, 5648.

17. Tao, J.; Perdew, J. P.; Staroverov, V. N.; Scuseria, G. E. *Phys Rev Lett* 2003, 91, 146401.
18. (a) Perdew, J. P.; Kurth, S.; Zupan, A.; Blaha, P. *Phys Rev Lett* 1999, 82, 82, 2544; (b) Perdew, J. P.; Kurth, S.; Zupan, A.; Blaha, P. *Phys Rev Lett* 1999, 82, 5179 (erratum).
19. Paier, J.; Marsman, M.; Kresse, G. *J Chem Phys* 2007, 127, 024103.
20. (a) Perdew, J. P.; Burke, K.; Ernzerhof, M. *Phys Rev Lett* 1996, 77, 3865; (b) Perdew, J. P.; Burke, K.; Ernzerhof, M. *Phys Rev Lett* 1997, 78, 1396 (erratum).
21. Staroverov, V. N.; Scuseria, G. E.; Tao, J.; Perdew, J. P. *Phys Rev B* 2004, 69, 075102.
22. Staroverov, V. N.; Scuseria, G. E.; Tao, J.; Perdew, J. P. *J Chem Phys* 2003, 119, 12129.
23. Tao, J.; Perdew, J. P.; Ruzsinszky, A.; Scuseria, G. E.; Csonka, G.; Staroverov, V. N. *Philos Mag* 2007, 87, 1071.
24. Perdew, J. P.; Constantin, L. A.; Sagvolden, E.; Burke, K. *Phys Rev Lett* 2006, 97, 223002.
25. Perdew, J. P.; Ruzsinszky, A.; Csonka, G. I.; Vydrov, O. A.; Scuseria, G. E.; Constantin, L. A.; Zhou, X.; Burke, K. *Phys Rev Lett* 100, 136406 (2008).
26. Car, R.; Parrinello, M. *Phys Rev Lett* 1985, 55, 2471.
27. Hafner, J.; Wolverton, C.; Ceder, G. Eds. *Topical Issue, MRS Bulletin* 2006, 31:9.
28. Hedin, L.; Lundqvist, S. In *Solid State Physics*; Ehrenreich, H., Seitz, F., Turnbull, D., Eds.; Academic Press, New York, 1969; vol. 23, p. 1.
29. Hybertsen, M. S.; Louie, S. G. *Phys Rev B* 1986, 34, 5390.
30. George, A.; Kotliar, G.; Krauth, W.; Rozenberg, M. J. *Rev Mod Phys* 1996, 68, 13.
31. Held, K.; Andersen, O. K.; Feldbacher, M.; Yamasaki, A.; Yang, Y. F. *J Phys Condens Matter* 2008, 7, 064203.
32. Kresse, G.; Hafner, J. *Phys Rev B* 1993, 47, 558.
33. Kresse, G.; Furthmüller, J. *Computat Mater Sci* 1996, 6, 15.
34. Kresse, G.; Furthmüller, J. *Phys Rev B* 1996, 54, 11 169.
35. Kresse, G.; Joubert, D. *Phys Rev B* 1999, 59, 1758.
36. Blöchl, P. E. *Phys Rev B* 1994, 50, 17 953.
37. Paier, J.; Hirschl, R.; Marsman, M.; Kresse, G. *J Chem Phys* 2005, 122, 234102.
38. Frisch, M. J.; Trucks, G. W.; Schlegel, H. B.; et al. *GAUSSIAN03, Revision B.02*, Gaussian Inc.; Wallingford, CT, 2004.
39. Gruber, M.; Heimele, G.; Romaner, L.; Brédas, J.-L.; Zojer, E. *Phys Rev B* 2008, 77, 165411.
40. Soler, J. M.; Artacho, E.; Gale, J. D.; Garcia, A.; Junquera, J.; Ordejon, P.; Sanchez-Portal, D. *J Phys Condens Matter* 2002, 14, 2745.
41. Kresse, G.; Hafner, J. *J Phys Condens Matter* 1994, 6, 8245.
42. Troullier N.; Martins, J. L. *Phys Rev B* 1993, 43, 1993.
43. Vanderbilt, D. *Phys Rev B* 1990, 41, 7892.
44. Louie, S. G.; Froyen, S.; Cohen, M. L. *Phys Rev B* 1982, 26, 1738.
45. Singh, D. J. *Plane Waves, Pseudopotentials and the LAPW Method*; Kluwer Academic, Norwell, MA, 1994.
46. Feynman, R. *Phys Rev* 1939, 56,340.
47. Pulay, P. *Molec Phys* 1969, 17,197.
48. Blaha, P.; Schwarz, K.; Madsen, G. K. H.; Kvasnicka, D.; Luitz, J. *WIEN2k, An Augmented Plane Wave + Local Orbitals Program for Calculating Crystal Properties*; Technische Universität Wien, Wien, 2001. ISBN 3-9501031-1-2.
49. Heyd, J.; Scuseria, G. E. *J Chem Phys* 2004, 118, 8207.
50. Paier, J.; Marsman, M.; Hummer, K.; Kresse, G.; Gerber, I. C.; Ángyán, J. G. *J Chem Phys* 2006, 124, 154709.
51. Kiejna, A.; Kresse, G.; Rogal, J.; De Sarkar, A.; Reuter, K.; Scheffler, M. *Phys Rev B* 2006, 73, 035404.
52. Marsman, M.; Kresse, G. *J Chem Phys* 2006, 125, 104101.
53. VASP code. 2008. Available at: www.cms.mpi.univie.ac.at/vasp.
54. Koelling, D. D.; Harmon, B. N. *J Phys C* 1977, 10, 3107.
55. Lebacqz, O.; Kresse, G. Unpublished.
56. Teter, M. P.; Payne, M. C.; Joannopoulos, J. D. *Phys Rev B* 1989, 40, 12 255.
57. Stich, I.; Car, R.; Parrinello, M.; Baroni, S. *Phys Rev B* 1989, 39, 4997.
58. Davidson, E. R. In *Methods in Computational Molecular Physics*; Diercksens, G. H. F.; Wilson, S.; Eds.; NATO Advanced Study Institutes, Series C, vol. 113, Plenum, New York, 1983, p. 95.
59. Bylander, D. M.; Kleinman, L.; Lee, S. *Phys Rev B* 1990, 42, 1394.
60. Pulay, P. *Chem Phys Lett* 1980, 73, 393.
61. Wood, D. M.; Zunger, A. *J Phys A* 1985, 18, 1343.
62. Ramos, L. E.; Furthmüller, J.; Scolaro, L. M. R.; Leite, J. R.; Bechstedt, F. *Phys Rev B* 2003, 66, 075209.
63. Kresse, G.; Dulub, O.; Diebold, U. *Phys Rev B* 2003, 68, 245409.
64. Alfé, D. *Phys Rev B* 2003, 68, 064423.
65. Ceperley, D. M.; Alder, B. J. *Phys Rev Lett* 1980, 45, 466.
66. von Barth, U.; Hedin, L. *J Phys. C* 1972, 5, 1629.
67. Vosko, S. H.; Wilk, L.; Nusair, M. *Can J Phys* 1980, 58, 1200.
68. (a) Perdew, J. P.; Wang, Y. *Phys Rev B* 1992, 45, 13 244; (b) Perdew, J. P.; Chevary, A.; Vosko, S. H.; Jackson, A.; Pederson, M. R.; Singh, D. J.; Fiolhais, C. *Phys Rev B* 1992, 46, 6671; (c) Perdew, J. P.; Chevary, A.; Vosko, S. H.; Jackson, A.; Pederson, M. R.; Singh, D. J.; Fiolhais, C. *Phys Rev B* 1993, 48 4978 (Erratum).
69. Hammer, B.; Hansen, L.B.; Norskov, J. K. *Phys Rev B* 1999, 59, 7413.
70. Armiento, R.; Mattson, A. E. *Phys Rev B* 2005, 72, 085108.
71. Wu, Z.; Cohen, R. E. *Phys Rev B* 2006, 73, 235116.
72. Constantin, L. A.; Perdew, J. P.; Tao, J. *Phys Rev B* 2006, 73, 205104.
73. Tran, F.; Laskowski, R.; Blaha, P.; Schwarz, K. *Phys Rev B* 2007, 75, 115131.
74. Mattson, A. E.; Armiento, R.; Paier, J.; Kresse, G.; Wills, J. M.; Mattson, T. R. *J Chem Phys* 2008, 128, 084714.
75. Gajdos, M.; Eichler, A.; Hafner, J. *J Phys Condens Matter* 2005, 16, 1141.
76. Moroni, E. G.; Kresse, G.; Hafner, J. *Phys Rev B* 1997, 56, 15 629.
77. Hafner, R.; Spišák, D.; Lorenz, R.; Hafner, J. *J Phys Condens Matter* 2002, 14, 4297.
78. Gross, A. *Surf Sci Rep* 1998, 32, 291.
79. Eichler, A.; Hafner, J.; Kresse, G. *Surf Sci* 1997, 397,116.
80. Furthmüller, J.; Kresse, G.; Hafner, J. *Phys Rev B* 1994, 50, 15 606.
81. Csonka, G. I.; Vydrov, O. A.; Scuseria, G. E.; Ruzsinszky, A.; Perdew, J. P. *J Chem Phys* 2007, 126, 244107.
82. Paier, J.; Kresse, G. to be published.
83. Svendsen, P. S.; von Barth, U. *Phys Rev B* 1996, 54, 17402.
84. Hirschl, R. 2002, Thesis (Universität Wien, unpublished).
85. Dong, W.; Hafner, J. *Phys Rev B* 1997, 56, 15396.
86. Busnengo, H. F.; Crespos, C.; Dong, W.; Salin, A.; Rayez, J. C. *Phys Rev B* 2001, 63, 041402.
87. Mittendorfer, F.; Hafner, J. *J Phys Chem B* 2002, 106, 13 299.
88. Harris, J.; Jones, R. O. *J Phys F* 1974, 4, 1170.
89. Gunnarsson, O.; Lundqvist, B. I. *Phys Rev B* 1976, 13, 4274.
90. Lee, C.; Yang, W.; Parr, R. *Phys Rev B* 1988, 37, 785.
91. Adamo, C.; Barone, V. *J Chem Phys* 1999, 110, 6158.
92. Jaramillo, J.; Scuseria, G. E.; Ernzerhof, M. *J Chem Phys* 2003, 118, 1068.
93. Perdew, J. P.; Ernzerhof, M.; Burke, K. *J Chem Phys* 1996, 105, 9982.
94. Massida, S.; Posternak, M.; Baldereschi, A. *Phys Rev B* 1993, 48, 5058.
95. Makov, G.; Payne, M. C. *Phys Rev B* 1995, 51, 4041.
96. Hummer, K.; Grüneis, A.; Kresse, G. *Phys Rev B* 2007, 195211.
97. Kresse, G.; Gil, A.; Sautet, P. *Phys Rev B* 2003, 68, 073401.
98. Stroppa, A.; Termentzidis, K.; Paier, J.; Kresse, G.; Hafner, J. *Phys Rev B* 2007, 195440.
99. da Silva, J. L. F.; Ganduglia-Pirovano, V.; Sauer, J.; Bayer, V.; Kresse, G. *Phys Rev B* 2007, 75, 045121.

100. Franchini, C.; Bayer, V.; Podloucky, R.; Paier, J.; Kresse, G. *Phys Rev B* 2005, 72, 045132.
101. Franchini, C.; Podloucky, R.; Paier, J.; Marsman, M.; Kresse, G. *Phys Rev B* 2007, 75, 195128.
102. Almladh, C. O.; von Barth, U. *Phys Rev B* 1985, 31, 3231.
103. Savin, A. In *Recent Developments and Applications of Modern Density Functional Theory*; Seminario, J. M.; Ed.; Elsevier: Amsterdam, 1996; p. 327.
104. Leininger, T.; Stoll, H.; Werner, H. J.; Savon, A. *Chem Phys Lett* 1997, 275, 151.
105. Gerber, I. C.; Ángyán, J. C. *Chem Phys Lett* 2005, 415, 100.
106. Vydrov, O. A.; Scuseria, G. E. *J Chem Phys* 2006, 125, 234109.
107. Sekino, H.; Maeda, Y.; Kamiya, M.; Hirao, K. *J Chem Phys* 2007, 126, 014107.
108. Gerber, I. C.; Ángyán, J. C.; Marsman, M.; Kresse, G. *J Chem Phys* 2007, 127, 054101.
109. Lee, D. H.; Joannopoulos, J. D.; Negele, J. W.; Landau, D. P. *Phys Rev B* 1986, 33, 450.
110. Jensen, J.; Mackintosh, A. R. 1991 *Rare Earth Magnetism*; Clarendon: Oxford.
111. Lorenz, R.; Hafner, J. *J Magn Magn Mater* 1995, 139, 209.
112. Kübler, J.; Höck, K. H.; Sticht, J.; Williams, A. R. *J Phys F* 1988, 63, 3482.
113. Oda, T.; Pasquarello, A.; Car, R. *Phys Rev Lett* 1998, 80, 3622.
114. Hobbs, D.; Kresse, G.; Hafner, J. *Phys Rev B* 2000, 62, 11556.
115. Herring, C. In *Magnetism*; Rado, G. T.; Suhl, H.; Eds.; Academic Press: New York, 1966.
116. Marsman, M.; Hafner, J. *Phys Rev B* 2002, 66, 224409.
117. Hobbs, D.; Hafner, J. *J Phys Condens Matter* 2000, 12, 7025.
118. Hafner, J.; Spišák, D. *Phys Rev B* 2005, 144420.
119. Hobbs, D.; Hafner, J.; Spišák, D. *Phys Rev B* 2003, 68, 014407.
120. Lawson, A. C.; Larson, A. C.; Aronson, M. C.; Johnson, S.; Fisk, Z.; Canfield, P. C.; Thompson, J. D.; von Dreese, R. B. *J Appl Phys* 1994, 76, 7049.
121. Dudarev, S. L.; Botton, G. A.; Savrasov, S. Y.; Humphreys, C. J.; Sutton, A. P. *Phys Rev B* 1998, 75, 1505.
122. Lichtenstein, A. I.; Anisimov, V. I.; Zaanen, J. *Phys Rev B* 1995, 52, 5467.
123. Bengone, O.; Alouani, M.; Blöchl, P.; Hugel, J. *Phys Rev B* 2000, 62, 16392.
124. Rohrbach, A.; Kresse, G.; Hafner, J. *J Phys Condens Matter* 2003, 15, 279.
125. Rohrbach, A.; Kresse, G.; Hafner, J. *Phys Rev B* 2004, 69, 075413.
126. Rohrbach, A.; Kresse, G.; Hafner, J. *Phys Rev B* 2004, 70, 125426.
127. Rollmann, G.; Rohrbach, A.; Entel, P.; Hafner, J. *Phys Rev B* 2004, 69, 165107.
128. Petersen, M.; Hafner, J.; Marsman, M. *J Phys Condens Matter* 2006, 18, 7021.
129. Hedin, L. *Phys Rev* 1965, 139, A796.
130. Aryasetiawan, F.; Gunnarsson, O. *Rep Prog Phys* 1998, 61, 237.
131. Furthmüller, J.; Cappellini, G.; Weissker, H. C.; Bechstedt, F. *Phys Rev B* 2002, 66, 155208.
132. Shishkin, M.; Kresse, G. *Phys Rev B* 2006, 74, 035101.
133. Shishkin, M.; Kresse, G. *Phys Rev B* 2007, 75, 235102.
134. van Schilfgaarde, M.; Kotani, T.; Faleev, S. *Phys Rev Lett* 2006, 96, 226402.
135. Friedrich, C.; Schindlmayr, A.; Blügel, S.; Kotani, T. *Phys Rev B* 2006, 045104.
136. Fuchs, F.; Furthmüller, J.; Bechstedt, F.; Shishkin, M.; Kresse, G. *Phys Rev B* 2007, 76, 115109.
137. Reining, L.; Olevano, V.; Rubio, A.; Onida, G. *Phys Rev Lett* 2002 88, 066404.
138. Bruneval, F.; Sottile, F.; Olevano, V.; Del Sole, R.; Reining, L. *Phys Rev Lett* 2006, 94, 186402.
139. Shishkin, M.; Kresse, G. *Phys Rev Lett* 2007, 99, 246403.
140. Langreth, D. C.; Perdew, J. P. *Solid State Comm* 1975, 17, 1425.
141. Furche, F. *Phys Rev B* 2001, 64, 195120.
142. Dahlen, N. E.; van Leeuwen, R.; von Barth, U. *Phys Rev A* 2006, 012511.
143. Harl, J.; Kresse, G. *Phys Rev B* 2008, 77, 045136.
144. Bučko, T.; Hafner, J.; Ángyán, J. G. *J Chem Phys* 2005, 122, 124508.
145. Oganov, A. R.; Glass, C. W. *J Chem Phys* 2006, 124, 244704.
146. Glass, C. W.; Oganov, A. R.; Hansen, N. *Comp Phys Comm* 2006, 175, 713.
147. Mills, G.; Jonsson, H.; Schenter, G. K. *Surf Sci* 1995, 324, 305.
148. Jonsson, H.; Mills, G.; Jacobsen, K. W. In *Classical and Quantum Dynamics in Condensed Phase Simulations*; Berne, B. J.; Ciccotti, G.; Coker, D. F.; Eds; World Scientific: Singapore, 1998.
149. van Santen, R. A.; Niemandsvertriet, H. W.; *Chemical Kinetics and Catalysis*; Plenum: New York, 1995.
150. Bučko, T.; Hafner, J.; Benco, L. *J Phys. Chem. A* 2004, 108, 11 388.
151. Hafner, J. *J Molec Struct* 2003, 651-653, 3.
152. Kresse, G.; Furthmüller, J.; Hafner, J. *Europhys Lett* 1995, 32, 729.
153. The PHONON package of K. Parlinski. 2008. Available at: <http://wolf.ifj.edu.pl/phonon>.
154. The PHONON package of D. Aefé. 2008. Available at: <http://chiantoni.geol.ucl.ac.uk/dario/>.
155. LePage, Y.; Saxe, P. *Phys Rev B* 2002, 65, 104104.
156. King-Smith, R. D.; Vanderbilt, D. *Phys Rev B* 1993, 47, 1651.
157. Resta, R. *Rev Mod Phys* 1994, 66, 899.
158. Gajdos, M.; Hummer, K.; Kresse, G.; Furthmüller, J.; Bechstedt, F. *Phys Rev B* 2006, 73, 045112.
159. Hafner, J.; Hobbs, D. *Phys Rev B* 2003, 68, 014408.
160. McMahon, M. I.; Degtyareva, O.; Nelves, R. J. *Phys Rev Lett* 2000, 85, 4896.
161. Häussermann, U.; Söderberg, K.; Norrestam, R. *J Amer Chem Soc* 2002, 124, 15359.
162. Neaton, J. B.; Ashcroft, N. W. *Nature* 1999, 400, 141.
163. Neaton, J. B.; Ashcroft, N. W. *Phys Rev Lett* 2001, 86, 2830.
164. Feng, J.; Hennig, R. G.; Ashcroft, N.W.; Hoffmann, R. *Nature* 2008, 451, 445.
165. Vocadlo, L.; Alfé, D.; Gillan, M. J.; Wood, I. G.; Bordholt, J. P.; Price, G. D. *Nature* 2003, 424, 536.
166. Krajčí, M.; Hafner, J. *J Phys Condens Matter* 2002, 14, 5755.
167. Jahnatek, M.; Krajčí, M.; Hafner, J. *Phys Rev B* 2005, 71, 024101.
168. Jahnatek, M.; Krajčí, M.; Hafner, J. *J Phys Condens Matter* 2003, 15, 5675.
169. Magaud, F.; Pasturel, A.; Kresse, G.; Hafner, J. *Phys Rev B* 1997, 55, 13479.
170. Moroni, E. G.; Wolf, W.; Hafner, J.; Podloucky, R. *Phys Rev B* 1999, 57, 12860.
171. Dennler, S.; Hafner, J. *Phys Rev B* 2006, 73, 174303.
172. Chen, X. Q.; Wolf, W.; Podloucky, R.; Rogl, P.; Marsman, M. *Phys Rev B* 2005, 054440.
173. Chen, X. Q.; Wolf, W.; Podloucky, R.; Rogl, P. *Phys Rev B* 2007, 014424.
174. Grytsiv, A.; Chen, X. Q.; Witusiewicz, V. T.; Rogl, P.; Podloucky, P.; Pomjakushin, V.; Maccio, D.; Saccone, A.; Giester, G.; Sommer, F. *Z Kristallogr* 2006, 221, 334.
175. Seifert-Lorenz, K.; Hafner, J. *Phys Rev B* 1999, 59, 829.
176. Genser, O.; Hafner, J. *J Phys Condens Matter* 2001, 13, 959.
177. Seifert-Lorenz, K.; Hafner, J. *Phys Rev B* 2002, 66, 094105.
178. Zayak, A. T.; Entel, P.; Hafner, J. *J Physique IV France* 2003, 112, 985.
179. Chen, X. Q.; Podloucky, R.; Rogl, P. *J Appl Phys* 2006, 100, 113901.
180. (a) Fredricksen, D. C.; Lee, S.; Hoffmann, R.; Lin, J. *Inorg Chem* 2004, 43, 6151; (b) Fredricksen, D. C.; Lee, S.; Hoffmann, R.; Lin, J. *Inorg Chem* 2004, 43, p. 6159.

181. Waitz, T.; Spišák, D.; Hafner, J.; Karnthaler, H. P. *Europhys Lett* 2005, 71, 98.
182. Manley, M. E.; Asta, M.; Lashley, J. C.; Retford, C. M.; Hulst, W. L.; Taylor, R. D.; Thoma, D. J.; Thoma, Smith, J. L.; Hackenberg, R. E.; Littrell, K. *Phys Rev B* 2008, 77, 024201.
183. Krajčí, M.; Hafner, J. *Phys Rev B* 2007, 75, 024116.
184. Inoue, A.; Kimura, H.; *Mater Sci Eng A* 2000, 286, 1.
185. Hirschl, R.; Hafner, J.; Jeanvoine, Y. *J Phys Condens Matter* 2001, 13, 3545.
186. Sanchez, J. M.; Ducastelle, F.; Gratias, D. *Physica A* 1984, 128, 334.
187. Müller, S. *J Phys Condens Matter* 2003, 15, R1429.
188. Kaufman, L.; Bernstein, H. *Computer Calculation of Phase Diagrams*; Academic Press: New York, 1970.
189. Miodownik, A. P. In *Static and Dynamics of Alloy Phase Transformations*; Turchi, P. E. A.; Gonis, A.; Eds.; Plenum: New York, 1994.
190. Wolverton, C.; Yan, X. Y.; Vijayaraghavan, R.; Ozolins, V. *Acta Mater* 2002, 50, 2187.
191. Jomard, G.; Petit, T.; Pastural, A.; Magaud, F.; Kresse, G.; Hafner, J. *Phys Rev* 1999, B 59, 4044.
192. van der Ven, A.; Aydinol, M. K.; Ceder, G.; Kresse, G.; Hafner, J. *Phys Rev B* 1998, 58, 2975.
193. Watson, G. W.; Parker, S. C.; Kresse, G. *Phys Rev B* 1999, 59, 8481.
194. Raybaud, P.; Kresse, G.; Hafner, J.; Toulhoat, H. *J Phys Condens Matter* 1997, 11085.
195. Hobbs, D.; Hafner, J. *J Phys Condens Matter* 1999, 8197.
196. Wolverton, C.; Siegel, D. J.; Akbarzadeh, A. R.; Ozolins, V. *J Phys. Condens Matter* 2008, 20, 064228.
197. Hector, L. G.; Herbst, J. F.; Wolf, W.; Saxe, P.; Kresse, G. *Phys Rev* 2007, 76, 014121.
198. Hector, L. G.; Herbst, J. F. *J Phys Condens Matter* 2008, 20, 064229.
199. Broedersz, C. P.; Gremaud, R.; Dam, B.; Griessen, R.; Løvvik, O. M. *Phys Rev B* 2008, 77, 024204.
200. Steynberg, P. J.; van den Berg, J. A.; Janse van Rensburg, W. *J Phys Condens Matter* 2008, 20, 064238.
201. Ahuja, R.; Luo, W. *J Phys Condens Matter* 2008, 20, 65217.
202. Benco, L.; Hafner, J.; Lences, Z.; Sajgalik, P. *J Eur Ceram Soc* 2008, 28, 995.
203. Tanaka, I.; Oba, F. *J Phys Condens Matter*, 2008, 20, 064215.
204. Blake, N. P.; Mollnitz, L.; Kresse, G.; Metiu, H. *J Chem Phys* 1999, 111, 3133.
205. Biswas, K.; Myles, C. W. *J Phys Condens Matter* 2007, 19, 466206.
206. Wang, L.; Maxisch, T.; Ceder, G. *Phys Rev B* 2006, 73, 195107.
207. Demuth, T.; Jeanvoine, Y.; Hafner, J.; Ángyán, J. G. *J Phys Condens Matter* 1999, 11, 3833.
208. Teter, D.; Hemley, R. J.; Kresse, G.; Hafner, J. *Phys Rev Lett* 1998, 80, 2145.
209. Jeanvoine, Y.; J. Ángyán, J. G.; Kresse, G.; Hafner, J. *J Phys Chem B* 1998, 102, 5573.
210. Demuth, T.; Hafner, J.; Benco, L.; Toulhoat, H. *J Phys Chem B* 2000, 104, 4593.
211. Benco, L.; Demuth, T.; Hafner, J.; Hutschka, F.; Toulhoat, H. *J Catalysis* 2002, 209, 480.
212. Jeanvoine, Y.; J. Ángyán, J. G.; Kresse, G.; Hafner, J. *J Phys Chem B* 1998, 102, 7307.
213. Uzunova, E. L.; Mikosch, H.; Hafner, J. *J Phys Chem C* 2008, 112, 2639.
214. Benco, L.; Tunega, D.; Hafner, J.; Lischka, H. *Chem Phys Lett* 2001, 333, 479.
215. Benco, L.; Tunega, D.; Hafner, J.; Lischka, H. *J Phys Chem B* 2001, 105, 812.
216. Stixrude, L.; Peacor, D. R. *Nature* 2002, 420, 165.
217. Oganov, A.; Ono, S. *Nature* 2004, 430, 445.
218. Brodholt, J. P.; Vočadlo, L. *MRS Bulletin* 2006, 31, 675.
219. Plazanet, M.; Fukushima, N.; Johnson, M. R.; Horsewill, A. J.; Trommsdorf, H. P. *J Chem Phys* 2001, 115, 3241.
220. Plazanet, M.; Fukushima, N.; Johnson, M. R. *Chem Phys* 2002, 280, 53.
221. Sugihara, M.; Meyer, H.; Entel, P.; Sakamoto, Y.; Hafner, J.; Buss, V. In *Structure and Thermodynamics of Heterogeneous System*; Entel, P.; Wolf, D. E.; Eds.; World Scientific: Singapore, 2000; p.36.
222. Buss, V.; Sugihara, M.; Entel, P.; Hafner, J. *J Phys Chem B* 2004, 108, 3673.
223. Jahnátek, M.; Krajčí, M.; Hafner, J. *Philos. Mag.* 2007, 87, 1769.
224. Kiefer, B.; Stixrude, L.; Hafner, J.; Kresse, G. *Amer Mineralogist* 2001, 86, 1387.
225. Oganov, A. R.; Brodholt, J. P.; Price, D. G. *Nature* 2001, 411, 934.
226. Ogata, S.; Li, J.; Yip, S. *Science* 2002, 298, 807.
227. Clatterbuck, D. M.; Chrzan, D. C.; Morris, J. W. *Acta Materialia* 2003, 51, 2271.
228. Krenn, C. R.; Roundy, D.; Cohen, M. L.; Chrzan, D. C.; Morris, J. W. *Phys Rev B* 2002, 65, 134111.
229. Li, T.; Morris, J. W.; Chrzan, D. C. *Phys Rev B* 2004, 70, 054107.
230. Jahnátek, M.; Krajčí, M.; Hafner, J. *Phys Rev B* 2007, 76, 014410.
231. Ogata, S.; Li, J.; Hirotsaki, N.; Shibusaki, Y.; Yip, S. *Phys Rev B* 2004, 70, 104104.
232. Milstein, F.; Huang, K. *Phys Rev B* 1978, 18, 2529.
233. Lazar, P.; Podloucky, R.; Wolf, W. *Appl Phys Lett* 2005, 87, 261910.
234. Lu, G. H.; Deng, S.; Wang, T.; Kohyama, M.; Yamamoto, R. *Phys Rev B* 2004, 69, 134106.
235. Shang, J. X.; Wang, C. Y. *Phys Rev B* 2002, 66, 184105.
236. Yamaguchi, M.; Shiga, M. *Kaburaki, H. Science* 2005, 307, 393.
237. Schweinfest, R.; Paxton, A. T.; Finnis, M. W. *Nature* 2004, 432, 1008.
238. Ogata, S.; Li, J.; Yip, S. *Phys Rev B* 2005, 71, 224102.
239. Kern, G.; Kresse, G.; Hafner, J. *Phys Rev B* 1999, 59, 8551.
240. Dubay, O.; Kresse, G. *Phys Rev B* 2003, 67, 035401.
241. Eichler, A.; Bohnen, K. P.; Reichardt, W.; Hafner, J. *Phys Rev B* 1998, 57, 324.
242. Grabowski, B.; Hickel, T.; Neugebauer, J. *Phys Rev B* 2007, 76, 024309.
243. Souvatzis, P.; Eriksson, O.; Katsnelson, M. I. *Phys Rev Lett* 2007, 99, 015901.
244. Souvatzis, P.; Eriksson, O. *Phys Rev B* 2008, 77, 024410.
245. Rotter, M.; Grytsiv, A.; Chen, X. Q.; Rogl, P.; Podloucky, R.; Wolf, W.; Witusiewicz, V. T.; Saccone, A.; Noel, H.; Doerr, M.; Lindbaum, A.; Michor, H.; Bauer, E.; Heathman, S.; Kockelmann, W.; Taylor, J. *Phys Rev B* 2006, 74, 224109.
246. Lodziana, Z.; Parlinski, K.; Hafner, J. *Phys Rev B* 2001, 134106.
247. Parlinski, K.; Lazewski, J.; Jochym, P. T.; Chumakow, A.; Rüffer, R.; Kresse, G. *Europhys Lett* 2001, 56, 275.
248. de Wijs, G. A.; Fang, C. M.; Kresse, G.; de With, G. *Phys Rev B* 2002, 65, 094305.
249. Eichler, A. *Phys Rev B* 2001, 64, 174103.
250. Chang, C. M.; Wei, C. M.; Hafner, J. *J Phys Condens Matter* 2001, 13, L321.
251. Spišák, D.; Hafner, J. *Phys Rev B* 2004, 70, 195426.
252. Dennler, S.; Hafner, J. *Phys Rev B* 2005, 72, 214413.
253. Kresse, G.; Hafner, J. *Phys Rev B* 1993, 48, 13115.
254. Kresse, G.; Hafner, J. *Phys Rev B* 1994, 49, 14251.
255. Tsuiji, K.; Hattori, T.; Mori, T.; Kinoshita, T.; Narushima, T.; Funamori, N. *J Phys Condens Matter* 2004, 16, S989.
256. Jakse, N.; Pasturel, A. *Phys Rev Lett* 2007, 99, 205702.
257. Kresse, G.; Hafner, J. *Phys Rev B* 1997, 55, 7539.
258. de Wijs, G.; Kresse, G.; Vočadlo, L.; Alfé, D.; Gillan, M. J.; Price, G. D. *Nature*, 1998, 392, 805.
259. Alfé, D.; Kresse, G.; Gillan, M. J. *Phys Rev B* 200, 61, 132.
260. Secco, R. A. In *Mineral Physics and Crystallography: A Handbook of Physical Constants*; Ahrens, T. J.; Ed.; American Geophysical Union: Washington, DC, 1987; p. 218.

261. Genser, O.; Hafner, J. *J Phys Condens Matter* 2001, 13, 981.
262. Genser, O.; Hafner, J. *Phys Rev B* 2001, 63, 144204.
263. Seifert-Lorenz, K.; Kresse, G.; Hafner, J. *J Non-Cryst Solids* 2001, 293-295, 193.
264. Seifert-Lorenz, K.; Hafner, J. *Phys Rev B* 1999, 59, 843.
265. Winter, R. In *Thermodynamics of Alloy Formation*; Chang, Y. A.; Sommer, F.; Eds.; The Minerals, Metals, and Materials Society: London, 1997; p. 143.
266. Jakse, N.; Pasturel, A. *J Chem Phys* 2004, 120, 6124.
267. Jakse, N.; Pasturel, A. *Phys Rev Lett* 2003, 91, 195501.
268. Jakse, N.; LeBacq, O.; Pasturel, A. *Phys Rev Lett* 2004, 93, 207801.
269. Jakse, N.; LeBacq, O.; Pasturel, A. *J Chem Phys* 2005, 123, 104508.
270. Sheng, H. W.; Luo, W. K.; Alamgir, F. M.; Bai, J. M.; Ma, E. *Nature* 2006, 439, 419.
271. Ganesh, P.; Widom, M. *Phys Rev B* 2008, 77, 014205.
272. Hausleitner, C.; Hafner, J. *Phys Rev B* 1993, 47, 5689.
273. Jakse, N.; Pasturel, A. *Europhys Lett* 2006, 74, 275.
274. East, A. L. L.; Hafner, J. *J Phys Chem B* 2007, 111, 5316.
275. Lehtinen, P. O.; Foster, A. S.; Ma, Y.; Krasheninnikov, Nieminen, R. *M. Phys Rev Lett* 2004, 93, 187202.
276. Moroni, E. G.; Kresse, G.; Hafner, J. *J Phys Condens Matter* 1999, 11, L35.
277. Muller, S.; Bayer, P.; Reischl, C.; Heinz, K.; Feldmann, B.; Zillgen, H.; Wuttig, M. *Phys Rev Lett* 1995, 74, 765.
278. Biedermann, A.; Schmid, M.; Varga, P. *Phys Rev Lett* 2001, 86, 464.
279. Spišák, D.; Hafner, J. *Phys Rev Lett* 2002, 88, 056101.
280. Spišák, D.; Hafner, J. *Phys Rev B* 2004, 70, 195426.
281. Dennler, S.; Hafner, J. *Phys Rev B* 2005, 72, 214413.
282. Hafner, J.; Spišák, D. *Phys Rev B* 2005, 72, 144420.
283. Spišák, D.; Hafner, J. *Phys Rev B* 2004, 70, 195426.
284. Spišák, D.; Hafner, J. *Phys Rev B* 2003, 67, 214416.
285. Futschek, T.; Hafner, J.; Marsman, M. *J Phys Condens Matter* 2006, 18, 9703.
286. Hafner, J.; Spišák, D. *Phys Rev B* 2007, 76, 094420.
287. Mahadevan, P.; Zunger, A.; Sarma, D.D. *Phys Rev Lett* 2004, 93, 177201.
288. Sieberer, M.; Redinger, J.; Mohn, P. *Phys Rev B* 2007, 75, 035203.
289. Seiberer, M.; Khmelevskiy, S.; Mohn, P. *Phys Rev B* 74, 014416.
290. Jeng, H.-T.; Lin, S.-H.; Huse, C.-S. *Phys Rev Lett* 2006, 97, 067002.
291. Xiang, H. J.; Whangbo, M. H. *Phys Rev Lett* 2007, 99, 257203.
292. Picozzi, S.; Yamauchi, K.; Sanyal, B.; Sergienko, I. A.; Dagotto, E. *Phys Rev Lett* 2007, 99, 227201.
293. Fennie, C. J.; Rabe, K. M. *Phys Rev Lett* 2006, 97, 267602.
294. Gao, L.; Ji, W.; Hu, Y. B.; Cheng, Z. H.; Deng, Z. T.; Liu, Q.; Jiang, N.; Lin, X.; Guo, W.; Du, S. X.; Hofer, W. A.; Xie, X. C.; Gao, H.-J. *Phys Rev Lett* 2007, 99, 106402.
295. Barraza-Lopez, S.; Avery, M. C.; Park, K. *Phys Rev B* 2007, 76, 224413.
296. Jones, E. D.; Modine, N. A.; Allerman, A. A.; Kurtz, S. R.; Wright, A. F.; Tozer, S. T.; Wei, X. *Phys Rev B* 1999, 60, 4430.
297. Windl, W.; Bunea, M. M.; Stumpf, R.; Dunham, S. T.; Masquelier, M. *Phys Rev Lett* 1999, 83, 4345.
298. Sadigh, B.; Lenosky, T. J.; Thiess, S. K.; Caturla, M. J. de la Rubia, T. D.; Foad, M. A. *Phys Rev Lett* 1999, 83, 4341.
299. Bang, K.; Kim, H.; Kang, J.; Lee, W. J.; Chang, K. J. *Physica B Condens Matter* 2007, 401, 196.
300. Zywietz, A.; Furthmüller, J.; Bechstedt, F. *Phys Rev B* 1999, 59, 15166.
301. Foster, A. J.; Sulimov, V. B.; Gejo, F. L.; Shluger, A. L. Nieminen, R. M. *Phys Rev B* 2001, 64, 224108.
302. Foster, A. S.; Gejo, F. L.; Shluger, A. L.; Nieminen, R. M. *Phys Rev B* 2002, 65, 174117.
303. Ramos, L. E.; Degoli, E.; Cantele, G.; Ossicini, S.; Ninno, D.; Furthmüller, J.; Bechstedt, F. *J Phys Condens Matter* 2007, 19, 466211.
304. Oba, F.; Togo, A.; Tanaka, I.; Paier, J.; Kresse, G. *Phys Rev B* 2008, 77, 245208.
305. Janotti, A.; Segev, D.; van de Walle, C. G. *Phys Rev B* 2006, 74, 045202.
306. van de Walle, C. G. *J Phys Condens Matter* 2008, 20, 064230.
307. Paier, J. Thesis, Universität Wien 2008.
308. Kern, G.; Hafner, J. *Phys Rev B* 1998, 58, 13167.
309. Spišák, D.; Hafner, J. *Surf Sci* 2003, 546, 27.
310. Spišák, D.; Hafner, J. *Phys Rev B* 2003, 67, 235403.
311. Hirschl, R.; Delbecq, F.; Sautet, P.; Hafner, J. *Phys Rev B* 2002, 67, 235403.
312. Krajčí, M.; Hafner, J. *Phys Rev B* 2005, 71, 054202.
313. Krajčí, M.; Hafner, J. *Phys Rev B* 2006, 73, 184202.
314. Krajčí, M.; Hafner, J.; Ledieu, J.; McGrath, R. *Phys Rev B* 2006, 73, 0204202.
315. Kresse, G.; Bergermayer, W.; Podloucky, R.; Lundgren, E.; Koller, R.; Schmid, M.; Varga, P. *Appl Phys A* 2003, 76, 701.
316. Lundgren, E.; Kresse, G.; Klein, C.; Borg, M.; Andersen, J. N.; de Santis, M.; Gauthier, Y.; Konvicka, C.; Schmid, M.; Varga, P. *Phys Rev Lett* 2002, 88, 246103.
317. Köhler, L., Thesis, Universität Wien 2007.
318. Köhler, L.; Kresse, G.; Schmid, M.; Lundgren, E.; Gustafson, J.; Mikkelsen, A.; Borg, M.; Yuhara, J.; Andersen, J. N.; Marsman, M.; Varga, P. *Phys Rev Lett* 2004, 93, 266103.
319. Dri, C.; Africh, C.; Esch, F.; Comelli, G.; Dubay, O.; Köhler, L.; Mittendorfer, F.; Kresse, G.; Dudin, P.; Kiskinova, M. *J Chem Phys* 2006 125, 09471.
320. Kostelnik, P.; Seriani, N.; Kresse, G.; Mikkelsen, A.; Lundgren, E.; Blum, V.; Sikola, T.; Varga, P.; Schmid, M. *Surf Sci* 2007, 601, 1574.
321. Costina, I.; Schmid, M.; Schiechl, H.; Gajdos, M.; Stierle, A.; Kumara-grubaran, Hafner, J.; Dosch, H.; Varga, P. *Surf Sci* 2006, 600, 617.
322. Menzel, A.; Zhang, Z.; Minca, M.; Bertel, E.; Redinger, J.; Zucca, R. *J Phys Chem Solids* 2006, 67, 254.
323. Dulub, O.; Diebold, U.; Kresse, G. *Phys Rev Lett* 2003, 90, 016102.
324. Rohrbach, A.; Hafner, J.; Kresse, G. *Phys Rev B* 2004, 69, 075413.
325. Rohrbach, A.; Hafner, J.; Kresse, G. *Phys Rev B* 2004, 70, 125426.
326. Franchini, C.; Bayer, V.; Podloucky, R.; Parteder, G.; Surnev, S.; Netzer, F. P. *Netzer Phys Rev B* 2006, 73, 155402.
327. Bayer, V.; Franchini, C.; Podloucky, R. *Phys Rev B* 2007, 75, 035404.
328. Digne, M.; Sautet, P.; Raybaud, P.; Euzen, P.; Toulhoat, H. *J Catal* 2002, 211, 1.
329. Digne, M.; Sautet, P.; Raybaud, P.; Euzen, P.; Toulhoat, H. *J Catal* 2004, 226, 54.
330. Arrouvel, C.; Digne, M.; Breysse, M.; Toulhoat, H.; Raybaud, P. *J Catal* 2004, 222, 152.
331. Arrouvel, C.; Breysse, M.; Toulhoat, H.; Raybaud, P. *J Catal* 2006, 226, 260.
332. Kresse, G.; Schmid, M.; Napetsching, E.; Shishkin, M.; Köhler, L.; Varga, P. *Science* 2005, 308, 1440.
333. Schmid, M.; Shishkin, M.; Kresse, G.; Napetschnig, E.; Varga, P.; Kulawik, M.; Nilius, N.; Rust, H.P.; Freund, H. J. *Phys Rev Lett* 2006, 97, 046101.
334. Schmid, M.; Kresse, G.; Buchsbaum, A.; Napetschnig, E.; Gritschneider, S.; Reichling, M.; Varga, P. *Phys Rev Lett* 2007, 99, 196104.
335. Schoiswohl, J.; Sock, M.; Chen, Q.; Thornton, G.; Kresse, G.; Ramsey, M. G.; Surnev, S.; Netzer, F. P. *Top Catalysis* 2007, 46, 137.
336. Krajčí, M.; Hafner, J. *Phys Rev B* 2005, 71, 184207.
337. Krajčí, M.; Hafner, J. *Phys Rev B* 2007, 75, 224205.
338. Nørskov, J. K.; Scheffler, M.; Toulhoat, H. *MRS Bull* 2006, 31, 669.
339. Gajdos, M.; Eichler, A.; Hafner, J. *J Phys Condens Matter* 2004, 16, 1141.

340. (a) Gajdos, M.; Hafner, J.; Eichler, A. *J Phys Condens Matter* 2006, 18, 13; (b) Gajdos, M.; Hafner, J.; Eichler, A. *J Phys Condens Matter* 2006, 18, p. 41.
341. Eichler, A.; Hafner, J.; Gross, A.; Scheffler, M. *Phys Rev B* 1999, 59, 13297.
342. Mittendorfer, F.; Hafner, J. *Surf Sci* 2001, 472, 133.
343. Mittendorfer, F.; Hafner, J. *J Catal* 2003, 214, 234.
344. Eichler, A.; Hafner, J. *Phys Rev B* 1999, 59, 5960.
345. Eichler, A.; Hafner, J. *J Catal* 2001, 204, 118.
346. Hirschl, R.; Eichler, A.; Hafner, J. *J Catal* 2004, 226, 273.
347. Raybaud, P.; Costa, D.; Corral-Valero, M.; Arrouvel, C.; Digne, M.; Sautet, P.; Toulhoat, H. *J Phys Condens Matter* 2008, 20, 064235.
348. Opalka, S. M.; Vanderspurt, T. H.; Radhakrishnan, She, Y.; Willigan, R. R. *J Phys Condens Matter* 2008, 20, 064237.
349. Hafner, J.; Benco, L.; Bucko, T. *Topics in Catalysis* 2006, 37, 41.
350. Brønsted, N. *Chem Rev* 1928, 5, 231.
351. Topsoe, H.; Clausen, B. S.; Massoth, F. E. *Hydrotreating Catalysis—Science and Technology*; Springer: Berlin, 1996.
352. Schweiger, H.; Raybaud, P.; Kresse, G.; Toulhoat, H. *J Catal* 2002, 207, 76.
353. Helveg, S.; Lauritsen, J. V.; Laegsgaard, E.; Stensgaard, I.; Clausen, B. S.; Topsøe, H.; Besenbacher, F. *Phys Rev Lett* 2000, 84, 951.
354. Raybaud, P.; Hafner, J.; Kresse, G.; Kasztelan, S.; Toulhoat, H. *J Catal* 2000, 190, 128.
355. Arrouvel, C.; Breysse, M.; Toulhoat, H.; Raybaud, P. *J Catal* 2005, 232, 161.
356. Costa, D.; Arrouvel, C.; Breysse, M.; Toulhoat, H.; Raybaud, P. *J Catal* 2007, 246, 325.
357. Demuth, T.; Hafner, J.; Benco, L.; Toulhoat, H. *J Phys Chem B* 2000, 104, 4593.
358. Benco, L.; Hafner, J.; Hutschka, F.; Toulhoat, H. *J Phys Chem B* 2003, 107, 9756.
359. Benco, L.; Bucko, T.; Hafner, J.; Toulhoat, H. *J Phys Chem B* 2004, 108, 13565.
360. Barbosa, L. M.; van Santen, R. A.; Hafner, J. *J Am Chem Soc* 2001, 123, 4530.
361. Benco, L.; Bucko, T.; Grybos, R.; Hafner, J.; Sobalik, Z.; Dedecek, J.; Hrusak, J. *J Phys Chem C* 2007, 111, 586.
362. Rozanska, X.; Demuth, T.; Hutschka, F.; Hafner, J.; van Santen, R. A. *J Phys Chem B* 2002, 106, 3248.
363. Rozanska, X.; van Santen, R. A.; Demuth, T.; Hutschka, F.; Hafner, J. *J Phys Chem B* 2003, 107, 1309.
364. Bucko, T.; Hafner, J.; Benco, L. *J Phys Chem B* 2004, 120, 10 263.
365. Demuth, T.; Rozanska, X.; Benco, L.; Hafner, J.; Toulhoat, H. *J Catal* 2003, 214, 68.
366. Rozanska, X.; van Santen, R. A.; Hutschka, F.; Hafner, J. *J Am Chem Soc* 2001, 123, 7655.
367. Rozanska, X.; van Santen, R. A.; Hutschka, F.; Hafner, J. *J Catal* 2002, 205, 388.
368. Vos, A. M.; Rozanska, X.; Schoonheydt, R. A.; van Santen, R. A.; Hutschka, F.; Hafner, J. *J Am Chem Soc* 2001, 123, 2799.
369. Rozanska, X.; van Santen, R. A.; Hutschka, F.; Hafner, J. *J Catal* 2003, 215, 20.
370. Bucko, T.; Benco, L.; Hafner, J. *J Phys Chem A* 2004, 108, 11388.
371. Bucko, T. *J Phys Condens Matter* 2008, 20, 064211.
372. Fleurat-Lessard, P.; Ziegler, T. *J Chem Phys* 2005, 123, 084101.
373. Laio, A.; Parrinello, M. *Proc Natl Acad Sci USA* 2002, 99, 12562.
374. Bucko, T.; Benco, L.; Hafner, J.; Ángyán, J. G. *J Catal* 2007, 250, 171.
375. East, A. L. L.; Bucko, T.; Hafner, J. *J Phys Chem A* 2007, 111, 5945.